Toward Improving General Quantum Imaging Algorithms and the Realization of Quantum Recording

by

Brayden Freitas

A thesis submitted to
the University of Ottawa
in partial fulfillment of the thesis requirement
for the degree of
Master of Science
in Physics

Examining Committee

The following served on the Examining Committee for this thesis.

Internal Members:	Hang Chi Assistant Professor, Dept. of Physics, University of Ottawa Khabat Heshami Adjunct Professor, Dept. of Physics, University of Ottawa
Supervisors:	Jeff Lundeen Associate Professor, Dept. of Physics, University of Ottawa Ben Sussman Adjunct Professor, Dept. of Physics, University of Ottawa

Declaration of Authorship

I hereby certify that this thesis is entirely my own original work except where otherwise indicated. I am aware of the University's regulations concerning plagiarism, including those concerning consequent disciplinary actions. Any use of the works of any other author, in any form, is properly acknowledged at their point of use.

Abstract

Various quantum imaging techniques have been shown to be effective at imaging through some aspects of traditionally difficult free-space channels, including ghost imaging through turbulent channels, or quantum illumination through channels with noisy backgrounds. For quantum illumination through channels with noisy background, a full rigorous theoretical framework has never been given. This thesis begins by providing such a theoretical framework for a version of quantum illumination which relies on spatial correlations. While these techniques have only ever been shown to work independently, real-world free-space channels are often both turbulent and noisy simultaneously. This thesis then goes on to describe and experimentally demonstrate a quantum correlated imaging method which uses an SPDC source and a time-tagging camera which be made robust against both turbulent media and a noisy background in free-space channels by implementing filtering based on the temporal and spatial correlations of paired photons. Furthermore, the filtering reduces accidental coincidence counts between uncorrelated photons, allowing the pair source to operate at high brightness which, in turn, leads to video-rate integration times. These quantum correlated recordings allow for improved object tracking, while the longer integration time images improve image fidelity over turbulent and noisy channels. This demonstration could allow for new improvements in communication, measurement, and sensing through turbulent and noisy free-space channels.

Acknowledgements

I would like to thank my friends, co-workers, and family for supporting me mentally, physically, and emotionally through my degree, both in-person, and from halfway across the world. I specifically would like to thank my friend Matt Aziz for many much-needed breaks in the forms of rock climbing, hiking, camping, and simply hanging out together. I would also like to thank my partner Leah Oster for consistently supporting me and considering me throughout the arduous thesis writing process, and providing me with (unintentionally) caffeinated birthday cake which fueled a large part of the theory work here. Further, I would like to thank my friend Shantanu Vyas for allowing me to use his laptop while on vacation to polish off and finally submit this thesis. I would also like to thank my friends who I talk to on Discord for the many days and nights of company after moving to a new country.

From within the lab, I would like to thank many students and post-docs in the UOttawa physics department, as well as the NRC SDT department. Duncan England, Andrew Proppe, Manuel Ferrer, Yingwen Zheng, Kyle Jorden, Nick Sorensen, Kate Fenwick, Guillaume Thekkadath, Alicia Sit, Ramy Tannous, and Nick Couture, just to name a few, provided me with many scientific and educational conversations, along with social support.

I would like to acknowledge my advisors Jeff Lundeen and Ben Sussman for their support throughout my degree and consideration of my constantly changing situation regarding being in Canada. I am also very grateful to Lora Ramunno, who supported me in my teaching endeavors, along with providing much appreciated advice and support. I would like to thank my committee members Hang Chi and Khabat Heshami for agreeing to be on my committee with such short notice, and for thus supporting my academic choices. More generally, I would also like to thank my community at large, specifically that of the Baltimore area community, without the support of which I would never have even dreamed of attaining higher education in a foreign country, let alone undergraduate education. Among many educators, I would like to acknowledge Linda McDonough, who gave me access to invaluable resources during my time in high school which put me on the path to college and beyond. I also would like to mention Grace Cooper, Stu Chapman, and Douglas Cerasoli, all of whom unfortunately passed away before I ever had the opportunity to properly thank them for their support of a child who was overly excited by the weather and random encyclopedia facts. Community support, at all levels, is truly the only means of improving the life, available opportunities, and level of personal freedom of people in under-served communities.

Table of Contents

List of Tables

List of Figures

Chapter 1

Introduction

1.1 Free-Space Optical Sensing and Communication

To inspire the work performed in this thesis, the problems which the work solves must first be identified. Free-space optical sensing and communication are the primary fields which contain problems that can be solved by quantum imaging techniques, and as such a brief overview of some applications of the fields are given here. In describing the applications, their shortcomings and difficulties they face will become clear. Once these shortcomings are described appropriately, the relation to this thesis' work can be elucidated.

1.1.1 Free-Space Optical Sensing

Object Recognition and Tracking

Two of the most widespread uses of free-space optics are for object recognition and object tracking. In object recognition, the spatial and spectral properties of a general scene are measured by a sensor through some optical system. These properties, either individually or in conjunction with one another, are cross-referenced with known properties of an object of interest, and the degree of similarity between the known and observed properties is given. This leads to some metric which indicates how likely it is that a specific known object is in the scene, or how similar a subset of the scene is to a known object. Object recognition is used widely, in applications ranging from the very common uses in security measures for systems like personal cellphones and PCs, to more specialized uses like disease identification in medical image analysis [59].

In object tracking multiple frames are considered, over which the location of an object within those frames is measured and kept track of. Similar to in object recognition, known properties of a specific object of interest are compared with measured properties in each frame, and possibly across multiple frames. This generates a metric which gives the location of the object, or some other position/movement related metric of the object, either within the frame or relative to some fixed reference point, along with some certainty. In basic object tracking, like for example in rudimentary aircraft tracking or car speed estimating, both via RADAR, the constraint of the known properties matching with the expected properties is weak, and is often simply implied by the context of the measurement. For more advanced object tracking, like for the tracking of a specific individual in a crowd, the matching of the observed and known properties must be very strict, and full object recognition must be performed at minimum on every frame for successful tracking [39].

LiDAR

An increasingly common free-space optical sensing tool, dubbed LiDAR, allows for the determination of distances of a target object or surface from the measurement tool. LiDAR works by shining a laser beam at a target of interest, and measuring the time it takes for the laser beam to reflect off the target and return to its source. Taking this time of travel into account allows for the distance between the target and camera to be estimated. Such a tool is used frequently to make high-resolution surface maps of the Earth, as well as to assist in the navigation of self-driving vehicles, but also is used in less common applications like mapping buried sites for assisting in anthropological investigations [25].

1.1.2 Free-Space Optical Communication

Classical Free-Space Optical Communication

Historically, free-space optical communication has existed in some form well before most other forms of long-distance communication. These forms include the pre-industrial use of smoke signals by Indigenous Americans or the use of beacons by the Ming dynasty [52, 63], industrial-era contemporary uses of lighthouses and semaphores [21], and the post-industrial-era uses of heliographs by the North American forestry protection [16]. Modernly, attempts have been made to develop free-space optical communication networks with varying degrees of success, though most attempts have been generally unsuccessful. Extraterrestrially, there have been significant pushes towards practical free-space optical

communication networks, with the European Space Agency having demonstrated non-commercial applications of such a network [1]. Generally, applications for classical free-space optical communication are limited, primarily due to the shortcomings of range and turbulence effects outweighing any other potential benefits over more common fiber and/or wire based communication.

Quantum Key Distribution

One of the more promising applications of free-space optical communication is regarding quantum key distribution. Quantum key distribution allows for the sharing of a secret key between two parties, such that it would be known with certainty whether a third party intercepted the secret key, thus rendering the key no longer secret. This secret key can be used in order to cryptographically encode and decode a confidential message, or to verify the identity of the sending party. While not all quantum key distribution schemes rely upon free-space optical communication, it is one of the successful methods by which quantum key distribution has been demonstrated so far [18, 43, 45]. Generally, free-space optical quantum key distribution works by the sender encoding information into the quantum states of single photons, and the receiver making measurements on the single photons which arrive at them [10]. Such schemes have been shown to work in not only atmospheric conditions on intracity scales [64], but also underwater at shorter scales [13].

1.1.3 Shortcomings

In all the described schemes above, there exist shortcomings which effect each scheme to differing degrees. These shortcomings can be categorized into two separate categories based on the origin of the shortcomings: distortions due to turbulent media, and noise due to external sources.

Turbulent Media

The distortions in the spatial information of a free-space optical signal which arise from the propagation of the signal through turbulent media lead to a wide range of difficulties in most practical free-space optical processes. These distortions typically cannot be simply corrected for, and as a consequence many free-space optical processes are currently impractical for use in some, or most, contexts. A common result of this, for example, is how

most modern terrestrial astronomical observatories are located at high elevations, where signals from space do not have to propagate through as much of the atmosphere.

Turbulent media is any media, be it a solid, liquid, gas, or combination of any of these three, which causes light to be reflected, diffracted, or scattered in any way, such that all the light which enters the media also exits the media without creating any new light. This is in contrast to turbulence, which includes turbulent media, but can also absorb light, emit light, or combine these two processes to absorb incoming light and then emit new light. While the effects of turbulence (as opposed to *turbulent media*) also have deleterious affects on most practical free-space optical processes, turbulence is a broader problem which the work performed here is unable to address fully. After propagating through turbulent media, the spatial profile of the signal is distorted in some potentially chaotic way, which cannot be easily measured or predicted without prior knowledge of the entire system [61]. As such, any free-space optical process which relies upon the initial spatial profile of the signal will not be able to function as expected without compensating for the distortion effects.

For object recognition, the distortion from propagating through turbulent media can lead to the observed properties of the target differing from the prior known properties, even though the object is in fact the same as the one known beforehand. This is because the environment through which the properties are observed is different from what it was when the known properties of the object were initially measured. This can lead to not only a drop in the confidence of the identification of the object, but also can lead to a misidentification of the object if the spatial profile is distorted in such a way that the properties now seem more similar to the properties of some other known object. In the worst case, the target may not even be recognizable in the system, and thus nothing would be recognized even though an object is present. Typically, distortions are not a significant problem in common object recognition scenarios since the distance of the object from the camera is often very short, however for more complex and distant scenes it poses a distinct open problem with no solid solution [38].

While inheriting the same problems as with object recognition, object tracking has further issues as well: even if the object is able to be identified through the turbulent media, for example in the cases where object recognition comes from context, the actual position-related information of the object may be inaccurate due to the position information being distorted in some stochastic way by the propagation [27]. While object tracking is often used at long distances through turbulent media, either the location of the object is contextual and so the only issue is that of the imprecision of the measurement, as is in the case of car speed estimating, or wavelengths of light are used which are less effected by atmospheric turbulence, as in the case of RADAR [36].

LiDAR is significantly affected by the distortions from propagating through turbulent media, both as an effect of a portion of the out-going laser light not making it back to the measurement device, but also from the optical path length being increased by the refraction of the signal. In fact, LiDAR is so uniquely sensitive to atmospheric turbulence at short ($10 - 100\,\mathrm{m}$) and medium ranges ($15 - 30\,\mathrm{km}$), that it has been proposed to be used in aviation to measure atmospheric turbulence [48, 72]. Typical LiDAR measurements can be chosen to be done reliably on clear days with good conditions, since they are often not time-critical.

Classical free-space optical communication is significantly impacted by the distortions from propagating through turbulent media. While many older implementations are not significantly impacted due to the small amount of data which they transmit, the more data-dense methods like semaphores and heliographs have been mostly replaced by more modern non-free space solutions, partly because of the difficulty and drawbacks related to propagating through turbulent media. Adaptive optics are often utilized in order to mitigate the distortion effects, but are so far only successful in preserving telecom bitrates on the scale of hundreds of meters. The significant impact from distortions is the leading cause of limitations, and consequent failure, of modern terrestrial free-space optical communication attempts, though proposals for schemes using light in the infrared and near-radio ranges seem more promising [54].

While quantum key distribution via free-space optical channels suffers from many of the same issues as in classical free-space optical communication, it does have some benefits which increase its practical range. Notably, quantum key distribution does not require nearly as high of bitrates as modern telecom demands, since it is only being used to communicate a secret key. As such, the range of use for quantum key distribution is longer, though still limited to be around $10\,\mathrm{km}$ [64]. One benefit quantum key distribution uniquely can have is an increase in the information density per photon over classical communication by encoding information in bases like orbital angular momentum [14], or more complex encoding schemes utilizing topological properties [42]. By having more information density per photon, the bitrate of quantum key distribution can be increased without increasing the photon-detection rate at the receiver, though the effects of the distortion from turbulent media on these new encoding degrees of freedom must be considered.

Noise

Noise from external sources is another significant problem for many of these schemes, though it is more straightforward. Noise from external sources can come in many different forms, whether it be from the sun, from light pollution, from other artificial light sources,

from stars, from the moon, or any number of other points of origin. One unifying factor with all the sources is that the light contains some other information which is not the information the signal light contains.

In both object recognition and object tracking, external noise can lower the relative intensity of the light coming from the object of interest, leading to less detail in the observed properties of the object. This in turn creates more uncertainty in the measurement metrics as they relate to the object. Furthermore, if there is any structure to the external noise, it is possible for an object recognition or tracking scheme to misidentify the noise as an object of interest, and as a result misidentify a scene [75]. In object tracking, however, since external noise (often referred collectively to as the "background") is typically static while objects (also referred to collectively as the "foreground") are typically moving, there exists foreground detection schemes, and subsequent background subtraction schemes, to help mitigate the effect of external noise [49].

For LiDAR, external noise has been a consideration since its inception, however LiDAR has the benefit of only expecting to detect light at the same wavelength as its laser source. As such, a narrow band-pass filter can significantly reduce the effects of external noise, though this is not practical in all cases [73]. Even with a narrow band-pass filter, it is common practice to take LiDAR measurements at night and with a narrow field of view, in order to further minimize the effects of external noise [29]. Methods of background noise reduction for traditional LiDAR have been proposed [17], and as will be discusses in the following section, modifications taking advantage of quantum properties have also been proposed to increase resilience to noise [46].

Free-space optical communication, both classically and in quantum key distribution, is limited drastically by external noise sources, specifically in the form of the sun. For quantum key distribution especially, since the signal is attenuated to the single photon level, the effects from external noise sources are very strong. The strength of external noise is such that protocols are often only able to be executed at night, during a new moon, and preferably with a receiver facing away from any significant sources of light pollution [64].

1.1.4 Conclusion

In the modern world there are many diverse free-space optical sensing and communication protocols and designs. While some of them are used extensively in normal everyday life and to support infrastructure, research, and technological development, there are still significant limitations which have continued to stifle the further development of some of

these technologies for decades. The two main shortcomings are a lack of robustness against the effects of distortions arising from propagating through turbulent media, as well as a lack of resilience against external sources of noise.

As alluded to in the discussion of how LiDAR is affected by external noise, imaging solutions reliant upon quantum properties have been proposed which can increase resilience against external sources of noise, dubbed quantum illumination. Further, other imaging solutions reliant upon quantum properties have been proposed which can improve robustness of imaging techniques against the distortions which arise from a signal propagating through turbulent media, dubbed ghost imaging. The purpose of this thesis will be to investigate these techniques in detail, in order to understand how they would need to be modified to be used in conjunction with each other, and in turn develop a new quantum imaging technique which improves upon previous techniques.

1.2 Quantum Imaging

Typical quantum imaging schemes rely upon pairs of entangled photons, and take advantage of the inherent correlations between the photons in order to produce images with better properties than what are possible from equivalent classical imaging schemes. As such, quantum imaging schemes have three primary components: a source of entangled photons, the method of optical interaction with the target or scene of interest, and a detection mechanism. In the quantum imaging schemes discussed here, the source of entangled photons is spontaneous parametric down conversion (SPDC). As for the method of optical interaction with the target, for simplicity it will be assumed to be equivalent to binary transmission or reflection. That is, either the light completely transmits/reflects off the object and reaches the detection mechanism, or it is absorbed/reflected away such that it does not reach the detection mechanism. The two schemes — ghost imaging and quantum illumination — differ in their detection mechanisms, however in both the time of arrival information of the photons must be measured at minimum.

1.2.1 Spontaneous Parametric Down Conversion

Overview

Spontaneous parametric down conversion is a process by which one pump photon is converted into a pair of photons within a medium. The photon pair is made up of two entangled

photons — the "signal" and "idler" — which have correlations in position and energy [32]. These correlations are key to allowing many quantum imaging schemes to function, and as such must be understood to a basic level in order to connect it with quantum imaging.

Basic Theory

The aforementioned energy correlation between the signal and idler is a consequence of the energy conservation in the SPDC generation process (Figure 1.1.C). The correlation is such that the energy of the signal and idler photons must sum up to equal the energy of the pump photon which they were produced by, and thus knowing the energy of the pump photon and one of the generated pair photons absolutely determines the energy of the other generated photon. A degenerate SPDC source is a source where the energies of the signal and idler photons are identical. The degeneracy of an SPDC source is not necessary for quantum imaging, and in fact there exists quantum imaging schemes which rely upon non-degenerate SPDC sources [6, 41, 77]. That is, SPDC sources where the energies of the signal and idler photons are not identical can be utilized in quantum imaging. It is beneficial experimentally to work with a degenerate SDPC source, however, as when both photons in the pair are at the same wavelength, they will interact with optics in the same way as one-another. This includes interactions with lenses, mirrors, and filters, and further assures the photons are both measurable by detectors and cameras at the same efficiency. In the case of this work, a degenerate SPDC source is utilized, rendering the photons indistinguishable in the energy degree of freedom.

The position correlations are a consequence of a combination of the momentum conservation and local of generation of photons within the generation medium (Figure 1.1.(A,B)). The first part of the position correlations is that the signal and idler photons are generated simultaneously at the same location within the crystal. The second part is that the momenta of the two photons is such that the vector sum of the two will result in the original momentum of the pump photon which was destroyed to create them. These correlations have two useful consequences in the context of this work. The first benefit is that when the two photons travel the same optical path length, they will do so in the same amount of time. This means that if the photons are manipulated in such a way that they travel different paths to a sensor while still covering the same optical path length, then photons which were generated in pairs will arrive at the same time. While not all simultaneously arriving photons at the camera will be from pairs, this will show a statistical significance in the time of arrival (ToA) statistics of the all arriving photon pairs at a difference in ToA (dToA) ≈ 0 seconds. The second benefit, is that if the momentum of one photon from the pair is known, and the momentum of the pump beam is assumed to be orthogonal to the

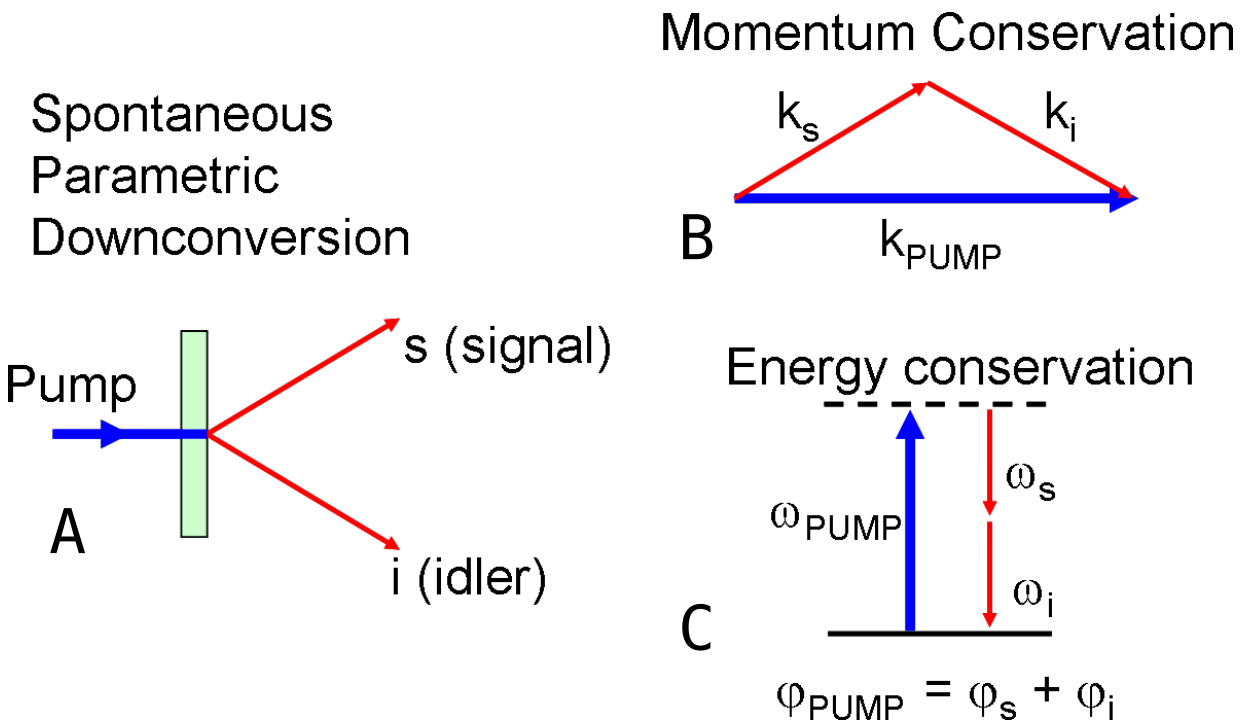

Figure 1.1: **SDPC Correlations.** (A) Production of signal and idler photon pairs from one pump photon within a medium via SPDC. The depicted correlations here assume perfect phase matching of the pump with the medium. (B) The vector sum of the momenta of the signal and idler photons must add up to be (approximately) equal to the momentum of the pump photon which they were created from. (C) Likewise, the sum of the energies of the signal and idler photons must add up to be equal to the energy of the pump photon. For degenerate SPDC, the energies of the signal and idler photons are equal to each other. Adapted from content created by J S Lundeen via Wikipedia.

camera plane, then the momentum of the other photon from the pair can be inferred.

A more careful and detailed discussion of the basic theory overviewed here, including mathematical descriptions and derivations of the correlations and photon statics of SPDC biphotons, can be found in Appendix A.1.

1.2.2 Quantum Illumination

Overview

Quantum illumination (QI) utilizes a quantum entangled light source, like SPDC, to better illuminate a target through a noisy channel [46]. This is accomplished by illuminating a target with the signal photons from the entangled source, and then spatially and temporarily measuring all light which illuminated the target, including light from other sources (Figure 1.2.A). In the most basic version of QI, a time-correlation measurement of this measured light is performed with the light from the idler photons from the quantum source. Light which illuminated the target from the quantum source can be distinguished from background light by rejecting identified pairs which are not correlated in time, thus creating an imaging technique which is robust against noise [65].

While the above imaging scheme has been shown to work to some capacity, the presence of external sources stronger than the signal results in many accidental pairings, and as such more complex QI schemes have been developed. These schemes rely upon more than just the temporal correlation of light from SPDC sources. Specifically, the spatial correlations have also been utilized [35, 47]. If the momenta of the pump photons which create the signal and idler pairs is such that it is orthogonal to the measurement plane, then the signal and idler photons will be spatially measured in positions reflected over the center of the transverse beam profile. As such, any measured pairs which are not observed to have the photons rotated 180° around the center of the beam profile are also filtered out of the results. This modification allowed for a stark decrease in the number of accidental pairs in QI, and thus an increase in image contrast.

Applications

Quantum illumination has found multiple applications over the last few years [31]. Two applications of interest are in the improvement of classical RADAR detection of objects in noisy environments, and quantum LiDAR. The improvement of classical RADAR detection of objects in noisy environments is a direct consequence of the mechanism of QI as described

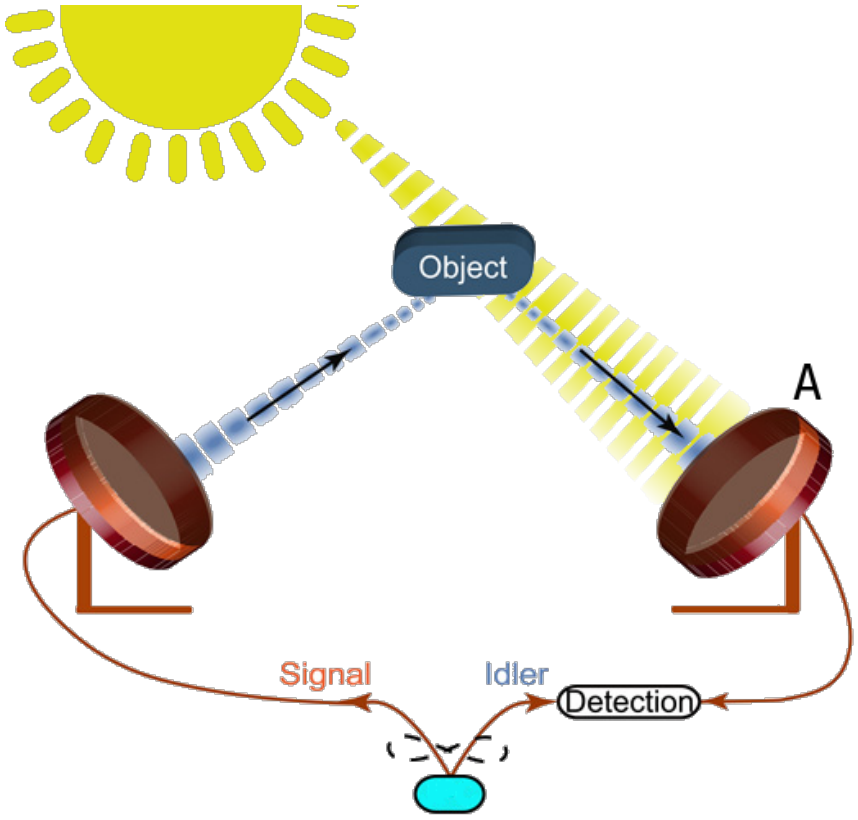

Figure 1.2: **Quantum Illumination.** A visual depiction of how quantum illumination functions. The entangled photons from the source (light blue) are split into two different paths. The idler photon goes directly to a time detector, while the signal photon is sent toward an object. This signal photon interacts with the object in some non-absorptive way (here a reflection), and is then measured both temporally and spatially (A). Other sources of light, here depicted by the sun, are also measured by the same sensor as the signal photons (A). The correlations between photons measured at position A, and the idler photons are calculated, and only pairs with strong correlations are kept. As such, most of the photons from external sources are filtered out. Figure adapted from [9].

above [9]. One implementation difficulty is that quantum sources tend to be too low-flux to effectively measure objects remotely in real time. As such, improvements which utilize Guassian or multi-photon entangled states have been proposed which could help to improve the flux of the quantum source [68].

Quantum LiDAR is a modification to traditional LiDAR techniques which utilizes a quantum source. This allows for shortening the time needed to measure difficult-to-image scenes [50], and also to minimize the background noise or interference in measurements taken in difficult-to-image-within environments [67]. Quantum LiDAR has also been shown to increase the resolution and range of classical LiDAR [44]. All of these improvements are direct consequences of the mechanism of QI as described above.

Shortcomings

While QI's robustness against noise can be significant, it also comes with many shortcomings. As previously mentioned, applications for QI are limited by the low flux of the quantum sources. While solutions to this issue have been proposed, they rely upon technologies which are either unrealized at the current time, or are too immature for application. The other major shortcoming of QI, is its lack of robustness against turbulence. Since the signal photon interacts with a scene or target, imaging of the scene using the signal photon suffers to the same degree as direct imaging does from the effects of turbulence. Further, the reliance of QI on the correlations between the photons can actually cause QI to be more sensitive to turbulence than classical imaging. This is because turbulence affects the spatial (and to a lesser extent the temporal) correlations of the signal photon with the idler photon.

1.2.3 Ghost Imaging

Overview

Similar to QI, by taking advantage of the correlations of photon pairs generated by SPDC, ghost imaging (GI) is an imaging technique which allows for an object to be imaged with a single pixel detector [58]. In a GI setup, a target is illuminated by the signal photons which are then detected with a bucket detector that has only temporal resolution, and thus no spatial resolution. Concurrently, the idler photons, which have not interacted with the target, are captured by a detector with both temporal and spatial resolution. By virtue of the inherent temporal and spatial correlation between the photon pairs, an image of the

target can be formed through the idler photons even though they never interacted with the target. It is worth noting that while SPDC is a common source of correlated photons for use in GI, and actually was the original source and inspiration of the technique [6,7,33,56], GI can alternatively utilize classical sources [11,28,55].

In GI, the momenta of the signal and idler photons are generally correlated as described in the SDPC overview, and the momenta of the pump photons which created the pairs is assumed to be orthogonal to the plane of the target and sensors. As such, the position of arrival of the idler photons at the camera plane will be reflected over the center of the transverse beam profile as compared to the position of arrival of the signal photons at the bucket detector plane. Identifying pairs of photons generated simultaneously by the correlated source via calculating the dToA between all possible pairs of photons detected from each sensor (Figure 1.3.A) allows for the pairs which exists with a dToA ≈ 0 to be kept in the data set. These pairs are assumed to originate from the correlated source. Since only signal photons which were not blocked by the target reach the bucket detector, these are the only photons which are considered in the pairing, and thus dToA calculation. As a result, when the pairs with large dToA are removed from the idler image (Figure 1.3.B, gray) only pairs in the shape of the spatial profile of the signal beam are left in the image (Figure 1.3.B, red), though reflected over the center of the beam.

Applications

While GI has existed for decades, only a handful of applications of the process have come to fruition. While a few one-off applications do not fit the mold [31,51], applications generally fall into one of two categories: two-color ghost imaging, and low-light imaging. In two-color ghost imaging, the signal and idler photons are at very different energies, typically with the idler in the infrared or near-infrared [6]. Since many camera sensors are most sensitive in the near-infrared region of the electromagnetic spectrum, it would be beneficial to perform all camera measurements at this energy. Unfortunately, not all targets which are to be imaged are opaque at this energy. Thus, by interacting with the object with the signal photon at some other energy, the camera measurement is performed with high sensitivity, while the object is interacted with in the electromagnetic spectrum region of interest.

For low-light imaging, classical imaging is generally limited by noise which originates from background light sources or even simply dark counts of a sensor. With GI, the majority of noise events from background light sources and dark counts of the sensor can be filtered out since the preserved photons in the ghost image must be correlated with a photon from the signal arm [56]. The signal arm photons are measured by bucket detectors which can have much lower dark counts than even the best cameras at the same, or better

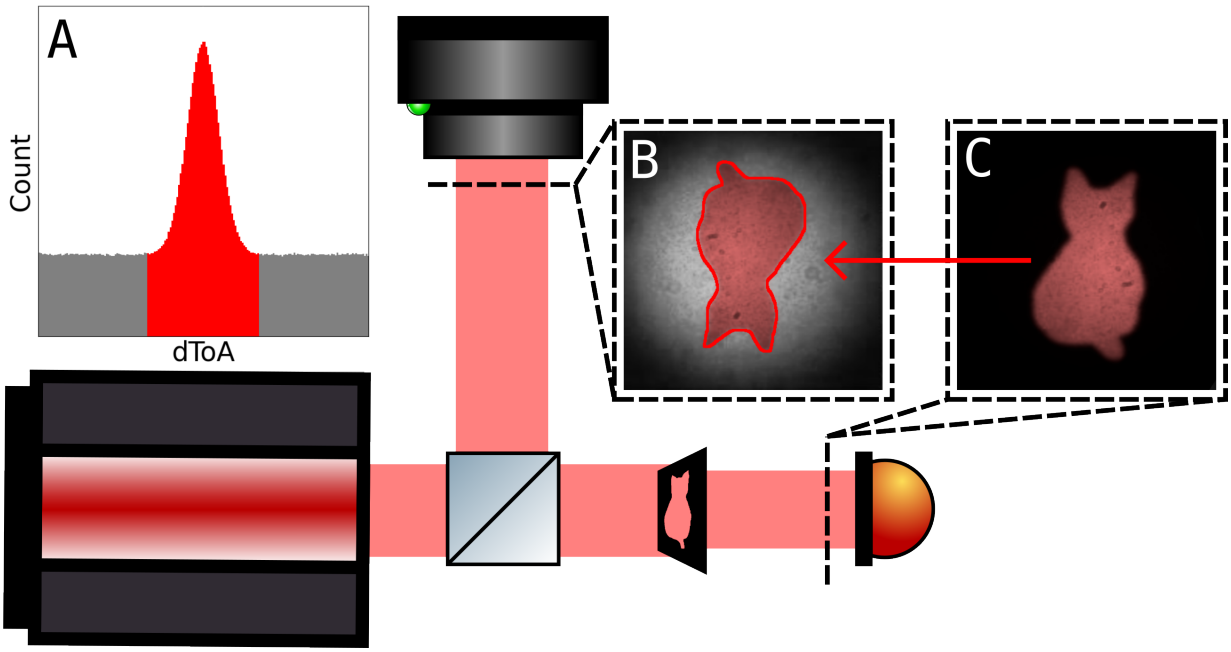

Figure 1.3: **Ghost Imaging.** A visual depiction of ghost imaging. Signal and idler photons generated by a correlated source are split into two identical length paths. The idler beam (upper path) is spatially and temporally resolved after the paths split. The signal beam is partially blocked by a target (here a cat) after the paths are split, and then is only temporally resolved. The time of arrival difference (dToA) between the signal and idler beam photons is calculated from the measurements (A). The pairs with dToA near 0 are kept (in red), while the rest of the pairs are not considered. Since signal photons are blocked by the target, they never reach the bucket detector (C). Note that the bucket detector does not measure the spatial information which is depicted in C, however this information is shown here to help explain the concept. While the idler image (B) is simply a spatial profile of the idler beam (which did not interact with the target, and thus is just a spatial profile of the source beam), all photons in pairs with dToA near 0 (red) are in the shape of the target (though mirrored). The red region of B is referred to as the ghost image.

sensitivity, and thus the dark counts in the idler image are nearly all filtered out. Further, the background light sources will statistically be unlikely to have a dToA of ≈ 0 between the two sources, and so will also be preferentially filtered out.

Shortcomings

While GI does work to some extent, a large reason for its lack of seriously pursued applications is because of its many shortcomings. First, and most historically significant, is that GI is a slow process compared to similar imaging processes. Original GI techniques utilized scanning single photon detectors which needed to physically move over the entire imaging space in order to resolve the idler photons in both space and time [24]. This was very slow as it relied upon the physical movement of a detector, with individual images taking hours to resolve. Later GI implementations utilized gated CCD cameras, where the signal photon was used as a trigger to begin a very short exposure time on a traditional CCD camera [7]. This cut the exposure times down, however by using a traditional CCD, the rate of idler photon detection was low, and dark counts were high. This resulted in exposure times on the scale of around an hour.

The use of intensified-CCD cameras incrementally shortened this time further, though the next significant improvement came with the development of single photon avalanche detector (SPAD) arrays [33]. SPAD arrays allow GI exposure times to go below 1 minute, with recent experiments even pushing the limit down to ~ 1 second [80]. While SPAD arrays were initially limited by resolution, they now have high enough resolutions for meaningful application. The main limiting factors for GI with SPAD arrays is that of background noise from accidentals. Longer exposure time allows for tighter temporal filtering, and thus a reduction in accidentals. As such, accidental photon pairing currently limits GI from approaching real-time imaging and recording, significantly narrowing its application scope.

1.2.4 Quantum Correlated Imaging

Overview

GI and QI are unique imaging techniques, but in the quickly developing field of quantum imaging, they are also quite dated. Recent developments in sensor technology have allowed for efficiently measuring different degrees of freedom of photons alongside their time of arrival and position. As such, a new class of quantum imaging techniques, dubbed quantum

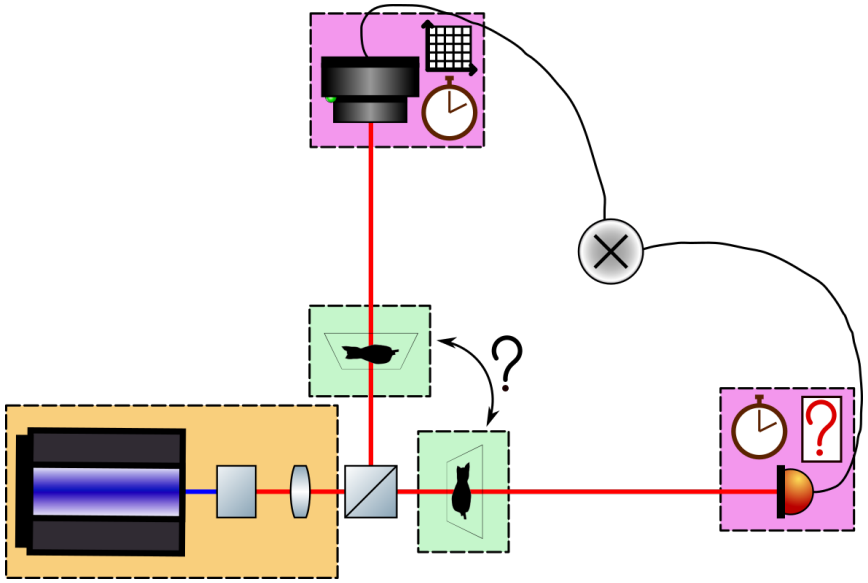

Figure 1.4: **General Quantum Correlated Imaging System.** Depicted here is a schematic for a general quantum correlated imaging system. The orange region indicates a source of photon pairs (here a crystal pumped with a strong laser to produce SPDC), while the green region indicates the target, and the purple region indicates the measurement apparatus. The target can be placed in either the idler beam path (top) or the signal beam path (right). At the end of the idler path both position and ToA information of the photon is measured, whereas at the end of the signal path ToA and some other degree of freedom are both measured. Here two different measurement devices are shown, however in practice different regions of the same device could be used instead.

correlated imaging, have emerged. In quantum correlated imaging, photon pairs which are correlated in multiple degrees of freedom are considered. This concept expands on the idea of a heralded measurement, where instead of the heralding idler photon only providing time of arrival and position information, it also provides other information related to another degree of freedom in which it is correlated with the signal photon.

A schematic of a general quantum correlated imaging system is given in Figure 1.4. Photon pairs are generated from the source with temporal correlations, spatial correlations, and potentially other correlations. These photons are split at a beam splitter into a top path containing the idler photons, and a right path containing the signal photons. The target of interest can be within either the signal or idler path, depending on the design of the system. The idler photons are then resolved in both time and space, while the

signal photons are resolved in both time and some other degree of freedom in which it is correlated with the idler.

Quantum correlated imaging systems are very general, and in fact both QI and GI are technically instances of the general class of quantum correlated imaging. This is evident if you consider that in QI the target is in the idler arm, while in the signal arm the other degree of freedom measured is nothing. Likewise for GI, the target is in the signal arm with nothing as the other degree of freedom, and the space and time information in the idler arm is used to resolve it.

Applications

While the concept of quantum correlated imaging is fairly new, applications are already emerging. The application of quantum correlated imaging is typically dependent on the extra degree of freedom being measured. When spectral information is considered, hyperspectral imaging is possible where the broadband spectral information of a target or scene is determined for every spatially resolved portion of the final image [77]. When the momentum is considered, both position and momentum information about light which interacts with a scene can be known [79]. This allows for utilizing raytracing to produce 3D or volumetric images of a scene [76, 79], and also via phase retrieval allows for phase microscopy [37, 78].

Shortcomings

Depending on the placement of the target, the other degree of freedom to be measured, and the measurement apparatus, the shortcomings of quantum correlated imaging can be numerous. Most notably however, is that quantum correlated imaging is a slow process. Typical state-of-the-art exposure times are on the order of 3-8 minutes [76, 78]. This can be due to a multitude of factors often relating to the mechanism of measurement for the other degree of freedom, however an overarching issue is that of external noise. In order to get reliable measurements, the signal-to-noise ratio of the measurement must be low, however when looking at a very wide degree of freedom like spectrum the possibility for external sources is very high.

1.3 Using Quantum Imaging to Improve Free-Space Optical Sensing and Communication

As outlined in the introductions of GI and QI, these quantum imaging techniques have already begun to be used in ways to improve free-space optical sensing. Further, there exists aspects of these techniques which are currently unrealized in any practical way to improve free-space optical sensing and communication. Even further still, these techniques can be used in conjunction with each other to improve free-space optical sensing and communication in novel ways. This combination of QI and GI has never before been theorized nor demonstrated. The description and experimental demonstration of the benefit of combining these techniques is the main focus of this thesis. First, the individual benefits of these techniques will be introduced in more detail in this section, followed by a discussion of how these benefits can be combined to open the door to a new realm of improvements for free-space optical sensing and communication.

1.3.1 Ghost Imaging — Imaging Through Turbulent Media

GI has been shown to be inherently resistant to scattering caused by turbulent media [24, 53]. While there is some evidence to a wider scope of robustness against scattering caused by turbulent media at any point in the GI setup [19], the robustness of interest here is specifically against scattering of the spatial profile of the signal beam due to turbulent media located after the target of interest. In short, the robustness against this scattering is a result of the spatial information of the ghost image arising from the interplay between the initial spatial correlation of the idler photon with the signal photon, and the temporal filter of the possibly detected pairs.

In the aforementioned discussion of the mechanism of function of GI, there are two possible conclusions for the signal photon: either the signal photon is not blocked by the target, and is thus measured at the bucket detector, or it is blocked by the target, and thus not measured at the bucket detector. When turbulent media is present after the target, these conclusions are no different. In the scenario where the photon is blocked by the target, the photon will not be detected by the bucket detector, whether the turbulent media is present or not, and thus the conclusion is unchanged. In the scenario where the photon is not blocked by the target, it is then scattered in some way by the turbulent media. If this scattering is such that the photon still reaches the bucket detector, then again this conclusion is also unchanged. If the photon is scattered in some way by the turbulent media that it does not reach the bucket detector, then there is a slight decrease

in the visibility of the final ghost image. In either case, the presence of the turbulent media after the target does not affect the spatial profile of the ghost image in any way.

While patents for this scheme exist (and are comparable in length to this thesis), no publically available technologies have come to fruition which utilize this effect. This is likely due to the exposure time shortcomings of GI discussed previously.

1.3.2 Quantum Illumination — Quantum LiDAR and Heralded Communication

QI's application in free-space optical sensing has already been introduced in the previous section when discussing quantum LiDAR. To generalize this application, the primary benefit of QI is that it allows for decreasing the noise of any general measurement in which the final measured signal of interest is one which is also intentionally generated. This generalization brings to light that QI is a subset of a class of measurements which can be categorized as heralded quantum measurements. This class of measurements is very wide-reaching, and has applications across quantum science. Of interest here is that of heralded communication in QKD.

On-demand sources of true single photons are still an area of active fundamental research [5], and as such QKD protocols which require single photons have utilized heralded sources [69]. Further, for scenarios where classical noise is detectable at the measurement side of the quantum channel, heralding of the quantum signal can be beneficial to distinguish between desired and undesired measurements. The improvements made to QI, like utilizing the spatial correlations of the photons in the pair to better filter out unwanted noise, can potentially be extended to this QKD scenario.

1.3.3 Quantum Correlated Imaging — Hyperspectral and Extreme Depth of Field Imaging

While applications of quantum correlated imaging are currently being proposed, these applications are for imaging systems which already exist to some capacity classically. Individually, the designed systems may have differing benefits over their classical counterparts which arise from the quantumness of their source. One benefit common to all of these systems is that of single-shot acquisition of images without any moving parts. Typically, in order to spatially resolve multiple properties of a scene, a detector must somehow perform

a raster of measurements. This is often accomplished by either physically moving a detector to many different locations, or refocusing light from different locations on to a static detector. It is possible to consider an array of detectors for many of these measurements, however each individual detector needs some amount of space to perform the measure, which typically will scale with the accuracy of the measurement. Further, specialized measurement apparatuses are both expensive and fragile, and thus it is often prohibitive to have many of them. With quantum correlated imaging, only two specialized measurement apparatuses are needed: the time-tagging camera, and the measurement mechanism for the other degree of freedom. In practice, this is often only one device as the time-tagging camera can measure both things in different regions. This also allows the measurement apparatus for the other degree of freedom to be much larger than it would be if it were to be in an array of detectors of similar size to a time-tagging camera.

In hyperspectral imaging, it is common for either an image to be taken multiple times using tunable filters [30], or for a typical spectrometer to take a raster image over many different positions [34]. In both cases, the image acquisition time is long, and requires either the physical moving of a spectrometer, or the physical reconfiguration of a filter. With quantum correlated hyperspectral imaging, no reconfiguration nor physical movement is required, and in practice the measurement of the scene could be made as straightforward as any typical single mode spectral measurement.

In the phase imaging schemes, it is common for a sensor which measures both momentum and position of light to be used, like a Shack-Hartmann wavefront sensor [12]. With a Shack-Hartmann sensor, an array of lenslets is overlaid on a camera. When light arrives at a lenslet, the location of the center of the lenslet is considered the light's position, while the area below the lenslet where the light focuses to is considered the light's propagation direction. As a result, the position precision is inversely proportional to the size of the lens, while the direction precision is directly proportional to numerical aperture of the lens, and thus the size of the lens. This means that the two degrees of freedom are limited by each other. In quantum correlated phase imaging, the two degrees of freedom can be measured by detectors which are independent of one another, and thus are not limited by each other. Further, the measurement of the position information can be direct, thus only limited by the detector resolution, while the propagation direction information can be measured by propagating into the far field using a single lens, which is not in principal limited in size by the position measurement, and thus can have a large numerical aperture.

1.3.4 Combining Ghost Imaging and Quantum Illumination

Time-Spatially-Filtered Quantum Correlated Imaging

GI and QI are implemented in very similar ways (Figure 1.5.(A,B)), yet have different strengths in improving free-space optical sensing and communication. To gain both the robustness against scattering from turbulent media from GI, and the robustness against external noise from QI, a hybrid setup is proposed (Figure 1.5.C). This hybrid setup goes along with a new technique which is dubbed time-spatially-filtered quantum correlated imaging (TSFQCI).

TSFQCI allows for near-video-rate imaging of a target through a channel which contains both dynamic distortion effects from an active turbulent media and a large background noise from an external source. This is achieved through utilizing a single photon sensitive time-tagging camera [33,57] to measure the temporal and spatial correlations between photons in entangled photon pairs. Traditional temporal filtering from GI is performed, while a newly modified spatial filtering, similar to one used in some QI schemes, is also developed and employed. This marriage of QI and GI leads to a higher signal-to-background ratio, even after propagating through turbulent media. Combined, these improvements allow for high-contrast quantum correlated imaging through turbulent and noisy channels with acquisition times on the sub-second timescale, opening the door to real-time quantum imaging and recording through free-space.

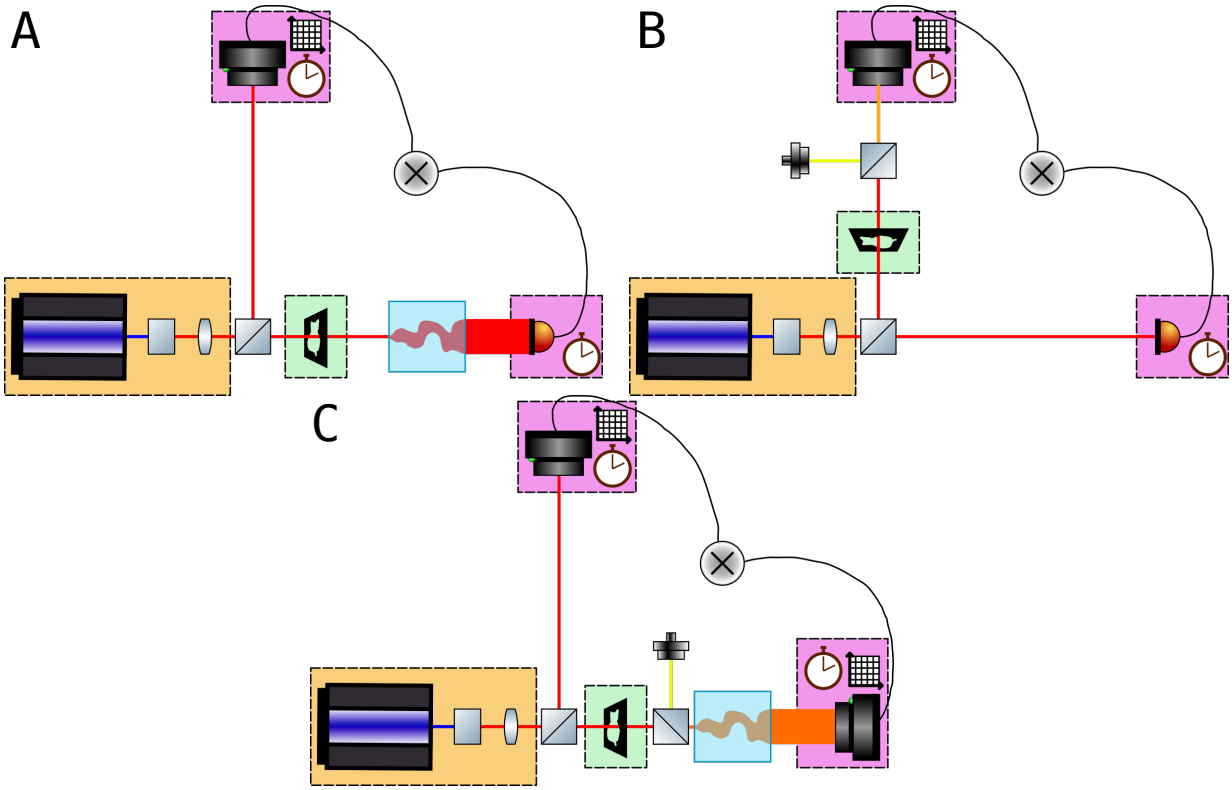

Figure 1.5: **Comparison of Quantum Imaging Setups.** Three different quantum imaging setups are depicted here. There are two traditionally known setups: (A) ghost imaging through turbulent media, and (B) quantum illumination in a noisy channel. One novel setup is depicted (C), which is a hybrid of setups (A) and (B), and depicts quantum imaging though turbulent media in a noisy channel. The property being measured by each device is shown: a clock for time only, and a clock and grid for time and position measurements.

Chapter 2

Theory

2.1 Ghost Imaging Though Turbulence

2.1.1 Assuming Perfect Correlations

There are well known previous works which have explored the theory of ghost imaging through turbulent media [19, 20], thus only a brief conceptual overview of the theory will be given here. Ghost imaging relies upon the second-order correlation between pairs of photons which is given by

$$G^{(2)}(\vec{x_i}, \vec{x_s}) = \langle I_i(\vec{x_i}) I_s(\vec{x_s}) \rangle \tag{2.1}$$

where $I_s(x_s)$ and $I_i(x_i)$ are the measured intensities of a signal and idler produced via SPDC in the far field, respectively, at some positions in the imaging plane x_s and x_i, which correspond to some momenta of the signal and idler photons $\vec{k_{Ts}}$ and $\vec{k_{Ti}}$ at the point of photon pair generation. It is assumed for convenience that the center of each beam is at the respective origin of each of the coordinate systems, and that the area covered by the two beams are equal in size and shape. That is, for the idler beam referred to as the region A_i, the position $\vec{x_i}$ is measured relative to the center of the idler beam, and similarly for the signal beam A_s the position $\vec{x_s}$ is measured from the center of the signal beam. Further, the distance from the center of A_i to the edge of A_i and the distance from the center of A_s to the edge of A_s is

$$\max[\|\vec{x_i}\|] = \max[\|\vec{x_s}\|] \quad \forall\{x_i \in A_i;\ x_s \in A_s\}. \tag{2.2}$$

This can be assured for any two similarly shaped regions by normalizing.

The goal of ghost imaging is to image some target. A target can generally be described by some transmission function $T(\vec{x})$ which has a total transmission of

$$T_{\text{total}} = \int_{\mathcal{R}} |T(\vec{x})| \cdot \vec{dx} \leq 1 \tag{2.3}$$

where $\mathcal{R} \subseteq \mathbb{R}^2$ over which $T(\vec{x})$ is defined (i.e. $\vec{x} \in \mathcal{R}$). Note that if $T(\vec{x})$ instead exists in a Hilbert space as T, then the total transmission is just $T_{\text{total}} = |\det(T)| \leq 1$. This target is placed in the signal beam path, and as such the transmission function is defined in A_s as $T(\vec{x_s})$. It is assumed that the target is placed in the far field of the SPDC source, and also that the imaging is being performed in the far field of the SPDC source. The effect of $T(\vec{x_s})$ is a spatial masking of the intensity of the signal image $I_s(\vec{x_s})$.

A direct anti-linear correlation between the momentum of the signal and idler photons is considered as given by Equation (A.12). When imaged in the far field, the correlation determines that

$$\langle I_i(\vec{x_i}) I_s(\vec{x_s}) \rangle = \langle I_i(\vec{x_i}) \rangle \, \delta_\Sigma(\|\vec{x_i} + \vec{x_s}\|) \tag{2.4}$$

where the function $\delta_\Sigma(\|\vec{x_i} + \vec{x_s}\|)$ here is a linear combination of Dirac delta functions $\forall x_s \in A_s$. This function is only non-zero when $\vec{x_i} = -\vec{x_s}$ $\forall x_i \in A_i; x_s \in A_s$, and the integral over the entire space this function is defined over has a value of 1. This is a mathematical description of the process shown in Figure 1.3.

Ghost imaging is then performed by measuring the full spatial information for $I_i(x_i)$, and bucket detecting all the information in $I_s(x_s)$. This measurement is proportional to

$$\begin{aligned} M_{\text{GI}}(\vec{x_i}) &= \int_C |T(\vec{x_s})|^2 G^{(2)}(\vec{x_i}, \vec{x_s}) \cdot \vec{dx_s} \\ &= \int_C |T(\vec{x_s})|^2 \langle I_i(\vec{x_i}) I_s(\vec{x_s}) \rangle \cdot \vec{dx_s} \\ &= \int_C |T(\vec{x_s})|^2 \langle I_i(\vec{x_i}) \rangle \, \delta(\|\vec{x_i} + \vec{x_s}\|) \cdot \vec{dx_s} \\ &= |T(-\vec{x_s})|^2 \langle I_i(\vec{x_i}) \rangle \end{aligned} \tag{2.5}$$

where $C = A_s \cup A_i$ is the domain which contains all the spatial modes which can be measured, as determined by the aperture of the camera and the interplay of the magnification of the system with the size of the pixels in the camera sensor, and is defined by the mapping $(\vec{x_i}, \vec{x_s}) \to \vec{x_i} + \vec{x_s}$. Thus, the spatial masking from $T(\vec{x_s})$ on the intensity of I_s will be present in $M_{\text{GI}}(\vec{x_i})$, though flipped over the center of A_i. This resolution of the spatial information of the target within the A_i space is the basic premise of ghost imaging.

Now consider some distorting process on the signal photon which does not generate new light. This can be represented by

$$\mathbf{S} : A_s \to A_s^* \quad \text{s.t. } A_s^* \supseteq A_s \tag{2.6}$$

where A_s^* is some new domain which may be larger than A_s (i.e. light can be lost). This representation follows from Equation (A.30). This has the effect that

$$\int_C \mathbf{S} dx_s = V \leq 1 \tag{2.7}$$

where V will be referred to as the "contrast" after the distortion. For the sake of this study it is assumed that the lost light is uniformly random for the strength of distortion and the scale of the experimental setup, though this is not always generally true [20]. Physically, this means that all input modes are still mapped to output modes within the domain A_s^* and no new modes are created in the process, however the output modes which are mapped onto are not unique, and some uniform randomly selected input modes may be mapped to modes which are not measurable by the system.

This coordinate system remapping does not modify Equation (2.4) since the mapping $\mathbf{S}$ is applied to the state after the correlations are considered as

$$G^{(2)}(\vec{x_i}, \vec{x_s})^* = \mathbf{S} G^{(2)}(\vec{x_i}, \vec{x_s}) = \mathbf{S} \langle I_i(\vec{x_i}) I_s(\vec{x_s}) \rangle \tag{2.8}$$

Thus, taking a ghost image through this distortion is then equivalent to

$$\begin{aligned} M_{\text{GI-turb}}(\vec{x_i}) &= \int_C |T(x_s)|^2 G^{(2)}(x_i, x_s)^* \cdot d\vec{x_s} \\ &= \int_C |T(x_s)|^2 \mathbf{S} \langle I_s(x_i) I_i(x_s) \rangle \cdot d\vec{x_s} \\ &= \int_C \mathbf{S} \left(|T(x_s)|^2 \langle I_s(x_i) I_i(x_s) \rangle \cdot d\vec{x_s} \right) \\ &= V M_{\text{GI}}(\vec{x_i}) \end{aligned} \tag{2.9}$$

which is simply the same as in the no distorting case, only with possibly lower contrast due to the lost light from the distortion process.

2.1.2 Effects from Imperfect Correlations

Introducing the effects from imperfect correlations as described in Equation (A.16) to the above theory is relatively straightforward. The effects are introduced in Equation (2.4) as

$$\langle I_i(\vec{x_i}) I_s(\vec{x_s}) \rangle = \langle I_i(\vec{x_i}) \rangle \, g(\vec{x_i} + \vec{x_s}). \tag{2.10}$$

where $g(\vec{x_i}+\vec{x_s})$ is a Gaussian function with width proportional to δk from Equation (A.16) propagated into the far field as $m\delta k$, where m is just the magnification of the optical system which the propagation into the far field occurs within. The normalization of $g(\vec{x_i}+\vec{x_s})$ is such that the integral of it over C is 1.

This results in the ghost image without distorting becoming

$$M_{\text{GI}}(\vec{x_i}) = |(T * g)(-\vec{x_s})|^2 \langle I_i(\vec{x_i})\rangle \tag{2.11}$$

where $(T * gx)(-\vec{x_s})$ is the two-dimensional convolution of $T(-\vec{x_s})$ with $g(\vec{x_i}+\vec{x_s})$. Conceptually, this equates to a blurring of the target's spatial profile, where the kernel of the blurring process is the imperfection of the momentum anti-correlations realized at the measurement plane $g(\vec{x_i}+\vec{x_s})$. This new value for $M(\vec{x_i})$ can be used directly to calculate $M_{\text{GI-turb}}(\vec{x_i})$ following Equation (2.9).

2.2 Quantum Illumination Through Noisy Free-Space Channels

2.2.1 Without Considering Spatial Correlations

Due to a lack of sufficient reference for the derivation of quantum illumination in this form from a quantum perspective, all the work in this section was derived firsthand from basic principles of quantum optics.

Similar to the ghost imaging derivation, quantum illumination is also dependent on the same $G^{(2)}(\vec{x_i},\vec{x_s})$ described in Equation (2.1). The assumptions about the spaces A_i and A_s are the same as described in Section 2.1.1. For the sake of simplicity, the intensities of the signal and idler will initially be considered perfectly anti-correlated. For convenience of this derivation, Equation (2.4) can be rewritten as

$$\langle I_i(\vec{x_i}) I_s(\vec{x_s})\rangle = \langle I_s(\vec{x_s})\rangle\, \delta_\Sigma(\|\vec{x_s}+\vec{x_i}\|) \tag{2.12}$$

with $\delta_\Sigma(\|\vec{x_s}+\vec{x_i}\|)$ as the same summed-Dirac delta function as described before.

The primary difference of QI from GI is that QI in its most basic version is performed by bucket detecting all the information for $I_s(x_s)$, and measuring the full spatial information for $I_i(x_i)$. This measurement is then proportional to

$$\begin{aligned} M_{\text{QI}}(\vec{x_s}) &= \int_C |T(\vec{x_s})|^2 G^{(2)}(\vec{x_i},\vec{x_s})\cdot d\vec{x_i} \\ &= |T(\vec{x_s})|^2 \langle I_s(x_s)\rangle \end{aligned} \tag{2.13}$$

which at first glance may appear to be just regular imaging. In fact, when done in this perfect way, this is true. It is important to point out however that the goal of QI is not to take images in such a perfect scenario, but rather to image through noise.

In order to see the benefits of QI, a scenario considering sources of external noise must also be considered in the calculation. These external sources are considered in only the signal path, resulting in

$$\langle I_s(\vec{x_s})\rangle := \langle I_s(\vec{x_s}) + I_{\text{ext}}(\vec{x_s})\rangle \tag{2.14}$$

where $I_{\text{ext}}(\vec{x_s})$ is the external source intensity in the A_s space. For the context of this derivation there is assumed to be no spatial profile of the external source intensity, and that the external photons can arrive at any location of the sensor with equal probability. As a point of comparison, a direct image of the target, which will be assumed not to interact with the external noise sources, would appear as

$$M_{\text{direct}}(\vec{x_s}) = |T(\vec{x_s})|^2 \langle I_s(\vec{x_s})\rangle + \langle I_{\text{ext}}(\vec{x_s})\rangle . \tag{2.15}$$

In this case, the visibility metric V is

$$V_{\text{direct}} = \text{SBR}(M_{\text{direct}}(\vec{x_s})) = \frac{N(\langle I_s(\vec{x_s})\rangle)}{N(\langle I_{\text{ext}}(\vec{x_s})\rangle)} = \frac{N_{\text{S}}}{N_{\text{ext}}} = \frac{T_{\text{total}} N_{\text{I}}}{N_{\text{ext}}} \tag{2.16}$$

where $N_{\text{S}} \approx N_{\text{I}} \propto \left|\chi^{(2)} E_p L\right|^2$ and $N_{\text{ext}} \propto |E_{\text{ext}}|^2$ are the number of events at the measurement device originating from the signal photons from the SPDC source, and the external noise source respectively, divided by the temporal resolution of the detector δt, and the area of the detector $|C|$. Note that $N_{\text{S}} = T_{\text{total}} N_{\text{I}}$ since the number of signal and idler photons are the same at generation, and the only assumed loss of photons in the system is due to reflection off of or absorption into the target. The timing resolution of the detector is chosen as the coincidencing time windowing in this case, though larger coincidencing time windows can also be chosen.

To begin, the second-order cross-correlation with this new noisy signal results in

$$G^{(2)}(\vec{x_i}, \vec{x_s})^* = \langle I_i(\vec{x_i}) I_s(\vec{x_s})\rangle + \langle I_i(\vec{x_i}) I_{\text{ext}}(\vec{x_s})\rangle . \tag{2.17}$$

The first term's correlations are still described by Equation (2.12), however the second term has a different correlation relationship. In the case of an idler photon and an external source photon, there is no spatial correlation since the measured positions on the sensor of the external source photons will follow a uniformly random distribution. This means that the intensities can be uncorrelated as

$$\langle I_i(\vec{x_i}) I_{\text{ext}}(\vec{x_s})\rangle = \langle I_i(\vec{x_i})\rangle \langle I_{\text{ext}}(\vec{x_s})\rangle . \tag{2.18}$$

Thus, performing QI on such a source results in

$$\begin{aligned} M_{\mathrm{QI}}(\vec{x_s}) &= \int_C |T(\vec{x_s})|^2 G^{(2)}(\vec{x_i}, \vec{x_s})^* \cdot d\vec{x_i} \\ &= \int_C |T(\vec{x_s})|^2 \langle I_i(\vec{x_i}) I_s(\vec{x_s}) \rangle + \langle I_i(\vec{x_i}) I_{\mathrm{ext}}(\vec{x_s}) \rangle \cdot d\vec{x_i} \\ &= \int_C |T(\vec{x_s})|^2 \langle I_s(\vec{x_s}) \rangle \, \delta_\Sigma(\|\vec{x_s} + \vec{x_i}\|) + \langle I_i(\vec{x_i}) \rangle \langle I_{\mathrm{ext}}(\vec{x_s}) \rangle \cdot d\vec{x_i} \\ &= |T(\vec{x_s})|^2 \langle I_s(\vec{x_s}) \rangle + \langle I_{\mathrm{ext}}(\vec{x_s}) \rangle . \end{aligned} \tag{2.19}$$

As should be expected, the resultant imaging process results in the same spatial profiles as in the direct image, and as such the visibility metric is similar, however the number of events in $\langle I_s(\vec{x_s}) \rangle$ and $\langle I_{\mathrm{ext}}(\vec{x_s}) \rangle$ are no longer as straightforward to state as they were before, and instead depend on the intensity correlations

$$V_{\mathrm{QI}} = \mathrm{SBR}(M_{\mathrm{QI}}(\vec{x_s})) = \frac{N(\langle I_i(\vec{x_i}) I_s(\vec{x_s}) \rangle)}{N(\langle I_i(\vec{x_i}) I_{\mathrm{ext}}(\vec{x_s}) \rangle)}. \tag{2.20}$$

To discuss the visibility for QI requires considering the number of identified pairs which can be attributed to each of these factors. To start with the number of pairs in $\langle I_i(\vec{x_i}) I_s(\vec{x_s}) \rangle$, it is considered that all the events in the A_i space are due to idler photons only, and that there are N_{I} of them. Some portion of the corresponding signal photons will be blocked by the target, and this portion is dependent on the transmission of the target T_{total}, as defined in Equation (2.3). Thus, it is considered that the number of idler photons which have possible signal pairs is

$$N_{\mathrm{pairs}} = T_{\mathrm{total}} N_I. \tag{2.21}$$

For noiseless QI this would be the end point, however because of the A_s space having a mixture of signal and external noise photons, there is still more to consider before arriving at the number of $\langle I_i(\vec{x_i}) I_s(\vec{x_s}) \rangle$ pairs.

The addition of the noise photons in the A_s space leads to some proportion of the idler photons arriving with $(n+2)$-fold coincidenced with a signal photon and $n \geq 1$ noise photons. In this case, there are $n+1$ possible pairs with this idler photon, and thus the probability of one of those pairs being the true signal-idler pair is $1/(n+1)$. The proportion of the idler photons which have $(n+2)$ potential coincidences is given by the probability of one or more noise photons showing up in the same coincidence time window as an idler and signal photon. Since the noise photons are from a coherent source $|\alpha\rangle$, the probability of

finding one or more photons at the same time as an idler is given by Poissonian statistics. This results in the number of signal-idler pairs after considering the reduction from the $(n+2)$-fold coincidences as being

$$\begin{aligned} N_{\checkmark\text{pairs}} &= N_{\text{pairs}} - N_{\text{pairs}} \sum_{n=1}^{\infty} \frac{n}{n+1} \mathcal{P}(n) \\ &= N_{\text{pairs}} - N_{\text{pairs}} e^{-N_{\text{ext}}} \sum_{n=1}^{\infty} \frac{n}{n+1} \frac{N_{\text{ext}}^n}{n!} \\ &= N_{\text{pairs}} - N_{\text{pairs}} \frac{e^{-N_{\text{ext}}} + N_{\text{ext}} - 1}{N_{\text{ext}}} \\ &= N_{\text{pairs}} - N_{\times\text{pairs}} \end{aligned} \tag{2.22}$$

where $N_{\times\text{pairs}}$ is the number of accidental pairs from the potential $(n+2)$-fold coincidences. This calculation results in the number of correctly identified pairs in the $\langle I_i(\vec{x_i}) I_s(\vec{x_s}) \rangle$ term, which when expanded is

$$N(\langle I_i(\vec{x_i}) I_s(\vec{x_s}) \rangle) = \frac{N_{\text{I}}}{N_{\text{ext}}} (1 - e^{-N_{\text{ext}}}) T_{\text{total}}. \tag{2.23}$$

To go on to calculate the number of pairs in $\langle I_i(\vec{x_i}) I_{\text{ext}}(\vec{x_s}) \rangle$, the proportion of idler photons which can potentially be paired with external source photons is

$$N_{\text{remaining}} = N_{\text{I}} - N(\langle I_i(\vec{x_i}) I_s(\vec{x_s}) \rangle) - N_{\times\text{pairs}} = (1 - T_{\text{total}}) N_{\text{ext}} \tag{2.24}$$

where $N_{\times\text{pairs}}$ is removed since these accidentals are already accepted as having occurred. Some proportion of these idler photons will be paired with noise photons based on photon time-of-arrival statistics. This is done following a similar calculation as in Equation (2.22). These photons, along with the accidentals $N_{\times\text{pairs}}$ counted during the calculation of the previous metric, are together the total number of accidental pairs

$$\begin{aligned} N(\langle I_i(\vec{x_i}) I_{\text{ext}}(\vec{x_s}) \rangle) &= N_{\times\text{pairs}} + \left(\sum_{n=1}^{\infty} \mathcal{P}(n) \right) N_{\text{remaining}} \\ &= \frac{e^{-N_{\text{ext}}} + N_{\text{ext}} - 1}{N_{\text{ext}}} T_{\text{total}} N_{\text{I}} + (1 - e^{-N_{\text{ext}}})(1 - T_{\text{total}}) N_{\text{i}} \\ &= \frac{N_{\text{I}}}{N_{\text{ext}}} ((1 + e^{-N_{\text{ext}}} T_{\text{total}} - e^{-N_{\text{ext}}}) N_{\text{ext}} + (e^{-N_{\text{ext}}} - 1) T_{\text{total}}). \end{aligned} \tag{2.25}$$

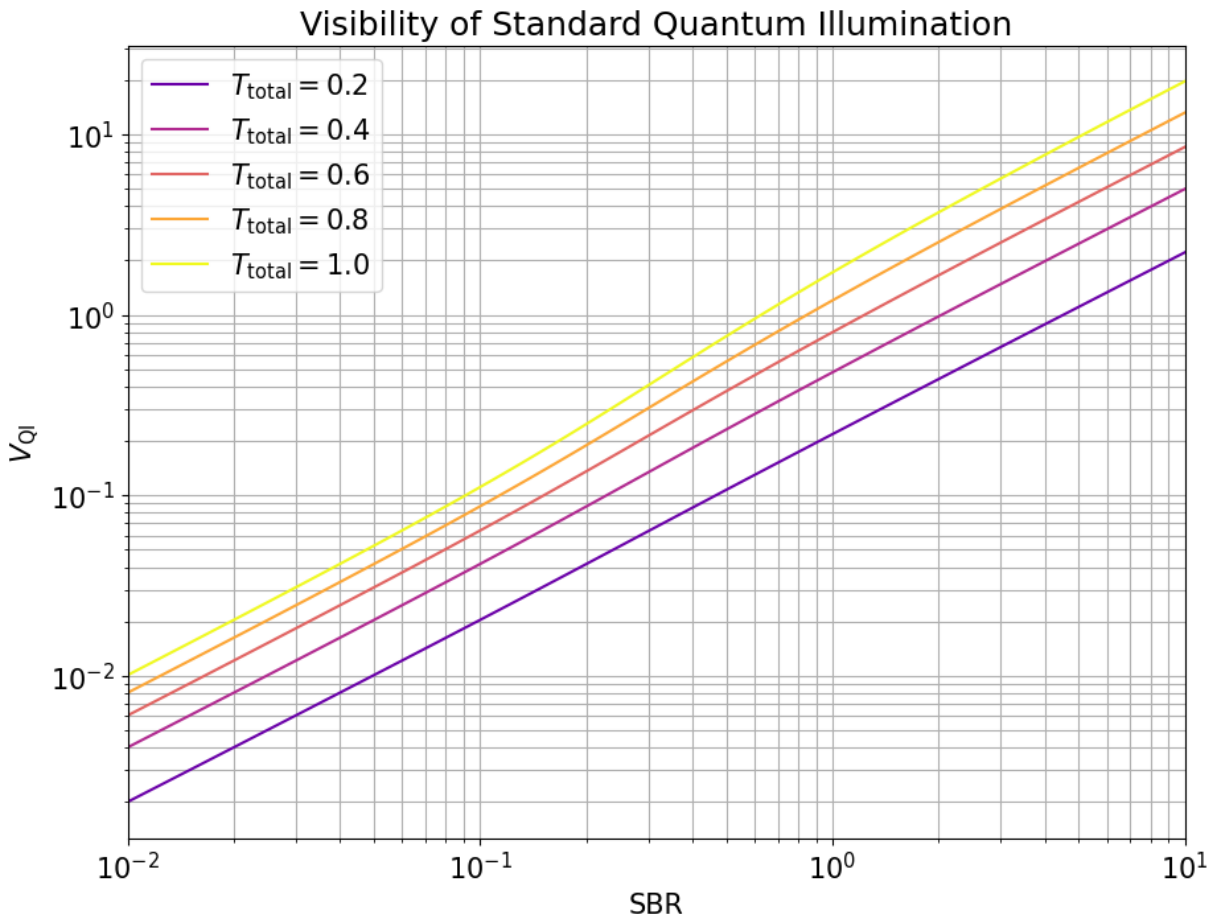

Figure 2.1: **Visibility of Standard Quantum Illumination.** A plot showing the visibility for quantum illumination for targets with different transmission amounts. The visibility of quantum illumination is directly proportional to the SBR, and thus inversely proportional to the intensity of noise. Smaller values of SBR correspond to more noise, and is the region of interest for this imaging method.

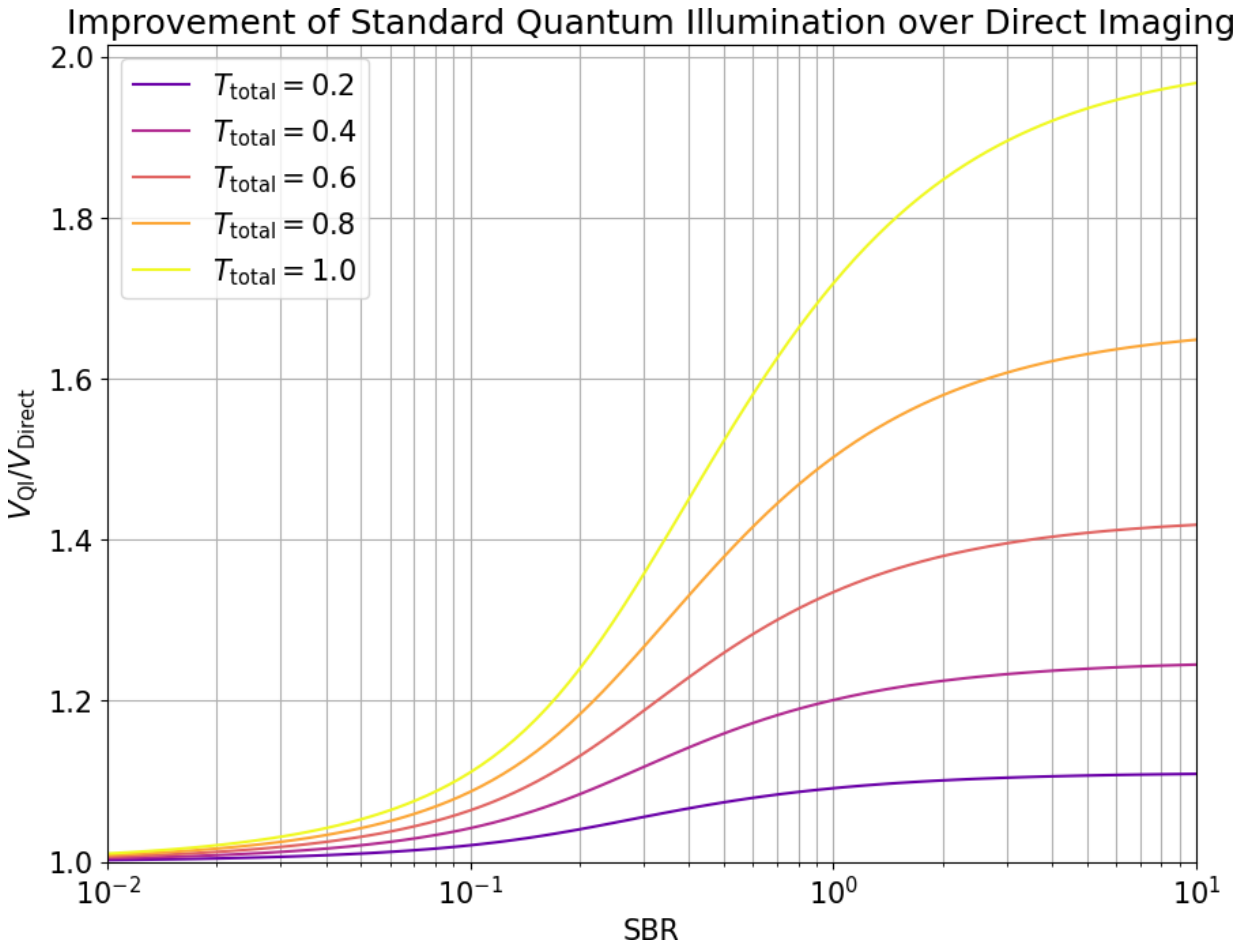

Figure 2.2: **Improvement of Standard Quantum Illumination over Direct Imaging.** A plot showing the improvement in the visibility for standard quantum illumination versus direct imaging, for targets with different transmission amounts. When the noise intensity is an order of magnitude or more than the signal intensity, the visibility of standard quantum illumination converges to that of direct imaging.

The visibility from Equation (2.20) can now be calculated as

$$\begin{aligned} V_{\mathrm{QI}} &= \frac{N(\langle I_i(\vec{x_i}) I_s(\vec{x_s})\rangle)}{N(\langle I_i(\vec{x_i}) I_{\mathrm{ext}}(\vec{x_s})\rangle)} \\ &= \frac{(1-e^{-N_{\mathrm{ext}}})T_{\mathrm{total}}}{((1+e^{-N_{\mathrm{ext}}}T_{\mathrm{total}}-e^{-N_{\mathrm{ext}}})N_{\mathrm{ext}}+(e^{-N_{\mathrm{ext}}}-1)T_{\mathrm{total}})}. \end{aligned} \tag{2.26}$$

To better understand the behavior of this function generally, the variable change $N_{\mathrm{I}}/N_{\mathrm{ext}} \rightarrow$ SBR is performed, and for the sake of plotting, $N_{\mathrm{I}} = 1$. Though this function is difficult to interpret analytically, the general takeaway is that it is inversely proportional to the amount of external noise (Figure 2.1). Graphing the improvement of the visibility for QI over direct imaging in Figure 2.2 for multiple transmission values alongside V_{direct} shows the strengths, and the weaknesses of QI. As for the strengths, regardless of the transmission of the target, the quantum illuminated target is consistently more visible than the direct image at all intensities of noise. Regarding weakness however, once the intensity of the noise is an order of magnitude or more than the intensity of the signal, the QI visibility converges toward that of the direct image.

2.2.2 Considering Spatial Correlations

Given the analysis at the end of the previous section, it is unsurprising that improvements to the basic QI technique have been sought out. While the improvement was originally made as an experimental practicality [35, 47], the use of the spatial correlations as a secondary pairing metric seems like a very logical compliment to the already utilized temporal correlations as a primary metric. In short, the idea is that since the signal and idler pairs already have the strong spatial correlation outlined in Equation (2.12), this can be utilized in the selection of pairs.

Changes to Quantum Imaging when Considering Space

The spatial correlations can be included through a combination of considering their impact on the $G^{(2)}(\vec{x_i}, \vec{x_s})$, and also by considering them when calculating $N(\langle I_i(\vec{x_i}) I_s(\vec{x_s})\rangle)$ and $N(\langle I_i(\vec{x_i}) I_{\mathrm{ext}}(\vec{x_s})\rangle)$. Before beginning on these, the size of the spatial correlations must briefly be considered. Like in GI, the correlations will again have a variance proportional to $m\delta k$ from Equation (A.16). This means that Equation (2.12) becomes

$$\langle I_i(\vec{x_i}) I_s(\vec{x_s})\rangle = \langle I_i(\vec{x_s})\rangle \, g(\vec{x_i} + \vec{x_s}) \tag{2.27}$$

where $g(\vec{x_i} + \vec{x_s})$ is the same Gaussian function from Equation (2.10). Equation (2.18) is unchanged as the idler photons and external filed are still uncorrelated. This results in the QI image being described by

$$\begin{aligned} M_{\text{QI-space}}(\vec{x_s}) &= \int_C |T(\vec{x_s})|^2 G^{(2)}(\vec{x_i}, \vec{x_s}) \cdot d\vec{x_i} \\ &= \int_C |T(\vec{x_s})|^2 \langle I_i(\vec{x_i}) I_s(\vec{x_s}) \rangle + \langle I_i(\vec{x_i}) I_{\text{ext}}(\vec{x_s}) \rangle \cdot d\vec{x_i} \\ &= \int_C |T(\vec{x_s})|^2 \langle I_i(\vec{x_s}) \rangle \, g(\vec{x_i} + \vec{x_s}) + \langle I_i(\vec{x_i}) I_{\text{ext}}(\vec{x_s}) \rangle \cdot d\vec{x_i} \\ &= |T(\vec{x_s})|^2 \langle I_i(\vec{x_s}) \rangle + \langle I_{\text{ext}}(\vec{x_s}) \rangle \end{aligned} \tag{2.28}$$

where the derivation is shown again to point out how here the Guassian spread of the correlations does not affect the target in any way directly, and instead is integrated out. The final visibility, similar in derivation as before is then

$$V_{\text{QI-space}} = \frac{N(\langle I_i(\vec{x_i}) I_s(\vec{x_s}) \rangle)}{N(\langle I_i(\vec{x_i}) I_{\text{ext}}(\vec{x_s}) \rangle)}. \tag{2.29}$$

Calculating Visibility

Moving on to considering the number of pairs in each of the factors of $V_{\text{QI-space}}$, the exact method of spatial filtering must be defined. A detailed discussion of this calculation is given in A.4, where two different spatial filters were investigated. Considering the spatial filter (2), the number of properly identified signal-idler pairs is then

$$N_{\text{pair-space}} = (1 - P_{2\checkmark\times}) N_{\text{pair}} \tag{2.30}$$

where $P_{2\checkmark\times}$ is the probability of a missed signal-idler pair occurring. This is because the number of pairs which are probabilistically missed by the spatial filter must be removed from the set of initial possible pairs.

Next, the possible $(n+2)$-fold coincidences must be considered. In this case, there is a difference as compared to the time-only approach: while the Poissonian statistics of the noise photons' arrival time still holds true, there is a further step in determining whether any of the arriving photons will be considered as a possible pair. The spatial correlation(s) between the idler photon and the extra noise photon(s) must now be satisfied. As such, for each photon which is correlated with the idler photon time-wise, the pair momenta difference is checked against the $g(\vec{x_i} + \vec{x_s})$ function, and if the argument of the function is

within the threshold distance δx, then it is accepted as a possible pair candidate, otherwise it is rejected. Since the noise photons will arrive at the detector with a generally uniform spatial distribution, and independent of the location of arrival of previous noise photons, the accidental acceptance probability is given by $P_{2\times}$. Thus, Equation (2.22) becomes

$$\begin{aligned} N_{\checkmark\text{pairs-space}} &= N_{\text{pairs-space}} - N_{\text{pairs-space}} \sum_{n=1}^{\infty} P_{2\times} \frac{n}{n+1} \mathcal{P}(n) \\ &= N_{\text{pairs-space}} - \frac{N_{\text{I}}}{N_{\text{ext}}} (P_{2\times}(1 - P_{2\checkmark\times}))(e^{-N_{\text{ext}}} - N_{\text{ext}} - 1) T_{\text{total}} \\ &= N_{\text{pairs-space}} - N_{\times\text{pairs-space}} \end{aligned} \tag{2.31}$$

Note that because photons in a biphoton pair are strongly correlated, and that as mentioned in Section A.1.2 this determines the lower bound for the spatial resolution of a quantum imaging setup, it can be generalized that $\delta x \ll |A_s| \Rightarrow 0 < P_{2\times} \ll 1$. This indicates that the amount of accidentals in this case is much less than the amount from the regular QI described in Equation (2.22).

The value for the first proportion is then

$$N(\langle I_i(\vec{x_i}) I_s(\vec{x_s}) \rangle) = (1 - P_{2\checkmark\times}) \frac{N_{\text{I}}}{N_{\text{ext}}} (-P_{2\times} e^{-N_{\text{ext}}} - N_{\text{ext}}(P_{2\times} - 1) - P_{2\times}) T_{\text{total}} \tag{2.32}$$

This leaves a remaining number of idler photons available to pair equivalent to

$$N_{\text{rem.-space}} = N_{\text{I}} - N(\langle I_i(\vec{x_i}) I_s(\vec{x_s}) \rangle) - N_{\times\text{pairs-space}} = (1 - (1 - P_{2\checkmark\times}) T_{\text{total}}) N_{\text{I}}. \tag{2.33}$$

Once more following the same logic, the number of noise photons paired with the remaining idler photons is scaled down based on the proportion of the noise photons which not only show up at the same time, but also within a distance from the idler photon which aligns with the expected spatial correlations. In this case, this is again equivalent to $P_{2\times}$ for each noise photon, and thus

$$\begin{aligned} N(\langle I_i(\vec{x_i}) I_{\text{ext}}(\vec{x_s}) \rangle) &= N_{\times\text{pairs-space}} + \left(\sum_{n=1}^{\infty} P_{2\times} \mathcal{P}(n) \right) N_{\text{rem.-space}} \\ &= N_{\times\text{pairs-space}} + (1 - e^{-N_{\text{ext}}}) P_{2\times} N_{\text{rem.-space}}. \end{aligned} \tag{2.34}$$

Returning now to Equation (2.29), the visibility can be calculated from Equations (2.32)

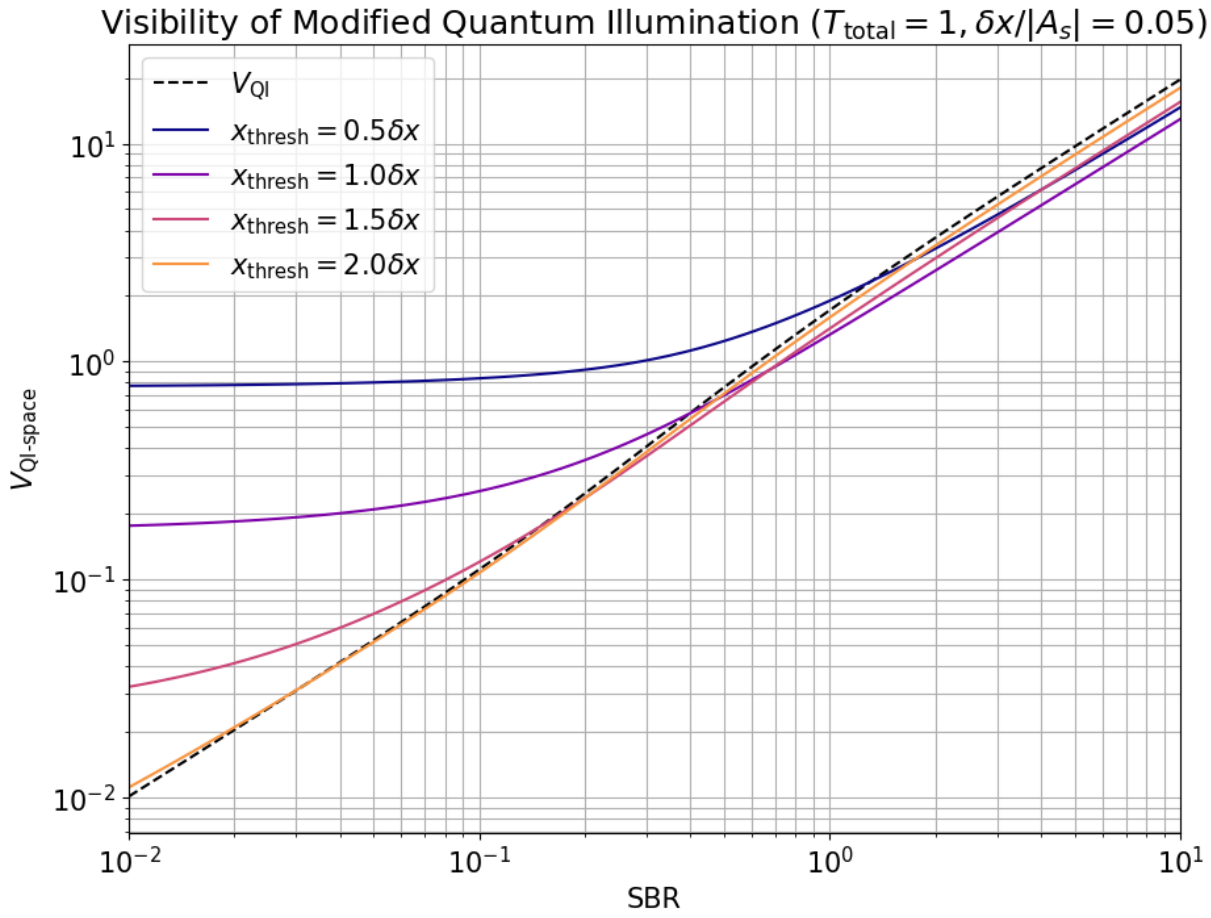

Figure 2.3: **Visibility of Modified Quantum Illumination for Different Thresholds.** The visibility of modified QI is shown for multiple ratios of $x_{\text{thresh}} : \delta x$. The visibility for unmodified QI is also shown as a baseline comparison. The T_{total} for each calculation is set to 1 in order to look at the best case scenario, and the ratio of correlation variance to sensor size is chosen to be $\delta x : |A_s| = 0.05$. As the size of x_{thresh} increases, the visibility approaches that of unmodified QI. For low background noise, modified QI is worse than unmodified QI due to missing some real pairs because of the finite sized filter, though at high background noise modified QI outperforms unmodified QI.

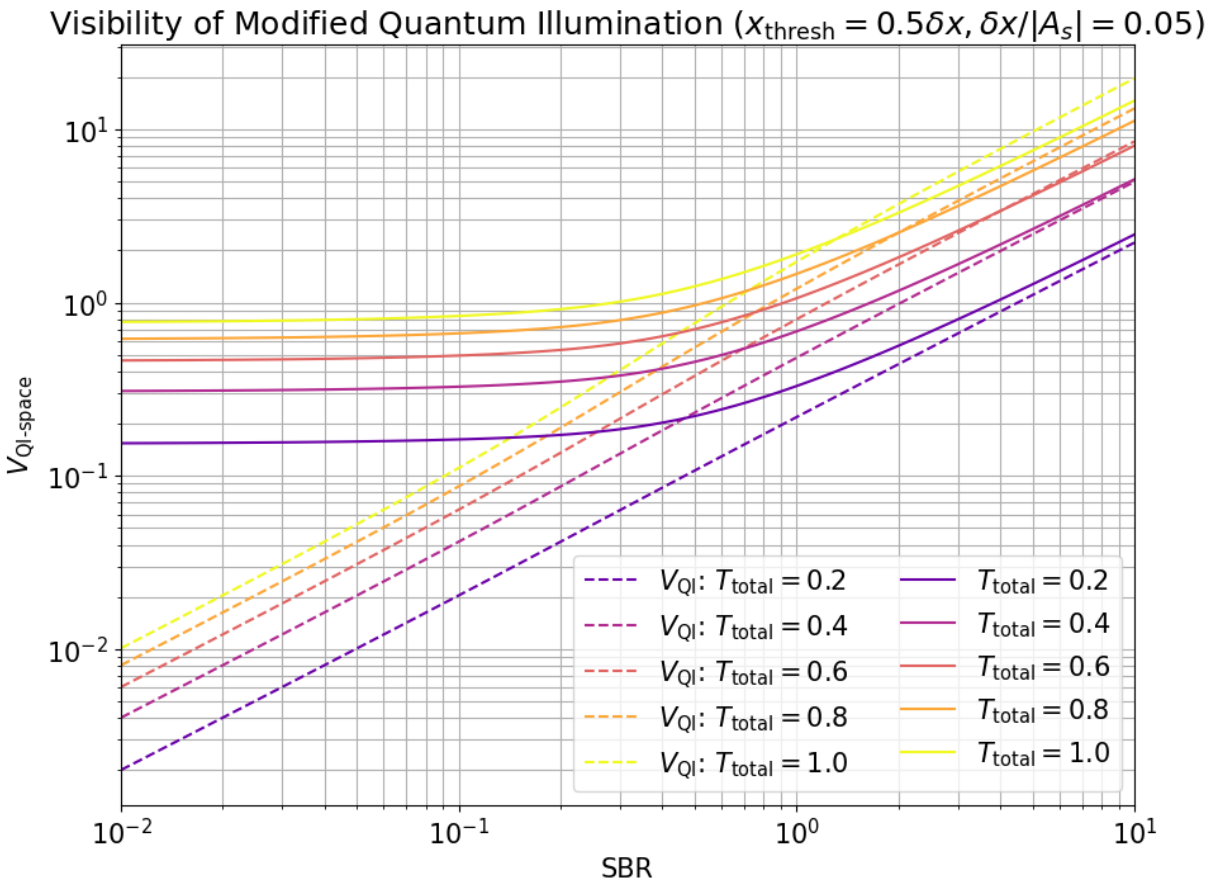

Figure 2.4: **Visibility of Modified Quantum Illumination for Different Transmissions.** The visibility of modified QI is shown for multiple total transmissions. The visibility for unmodified QI is also shown as a baseline comparison. The threshold is set to $x_{\text{thresh}} = 0.5\delta x$ in order to look at the best case scenario, and the ratio of correlation variance to sensor size is chosen to be $\delta x : |A_s| = 0.05$. At higher noise the modified QI is consistently more visible than the unmodified QI, and converges towards a constant visibility, however at low noise the better imaging algorithm is transmission dependent.

and (2.34), which thus gives the visibility as

$$\begin{aligned} V_{\text{QI-space}} &= \frac{N(\langle I_i(\vec{x_i}) I_s(\vec{x_s})\rangle)}{N(\langle I_i(\vec{x_i}) I_{\text{ext}}(\vec{x_s})\rangle)} \\ &= \frac{(P_{2\checkmark\times}-1)T_{\text{total}}\left(e^{N_{\text{ext}}}(N_{\text{ext}}(P_{2\times}-1)-P_{2\times})+P_{2\times}\right)}{P_{2\times}\left((e^{N_{\text{ext}}}-1)\,(P_{2\checkmark\times}-1)T_{\text{total}}+N_{\text{ext}}\,(e^{N_{\text{ext}}}-P_{2\checkmark\times}T_{\text{total}}+T_{\text{total}}-1)\right)}. \end{aligned} \tag{2.35}$$

This calculation is complex, however it can be simplified by acknowledging that both δx and $|A_s|$ are defined by the system, and thus are generally not directly controllable. As a result, $P_{2\checkmark\times}$ and $P_{2\times}$ become constants when x_{thresh} is fixed. Since δx is the variance in the spatial correlations of the paired photons, and thus defines the lower limit in the resolution of the imaging system, it is conservative to estimate that the ratio of $\delta x : |A_s| \approx 0.05$. For simplicity, this will be the used value for all plotting. It is convenient to consider x_{thresh} as a multiple of δx, and the visibility for multiple choices of x_{thresh} are shown in Figure 2.3 with a constant total target transmission of $T_{\text{total}} = 1$. By choosing a tighter filter, it is clear from Figure 2.4 that the modified QI is better at high noise.

It would seem that choosing a tighter spatial filter would always be better, however the visibility metric does not consider that exposures occur over a finite amount of time. A finite exposure time can result in the number of signal photons in the final image being too low to actually render the image. As such, in order to consider this, the fidelity metric would instead be more applicable. The fidelity metric is an experimental metric, and is the one discussed in the results in Chapter 5, however it can be estimated by saying that if $N(\langle I_i(\vec{x_i}) I_s(\vec{x_s})\rangle)t < T_{\text{total}}|A_s|$, then the fidelity is

$$\text{Fidelity}_{\text{QI-space}} = \begin{cases} \frac{N(\langle I_i(\vec{x_i}) I_s(\vec{x_s})\rangle)t}{T_{\text{total}}|A_s|} V_{\text{QI-space}}, & N(\langle I_i(\vec{x_i}) I_s(\vec{x_s})\rangle)t \le T_{\text{total}}|A_s| \\ V_{\text{QI-space}}, & \text{else} \end{cases} \tag{2.36}$$

where t is the exposure time. Explicitly calculating this metric requires knowledge of experimental details, and so will be left as a potential guide for optimizing the choice of spatial filter threshold, rather than as a comprehensive theoretical tool.

One detail which is unconsidered in the previous sets of calculations is that SPDC does not always produce only a single signal-idler pair. Instead, as shown in Equation (A.18), multiple pairs can be generated simultaneously from the same pump photon. Since the photons from these multiple pairs do not all generally have the momentum anti-correlations between them, they are unable to contribute to proper imaging. In a practical setup however, these extra pairs will be spectrally filtered out, so they need not be considered in the counts of N_{I} or N_{S}, though a similar consideration can be made without spectral filtering by only pumping SPDC in the low-gain regime.

2.3 Time-Space Filtered Quantum Correlated Imaging Trough Noisy and Turbulent Free-Space Channels

The full detailed theory for TSFQCI is still being developed, and such is not yet finalized. A general outline of the theory will be given here, however it is worth noting that the final theory will generally follow from the full theories provided in the previous sections of GI through turbulence (Chapter 2.1.2) and spatially modified QI through noise (Chapter 2.2.2). Specifically, the imaging mechanism from GI as explained in Equation (2.11) holds true, while the visibility details from spatially modified QI as explained in Equation (2.29) are approximately correct in the case with no turbulent media present. The primary difference is in the implementation of the spatial filter, which cannot be the same as that of the filter in spatially modified QI. The details of this are explained in the following general outline.

2.3.1 General Outline

To start, the correlations described in Equation (A.9) for time and Equation (A.16) for space are initially assumed. The considerations related to the photon statistics described in the previous section need to be considered in order to construct a full prediction of the visibility for this method. Unfortunately, clarifying the details of these statistics and their effects is still an open problem. Instead, the imaging method is described here less rigorously than the previous imaging methods, however as mentioned this imaging method is a marriage of both GI and modified QI, with some differences outlined below.

Starting with the time filtering, this filter relies upon Equation (A.8), and is applied by removing photon pairs which satisfy

$$\delta t = |t_s - t_i| \geq t_{\text{window}} \tag{2.37}$$

where t_{window} is a chosen coincidence window width. The choice of t_{window} is made such that $t_{\text{window}} \geq$ dToA as given in Equation (A.9), but also must be chosen to be small enough to minimize accidental coincidence counts similarly to the justification given for the fidelity in Equation (2.36). This value is generally constrained by the temporal resolution of the camera. The time filter used here is the same as is used in typical GI described before, and as such provides a robustness against distortions from propagating through turbulent media due to the justification given in Chapter 2.1.2.

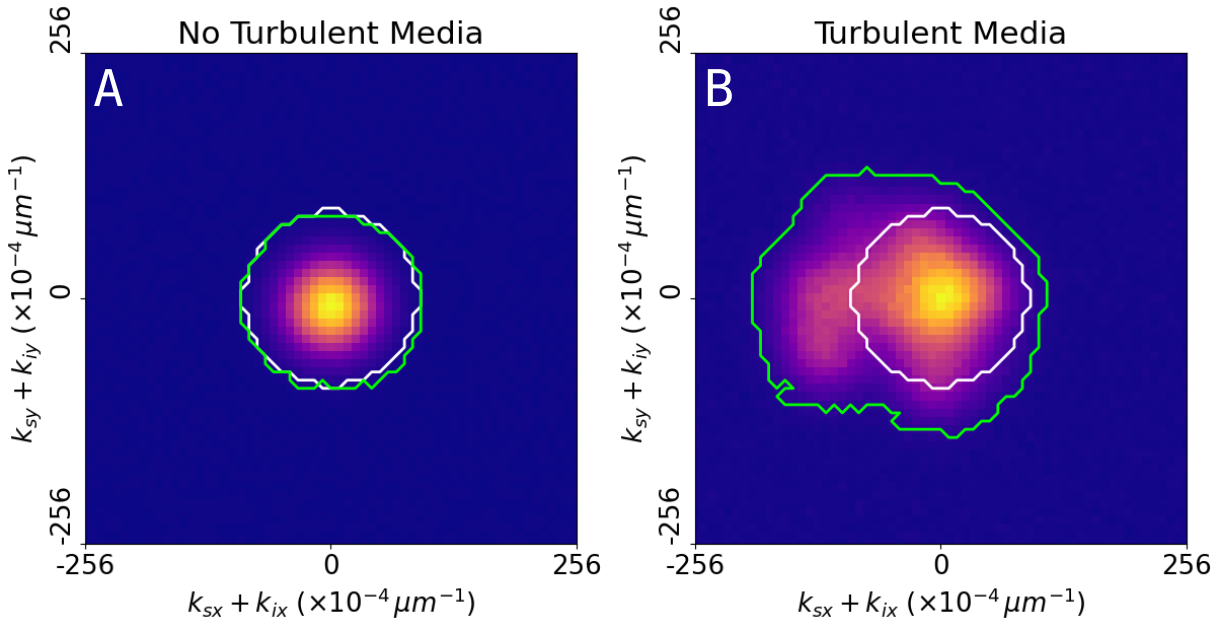

Figure 2.5: **Comparison of Standard and Dynamic Spatial Filters.** A visual depiction of the different function of the standard (white) and dynamic (green) spatial filters. This data set is simulated, and contains only properly paired SDPC events. In the case with no turbulent media present (A), the filters can function identically, and capture almost all real events. When turbulent media is present (B), the standard filter only captures a subset of events, while the dynamic filter still captures almost all real events.

The spatial correlation filter of the method relies upon Equation (A.16), and in the basic case where no turbulent media is present, is applied by removing photon pairs which satisfy

$$\delta k = \left\| \vec{k_s} + \vec{k_i} \right\| \geq k_{\text{window}} \tag{2.38}$$

where k_{window} is a chosen momentum window width (Figure 2.5.A, white outline). Note that δk takes discrete values since $\vec{k_s}$ and $\vec{k_i}$ have discrete values as measured by the camera sensor. This basic spatial correlation filter is the same as is used in modified QI as described before, and as such provides a resilience against background noise from external sources due to the justification given in Chapter 2.2.2. Unfortunately, such a filter will not work as expected if the signal beam propagates through turbulent media (Figure 2.5.B, white outline).

While the propagation of the signal beam through the turbulent media does not destroy the momentum anti-correlations, it does introduce some unknown, non-isotropic set of linear transformations on the signal momentum, as previously described by the mapping $\mathbf{S}$ in Equation (2.6). This mapping originally assumed that light could be lost, and thus that the new signal vector space $A_s^* \supseteq A_s$. For the sake of this argument, consider instead that no light is lost, and thus the vector spaces are isomorphic such that $A_s^* \cong A_s$. Equation (2.38) is still technically a valid filter, however since $\mathbf{S}$ is unknown, and thus $\mathbf{S}^{-1}$ is unknown, $\vec{k_s} = \mathbf{S}^{-1}\vec{k_s}'$ cannot be determined, and thus the simple spatial filter cannot be used as the filter in this scenario.

Inspired by the quantum origin of the momentum correlations, a filter based on the second order correlation between the signal and idler modes is used to identify regions of high correlation. In order to perform this calculation, the normalized second order correlation $g^{(2)}$ metric can be calculated for all possible pairs of signal and idler pixels as

$$g^{(2)}(k_{i,x}, k_{i,y}, k_{s,x}, k_{s,y}) = \frac{\langle I(k_{i,x}, k_{i,y}) I(k_{s,x}, k_{s,y}) \rangle}{\langle I(k_{i,x}, k_{i,y}) \rangle \langle I(k_{s,x}, k_{s,y}) \rangle}. \tag{2.39}$$

Conceptually, the $g^{(2)}$ metric is the ratio of the number of coincident events on a particular pair of pixels to the number of coincident events that would be expected if the photons were completely uncorrelated. For the idler and background fields, which are uncorrelated, it is expected that $g^{(2)} = 1$. Regions in which the $g^{(2)} > 1$ can be generally attributed to correlated events from the pair source. Accordingly, the $g^{(2)}$ function can be deployed as a spatial filter by selecting only regions where $g^{(2)} > 1$. The result is a spatial filter whose shape evolves depending on the scattering, and requires no knowledge of the mapping $\mathbf{S}$ (Figure 2.5.(A,B), green outline).

Since the $g^{(2)}$ function is 4-dimensional, it is difficult to represent it in an intuitive way in 2-dimensions. Instead, a basis change is performed which computes the momentum sum between the two photons in the signal-idler pair, in both the x and y directions. This allows for the momentum correlations to be plotted as a 2D histogram of momentum pair sums, as shown in Fig. 2.5. Determining the effectiveness of this filter is difficult theoretically, thus the reason for the experimental investigation. The visibility can be understood in the limits however since this method converges to either modified QI or GI. With no turbulent media present the visibility converges to that of modified QI (Equation (2.29)) since the dynamic spatial filter is identical to that of the simple spatial filter. When turbulent media with distortions so strong that all spatial information is lost, the method converges to ghost imaging, and thus the visibility is as described in Equation (2.9) applies. Between these two extremes, the visibility is a mixture of the two, and is investigated in later experimentation. The limits of this filter are discussed in more detail in Chapter A.6.

Chapter 3

Experimental Techniques and Unique Devices

3.1 Optical System Design

3.1.1 General Quantum Imaging System

A conceptual overview of the experimental setup is shown in Figure 3.1. Pairs of orthogonally polarized entangled photons at 810 nm are generated through type-II SPDC by illuminating a periodically poled potassium titanyl phosphate (ppKTP) crystal with a continuous wave laser at 405 nm. The pump laser is removed by a long pass filter and the paired photons are collimated using a 100 mm focal length lens. The horizontally polarized signal photons and vertically polarized idler photons are separated by a polarizing beam splitter (PBS), with the upper output port corresponding to the idler beam path, and the right output port corresponding to the signal beam path. Both beam paths are depicted here as ending on two different single-photon sensitive time-tagging cameras. Alternatively, they can end on different parts of the same sensor. The idler arm is directly imaged, while the signal arm has an added target, background noise source, and turbulent media. The target must precede the noise and turbulent media, though the order of the latter two is inconsequential.

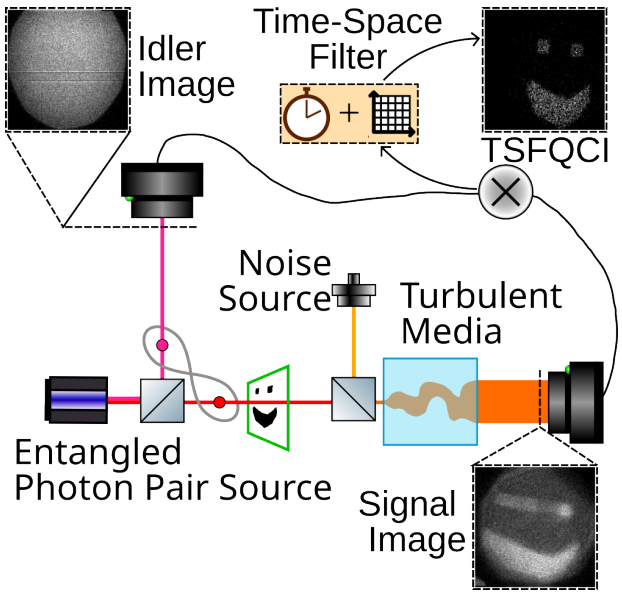

Figure 3.1: **Conceptual TSFQCI System.** A conceptual TSFQCI system. The signal and idler photons are split using a polarizing beam splitter into two paths. The signal beam is partially blocked by a transmissive target and a strong background noise signal is added to the beam via an 808 nm diode laser. The signal beam is then incident on a deformable mirror used to emulate the effects of turbulent media. The two beams are then directed either onto two separate time-tagging cameras or onto two separate regions of a single camera where time and spatial correlation measurements and filterings are performed.

3.1.2 Tunable Noisy Background Source

The used source of noisy background is a diode laser centered at 808 nm, and there are multiple details in the overviews of the system omitted relating to this component. First, since the diode is centered at 808 nm, and since it then goes through the 810 nm bandpass filter (BP-810), this filter acts to lower the intensity of the laser in order to not damage the intensifier of the TPX3CAM. Even with this lowering of the intensity, the beam would still damage the intensifier, and so neutral density (ND) filters were used to further lower the intensity. Lastly, an ND wheel was used to variably control the power of the noisy background. Alternatively, a half-waveplate (HWP) and PBS combo could have been employed to control the power of the noise source.

In a real-world use of TSFQCI within the context of free-space communication, the sources of external noise would be innumerable and varying. The use of a coherent source to emulate such a noisy background is reasonable. This is shown in Chapter A.2.2, where it is shown that the photon statistics of many independent thermal sources follows Poissonian statistics, similar to a coherent laser source. Further, within the context of quantum imaging, the most difficult to discern source of background noise events is that of a coherent laser source. This is due to the photon number statistics of a laser source more closely resembling those of a quantum source than any other single classical source.

3.1.3 Maximizing Correlation Strength — The 4f-Imaging System

The imaging part of the setup was accomplished via a typical $4f$-imaging scheme. If the SPDC source is viewed simply as a backlight to the object, then the imaging lens (Figure (3.2), lens with green outline in the signal arm) is two focal lengths away from the object plane, with the TPX3CAM two focal lengths away from the lens on the opposite side. Since the object plane is set such that it is one focal length after the collimating mirror, which has the ppKTP crystal one focal length before it, this leads to the overall image collected at the TPX3CAM being the far-field of the ppKTP crystal. This is important, as the momentum anti-correlations are used as part of the filtering scheme in TSFQCI, and these anti-correlations are maximized in the far-field of the crystal. Calibrating the system to image the far-field in the signal arm is easy since the object and imaging lenses can both be reliably placed in the correct location, and then the distance of the camera from the imaging lens can be varied to produce the sharpest imaging.

As opposed to the simplicity of the signal arm, calibrating the idler arm to assure that it

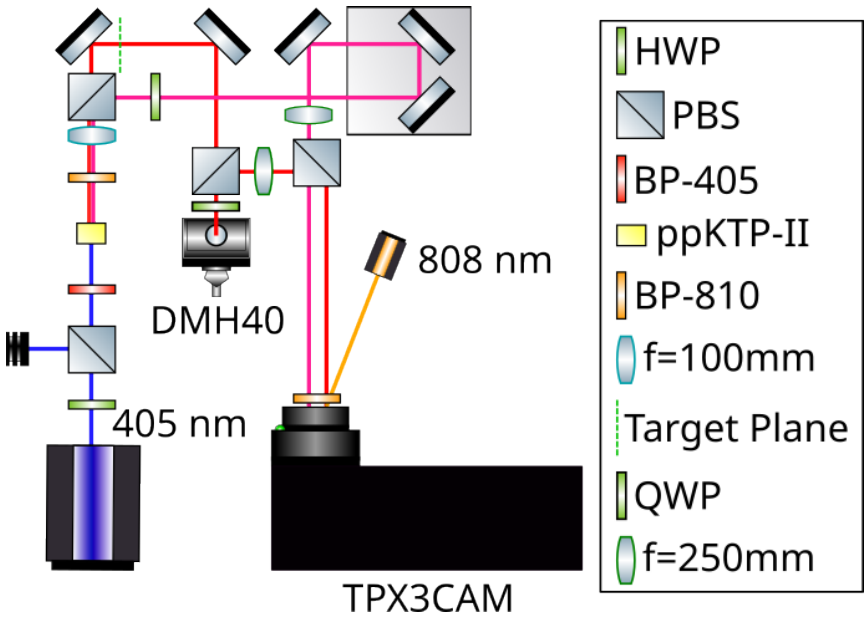

Figure 3.2: **Full TSFQCI Experimental Setup.** A detailed depiction of the full experimental system which allowed for TSFQCI and recording through a tunably-turbulent channel with a controllable noisy background signal. A collimated 405 nm laser was used to pump a type-II periodically poled potassium titanyl phosphate (ppKTP-II) crystal in order to facilitate an SPDC process. This SPDC process acts as a source of paired photons at 810 nm, which are collimated, and then split from each other into the signal (top, orange) and idler (right, pink) photons. The signal beam goes through the object plane, where a transmissive object is placed (either statically for imaging, or on a translation stage for recording). The signal beam is then incident on a DMH40 deformable mirror to emulate the effect of propagating through turbulent media, after which the beam is imaged on the TPX3CAM time-tagging camera using a lens. At the camera, an external noisy background is overlaid on the signal beam via an 808 nm diode laser. After splitting from the signal beam before the object plane, the idler beam travels to two mirrors on a translation stage to allow for varying the optical length of the arm, before being imaged on the TPX3CAM using a lens. The signal and idler beams are imaged on the same camera, but on different parts of the sensor.

is also imaging the far field of the crystal is more difficult. This is a result of the location of the crystal, the location of the camera, and thus the location of the focusing lens all being fixed. The only degree of freedom for calibrating the idler arm is the length of the optical path between the crystal and imaging lens. This length was carefully and painstakingly calibrated by moving optics by hand during the actual system design, however it instead could be accomplished more controllably and reliably by using a translation stage with either two mirrors at 45° from each other as depicted in Fig. 3.2.

3.1.4 Full System Design

A detailed depiction of the system is given in Fig. 3.2, however there are some more careful details which are worth noting. All waveplates used in the design are exclusively used for power control and/or control of which output port of a PBS a specific beam will come out of, and are not used as an integral part of the TSFQCI process. Namely, the half-waveplate (HWP) and PBS combo after the 405 nm source is for controlling the power of the pump, and consequentially the flux of the SPDC within the optical system. Similarly, the quarter-waveplate (QWP) between the PBS and the DMH40 mirror is present to allow the signal beam to be incident on the deformable mirror at a 90° angle via flipping the linear polarization of the beam when it transmits through the QWP twice. The HWP in the idler beam assures that the idler beam will transmit through the combining PBS before the camera after having reflected off the splitting PBS from the signal beam.

As mentioned above, the signal beam was assured to be incident on the deformable mirror at a 90° angle. This has the effect of maximizing the area of the cross-section of the beam which overlaps with the mirror's aperture. This was an important design choice in the system, as the size of this aperture on the mirror limited the size of the SPDC beam after being collimated. Alternatively, a larger beam could be telescoped down to a smaller size to fit within the aperture, however this would add in additional optical components to magnify and demagnify the beam, increasing the overall system size, and also adding more optical losses. In a real use-case scenario where the turbulent media effect is not emulated and controlled, but is instead a result of propagation through an actual turbulent media, this limitation would not be present. The only real use-case limitation on the beam size is related to the sensor size of the camera.

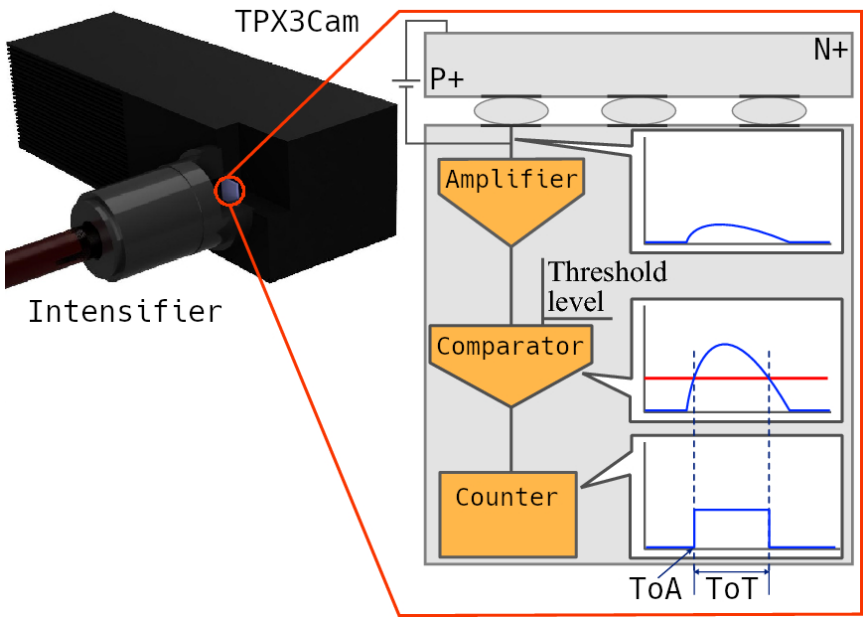

Figure 3.3: **TPX3CAM Diagram.** A diagram of the function of the TPX3CAM detector. The intensifier takes single photon events and converts them into tens of thousands of photons. These photons charge the sensor at pixel locations. The charge is amplified and compared to a threshold. The leading edge of the amplified charge over the threshold is taken as the ToA, while the length of time the amplified charge is over threshold is taken as the time over threshold (ToT). Adapted from [70].

3.2 Unique Devices

3.2.1 Time-Tagging Single Photon Sensing Camera — TPX3CAM

Details on the measurement of single photon position and ToA information at the time-tagging camera has been well-described in previous literature [57, 70]. In order to be sensitive to single photons, a photoelectric intensifier is placed in front of the camera. This intensifier converts a single photon into a cluster of hundreds of thousands of photons, illuminating a small cluster of pixels on the camera sensor with ToA information. By performing a centroiding algorithm on this cluster, both the arrival position and ToA of the single photon can be inferred.

A visual depiction of the pixel triggering mechanism can be seen in Figure 3.3. In order for a pixel to be triggered, the photon clusters are absorbed by the sensor, resulting in a

Table 3.1: **DMH40 Aberrations Range.** The different aberrations which the DMH40 mirror is able to emulate. The standard corresponding Zernike polynomial term for each aberration is provided, along with the OSA+1 indexed term, and finally the physical range available to the mirror for that aberration. A depiction of the Zernike polynomial profiles can be found in Figure A.1 in Appendix A.2

Aberration	Term (OSA+1)	Term (standard)	Aberration Range ($\pm\mu$m)
Astigmatism	Z_4	Z_2^{-2}	18.4
Defocus	Z_5	Z_2^0	17.6
Astigmatism	Z_6	Z_2^2	18.4
Trefoil	Z_7	Z_3^{-3}	6.5
Coma	Z_8	Z_3^{-1}	6.8
Coma	Z_9	Z_3^1	6.8
Trefoil	Z_{10}	Z_3^3	6.5
Tetrafoil	Z_{11}	Z_4^{-4}	5.7
Secondary Astigmatism	Z_{12}	Z_4^{-2}	3.0
Spherical Aberration	Z_{13}	Z_4^0	2.7
Secondary Astigmatism	Z_{14}	Z_4^2	3.0
Tetrafoil	Z_{15}	Z_4^4	5.7

charge in the region of a specific pixel or pixels. This charge is amplified and compared to some threshold value, resulting in a counter signal. The time which the counter signal is above the threshold is also monitored. The leading edge of the counter signal is the ToA, while the width of the counter signal is the time over threshold (ToT). The ToT is utilized to improve the accuracy of the ToA. In total, there are 256×256 pixels.

The spatial resolution of the camera is $55\,\mu$m. The experimental system outlined in Figure 3.2 results in the resolution of the imaging system being equivalent to $8.533 \times 10^{-4}\,\mu\text{m}^{-1}$ in reciprocal space, or $\sim 1\,\mu$m in target space, at the target plane. The temporal resolution of the camera is technically 1.5625 ns, however in practice the uncertainty in the detectors leads to a temporal resolution of 7.3 ns. The quantum efficiency of the sensor is $7.4 \pm 2\%$, with ~ 3 dark counts per pixel per second.

3.2.2 Deformable Mirror — DMH40

In order to emulate the effects of propagating through turbulent media in a controlled and predictable fashion, a deformable mirror was used. The specific mirror, a Thorlabs DMH40, was chosen due to its common use as a wavefront aberration corrector in adaptive optics

systems. The mirror consists of 40 separately deformable sections which are electronically controllable as piezoelectric actuators. Such a physical layout of actuators allows for the mirror to emulate aberrations which can be modeled by linear combinations of Zernike polynomials with coefficients outlined in Table 3.1. The mirror is documented utilizing the Optical Society of America (OSA) standard of Zernike coefficient indexing, with a +1 offset [66]. The tilt aberrations are uncontrollable with the actuators, though are corrected in optical alignment anyhow, while the "piston" or global phase aberration is controlled in this setup by the spacing of optical elements, and has no effect assuming a properly designed and constructed $4f$-imaging system. The mirror has an effective max refresh rate of 3000 Hz. Since the mirror is used effectively in correcting common wavefront aberrations, it is also able to effectively emulate common wavefront aberrations.

3.3 Reference Image Preparation

In order to establish the reference image for the cross-correlation measurement, a 30-second integration time image of the beams with no scattering was taken. The raw image from this measurement was used as the base of the reference image for all cross-correlation comparisons (Figure 3.4, left), however some modifications were performed in order to better match the data as it was measured.

At the camera plane, the signal and idler beams had a slight rotation and magnification difference between them. The raw image has the same orientation as the direct image since the spatial information of both comes from the signal beam, and as such the raw image does not need to be transformed when used as the reference for cross-correlation measurements of the direct image. Since the spatial information of the TSFQCI image comes from the idler beam, the relative rotation and magnification needs to be corrected for in the reference image by applying a transformation to the image (Figure 3.4.T_1). The transformation was applied using the SciPy ndimage package [71], which consisted of a $1 : 1.085$ demagnification, followed by a $-3.5°$ rotation around the center of the image.

Because of the single-photon sensitivity of the camera and the relatively low flux of the SPDC light, even the 30-second integration time reference image has some shot-noise present, as well as an unwanted background. To remove both of these from the reference image at the same time, the image was converted into a binary black and white image by using a threshold cutoff (Figure 3.4.T_2). The threshold value for this cutoff was determined by finding the value which maximizes the cross-correlation maximum value between the reference and the TSFQCI image from the 30-second integration time image. This value was found to be a 40% threshold. Whenever a cross-correlation measurement was

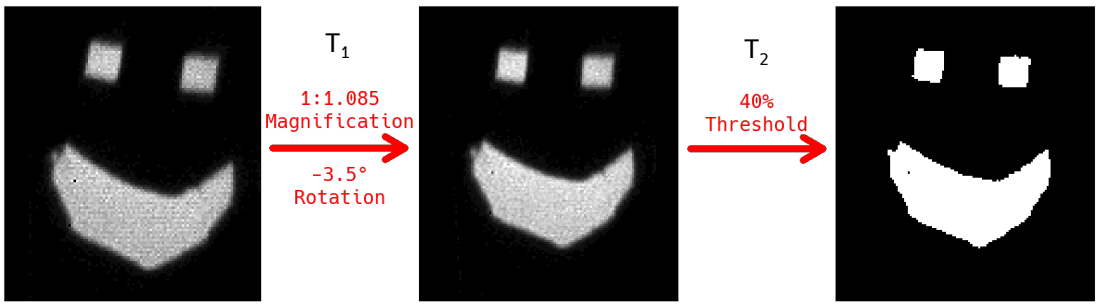

Figure 3.4: **Reference Image Preparation.** The two-step image post-processing performed on the reference image in preparation for a ghost image cross-correlation. The transformation T_1 performs the $1 : 1.085$ demagnification and $-3.5°$ rotation, while the T_2 transformation performs the 40% threshold binary cutoff. For the direct image, only T_2 is performed.

performed on binned data, the reference was also binned after performing all the above described image post-processes.

After these adjustments, the maximized similarity of the TSFQCI image to the reference image in this measurement is 97.1%, establishing this as a fair reference for the correlated images, with the remaining $\sim 3\%$ difference likely being from remaining shot noise in the TSFQCI image.

Chapter 4

Algorithms

4.1 Filtering

Once the data has been processed via parsing, clustering, and coincidencing, it is ready to be filtered in order to produce images. An overview of the filtering process is shown in Figure 4.1. The first column of this figure (A) shows the signal and idler data after coincidencing, where it is clear that there is not yet any advantage to the quantum imaging scheme. At this point, the data is similar to performing ghost imaging with a very large time window, except with the spatial information from both ends of the imaging schemes being resolved. In (B) temporal filtering is performed on the data set, resulting in the data set shown in the center column (C). This data set is similar to performing ghost imaging with a reasonably tight time filter, and as such the undistorted view of the target begins to appear in the idler (C2). Unfortunately, due to the added external noise, the data has a poor signal-to-background (SBR) ratio. For higher noise intensities the ghost image is often not discernible from the background. As such, a spatial filter is applied to this data in (D), and the data set as shown in the right column (E) is the result. This is similar to having taken a ghost image and then applying techniques from spatially-dependent quantum illumination to it, resulting in a high SBR, unperturbed view in the idler (E2). This is the TSFQCI image. Interestingly, a low-noise view of the perturbed target is visible in the signal.

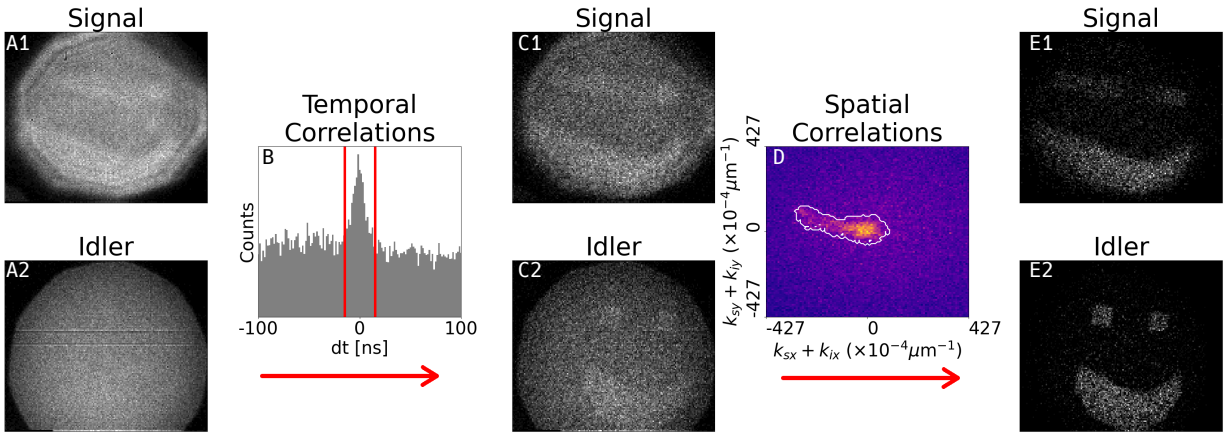

Figure 4.1: **TSFQCI Filtering Overview.** A visual depiction of the temporal-spatial correlation filtering process for imaging a target through turbulent media and background noise with a source SBR of 1 : 15.8. The time filter (B) removes photon pairs that are detected with a time difference larger than the two red lines (± 15 ns here). The resultant signal and idler beam images after time filtering, equivalent to traditional ghost imaging, are shown in (C). The spatial filter (D) selects photon pairs where $g^{(2)} \geq 1$. This is represented by the white outline, where pairs outside the outline are removed by the filter. After the temporal-spatial correlation filters, the correlated image in the idler (E2) is clear with minimal to no background noise, while the direct image in the signal (E1) is still strongly distorted. Each image displayed here is normalized to have a max intensity of 1.

4.1.1 Time Filtering

The time filter theoretically follows directly from the known correlations of photon pairs as produced by SPDC and described in Equations (A.8) and (A.9). As such, it is expected that both photons from a true SPDC pair will arrive at the time-tagging camera at nearly the same time (up to a constant offset). Thus, by simply removing coincidenced pairs with a dToA larger than some tight threshold, the time filter is applied (Equation (2.37)). With the accuracy of the time-tagging camera in this setup, along with the accuracy of the setups alignment and arm balance, it was found that filtering out pairs with a greater than 15ns ToA difference was sufficient for time filtering. With such a time filter, it is possible to observe ghost images.

4.1.2 Space Filtering

The inspiration and theory behind the spatial filter is provided in Chapter 2.3. Figure 4.2 graphically represents the way that the spatial $g^{(2)}$ is calculated. The numerator of the $g^{(2)}$ metric is measured directly from the data after performing the time filter around $\delta t = 0$ as shown in Figure 4.2.(A,D). Here, the bright peak around the origin in Figure 4.2.A is indicative of the high degree of correlation in the light. In Figure 4.2.D, this correlation is distorted by the scattering. The denominator can be approximated to a high degree of accuracy by measuring coincidences between uncorrelated photons. This is achieved by selecting pairs of photons outside the correlation window, (*i.e.* $|\delta t| \gg t_{\text{window}}$). As expected, these pairs exhibit no correlation as show in Figure 4.2.(B,E). At this point, if the measurements were perfect, the spatial $g^{(2)}$ could be calculated directly. Unfortunately, the presence of turbulent media, as well as the finite acquisition time of the data sets, can introduce disadvantageous effects to the spatial $g^{(2)}$. To counteract these disadvantageous effects, modifications are made to the calculation of the spatial $g^{(2)}$. None of these modifications change the underlying physical explanation as to how the filter works, however they are important to note for practical implementation.

The first modification was to deal with issues arising from the finite integration times of the images. Namely, when calculating the normalization component of the spatial $g^{(2)}$ metric from the uncorrelated photon pairs (Figure 4.2.(B,E)), the resultant data set will have many momenta combinations which contain 0 photon pairs. Most of these combinations will occur far from the center of the data set, which is generally the area of interest for this filter. It is still possible however for some combinations which contain 0 photon pairs to occur close to the center. Such combinations will lead to a division by 0 in the calculation of the spatial $g^{(2)}$, and thus will result in undefined values at those locations

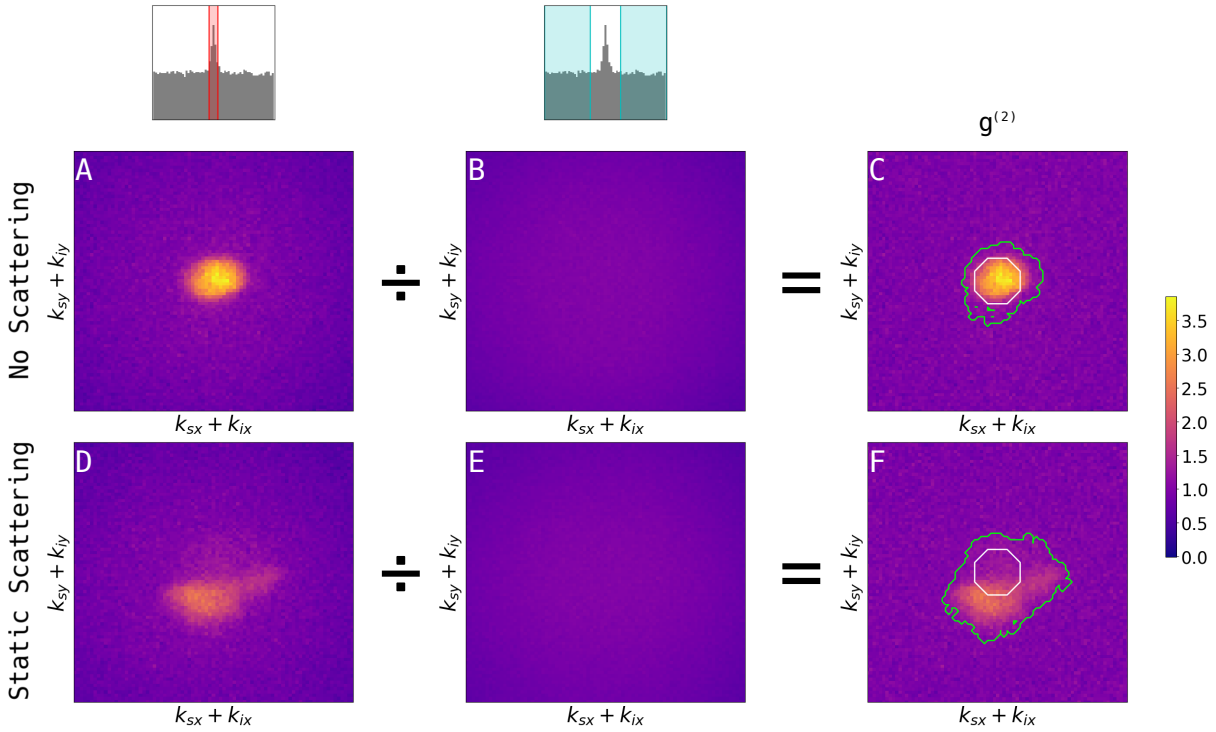

Figure 4.2: **Construction of the Spatial Filter.** A visual depiction of how the $g^{(2)}$ function (C,F) is calculated based on the time filtered data (A,D) and the uncorrelated data (B,E). This is shown for data which contains no scattering (A,B,C) and static scattering (D,E,F) in the signal arm, and in both cases has to target in the signal arm. The filter thresholds are shown for the simple filter (white outline) and the $g^{(2)}$ threshold filter (green outline) in the right-most column.

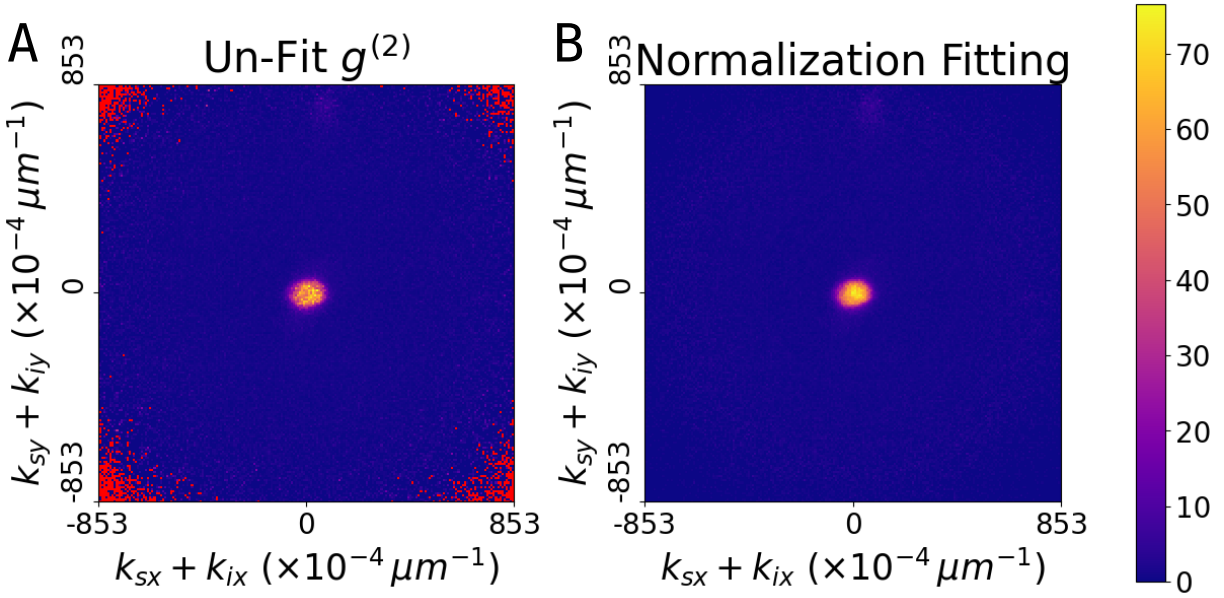

Figure 4.3: **Comparison of $g^{(2)}$ Normalization Fitting.** A comparison of the calculation of the spatial $g^{(2)}$ metric without the uncorrelated data set being fit (A) and with the uncorrelated data set being fit (B), both before using the uncorrelated data set as the normalization value. The bright red values represent where the metric had to divide by zero (i.e. the value is undefined). Here, no target or turbulent media are place in the signal arm, and no added background noise is present. Without the fitting, not only are there issues with undefined values around the edges of the data set, but also the spatial $g^{(2)}$ metric is locally unstable due to increased shot-noise effects. This problem is less pronounced for higher background noise intensities.

(Figure 4.3.A, edges). Similarly, due to shot noise effects, there will be some added variance in the observed number of photons for each momenta combination in the uncorrelated data set. This variance is larger for higher background intensity levels and shorter integration times. This results in a lower signal-to-noise ratio, leading to local instability of the calculated spatial $g^{(2)}$ (Figure 4.3.A center).

To mitigate these issues, the uncorrelated data sets are fit to a super Gaussian of the form

$$\text{fit}(x,y) = A\exp\{\left[-(a(x-x_0)^2 + 2b(x-x_0)(y-y_0) + c(y-y_0)^2)^P\right]\} \tag{4.1}$$

where (x_0, y_0) is fixed to the center of the data set where $(k_{sx}+k_{ix}, k_{sy}+k_{iy}) = (0,0)$, before using it to perform the normalization in calculating the spatial $g^{(2)}$ metric. The amplitude A is taken as the average of values withing 10 bins of the center of the uncorrelated data set, and the rest of the parameters are fit using a least squares fit. Typically, the power of the super Gaussian P is close to 1, however this parameter is still considered, as at lower background intensities or shorter integration times this parameter can be larger. Performing this fit allows for eliminating the effect of the variance in the spatial $g^{(2)}$ metric as caused by finite integration time (Figure 4.3.B, center). Along with the fit as described in Equation (4.1), the uncorrelated data set is further clipped to not be lower than 1 in any calculated location. This removes the divide by zero errors which can occur near the edges of the data set (Figure 4.3.B, edges). Alternatively, areas of the spatial $g^{(2)}$ metric which are undefined could be specially removed by a separate filter, however the clipping allows for the mathematical description as given in Chapter 2.3 to still hold true regardless of the length of time of the data set.

Similar to the uncorrelated data set, the time filtered data set (Figure 4.2.(A,D)) also suffers from variance due to shot noise as a result of the finite data acquisition time. This variance causes the filter to include accidentals due to the statistical chance of the spatial $g^{(2)}$ metric being larger than 1 (Figure 4.4.A). The accidentals could be mitigated by raising the filter threshold value to be higher than 1, as the typical threshold for light to be considered quantum is set at 2. Unfortunately, this only holds true for scenarios where distortions from turbulent media are not present. When distortions from turbulent media are present, depending on the strength of the distortions, the new lower bound for quantum light becomes < 2. The explanation for this is speculated in detail in Chapter A.6, but in brief, the idea is that strong scattering will redistribute the counts in normally correlated spatial bins throughout the entire space of correlated bins. If the normally correlated bins have a $g^{(2)} \approx 2$, and would thus be considered quantum with counts proportional to $g^{(2)} \approx 1$ coming from the SPDC light, then when the SPDC hits are redistributed over say 100 different spatial bins, the new $g^{(2)}$ in bins which do contain SPDC light may be as low as $g^{(2)} \approx 1.01$. As such, the filter threshold value must be set at 1, and some method

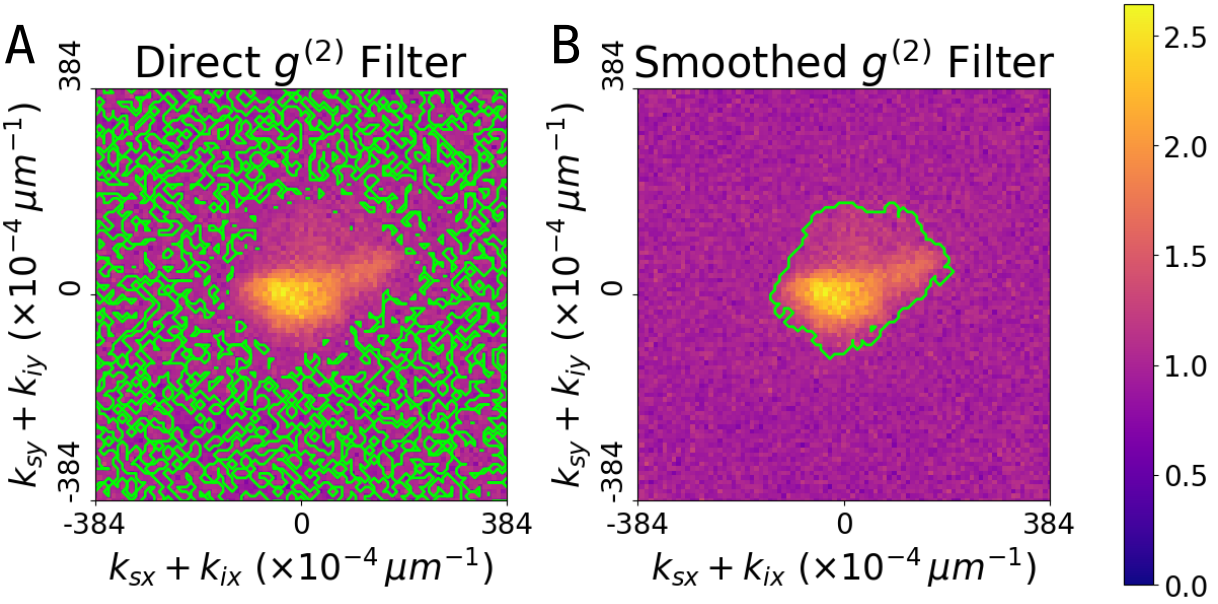

Figure 4.4: **Comparison of $g^{(2)}$ Filter Smoothing.** A comparison of the spatial $g^{(2)}$ filter without smoothing of the included filter values (A) and with smoothing of the included filter values (B). The values preserved by the filter are within the green outline. Here, no target is placed in the signal arm, however both turbulent media and added background noise are present. Without the smoothing, the variance in the time filtered data set due to finite exposure time causes many accidentals to be included within the filter. Due to the possible presence of turbulent media and the unknown target mask profile, the data set cannot be fitted to a known function. Instead, a smoothing is applied to the mask which makes up the filter. This problem is more pronounced for stronger turbulent media and higher background noise intensities.

to mitigate the shot noise variance is necessary to minimize the number of accidentals included in the filter.

Unlike in the case of the uncorrelated data, the time filtered data set may not have a well-defined spatial profile as a result of the distortions from the turbulent media, and the unknown spatial profile of the target. This data set cannot be characterized by an arbitrary class of functions, and thus cannot be fitted in the same way the uncorrelated data set can be. Instead, to mitigate the shot noise variance, a smoothing is applied to the mask which makes up the spatial $g^{(2)}$ filter (Figure 4.4.B). This smoothing is performed by performing an average blurring of the filter mask. The filter mask is treated as an array of 0s and 1s, where a value of 0 means the photon pairs which have that momenta combination will be filtered out, while a value of 1 means the photon pairs which have that momenta combination will be kept in the final data set. This average blurring is applied on each value of the filter mask, and considers the set of 7×7 neighboring values centered on the current value of interest, and checks if the average of that set is greater than 0.8. Mathematically, this is equivalent to performing

$$g_{i,j} = h\left(\frac{1}{49}\sum_{(k,l)=(-3,-3)}^{(k,l)=(3,3)} f_{i+k,i+l}\right) \quad \forall f_{i,k} \in F, g_{i,k} \in G$$
$$\text{s.t. } h(x) = \begin{cases} x > 0.8, & 1 \\ \text{else}, & 0 \end{cases} \tag{4.2}$$

where F and G describe the filter mask arrays before and after the smoothing, respectively. Applying this smoothing results in some amount of shot noise variance mitigation, and consequently accidentals minimization for data sets independent of the turbulent media strength and target spatial profile. The number of accidentals remaining after the minimization is proportional to the intensity of the background noise, and thus for high enough background noise intensity the accidentals will eventually outnumber the true pairs. The combination of both fitting the normalization of the spatial $g^{(2)}$, and smoothing the masking from the spatial $g^{(2)}$ results in the overall spatial $g^{(2)}$ filtering shown in Figure 4.2 and used in Figure 4.1.D.

4.2 Simulating Quantum Imaging

Alongside the experimental demonstration of the imaging scheme, it was beneficial to create an accurate simulation of the imaging scheme. This allowed for testing of many

of the computational techniques and to discern experimental mistakes from computation mistakes. Further, by developing a reliable method to simulate data, exposures which would in practice damage the equipment like high background noise intensities and long exposures could be simulated and investigated to test the limits of TSFQCI separate from the current technological limits of the setup.

4.2.1 Photon Events

To simulate the photon events, only the X-Y location and ToA of each photon must be generated. Any phase, orbital angular momentum, linear momentum, etc. information is not considered in order to be in-line with the information measurable by the TPX3CAM at the imaging plane. Two different types of events can be generated: background noise events, and paired SPDC events. These events require different methods of generation, and so will be described separately.

Background Noise Events

As discussed in Chapter A.2.2, the background noise events can in practice come from many sources following different time statistics, angles of incidence, spacial profiles, etc., and may not even physically originate from photons (i.e. sensor dark counts). Thus, to simulate these events with full accuracy would be infeasible. Chapter A.2.2 shows that since the sources can be considered to be independent, if multiple simultaneous sources are considered, then the photon number statistics follow a Poissonian distribution. This is reflected in the experimental use of a laser to emulate the external sources.

In order to generate random ToAs which follow a Poissonian distribution, a single data set must be considered to be made up of a set of discrete time windows. Conveniently, the TPX3CAM already has a time resolution of 1.5625 ns as stated in Chapter 3.2.1, and also as shown in the example calculation of the ToA from TPX3CAM data as shown in Table A.1.(c). Thus, by knowing the expected number of noise photons which are to be in the final data set, the expected photons per time window can be calculated. Using this value as $\langle n \rangle$ in Equation (A.36) gives the probability of n photons arriving in each time window. Conveniently, both NumPy and CuPy allow for the generation of random integers from a given discrete Poissonian distribution, and as such this generator was used to generate the number of photons in each time window over a given data set exposure time. This distribution is then used to calculate the ToA of each event.

To generate the positions of each event, the uniform spatial distribution assumption from Chapter 3.2.1 was utilized. This assumption could be easily fulfilled by generating two random numbers (p_1, p_2), each in the range $[0, 1)$, and then performing the following calculation

$$\begin{aligned} r &= \sqrt{p_1} \\ \theta &= 2\pi(p_2). \end{aligned} \tag{4.3}$$

The variables r and θ are no longer randomly distributed, however by performing the final transformation

$$\begin{aligned} x &= r\cos\theta \\ y &= r\sin\theta \end{aligned} \tag{4.4}$$

the variables x and y are uniformly distributed over the unit disc. These values can be scaled to fit the size of the expected beam.

SPDC Events

The generation of paired SPDC events is not as simple as the generation of background noise events. To begin, the photon number statistics must be considered. As shown in Chapter A.1, the photon number statistics of an idler or signal photon in isolation follow that of thermal light. The photon number statistics of thermal light follow the Bose-Einstein distribution described in Equation (A.33). As such, the number statistics of both photons as a pair also follow this distribution, but with the transformation $\langle n\rangle \rightarrow \langle n, n\rangle$. This means that, similar to with the noise events, the ToA of the pairs can be generated from this distribution. Similar to with the Poissonian distribution, NumPy and CuPy allow for the generation of random integers from this distribution, albeit with a slight modification. Both provide the function `random.Generator.geometric()`, which generates random integers from the following distribution

$$P_k = p(1-p)^{k-1} \tag{4.5}$$

where p is the probability of success of an individual trial and k is the integer potentially being generated. The Bose-Einstein distribution can be sampled from using this function by performing the following variable reassignment

$$\begin{aligned} p &= \frac{1}{\langle n\rangle + 1} \\ k &= n + 1 \end{aligned} \tag{4.6}$$

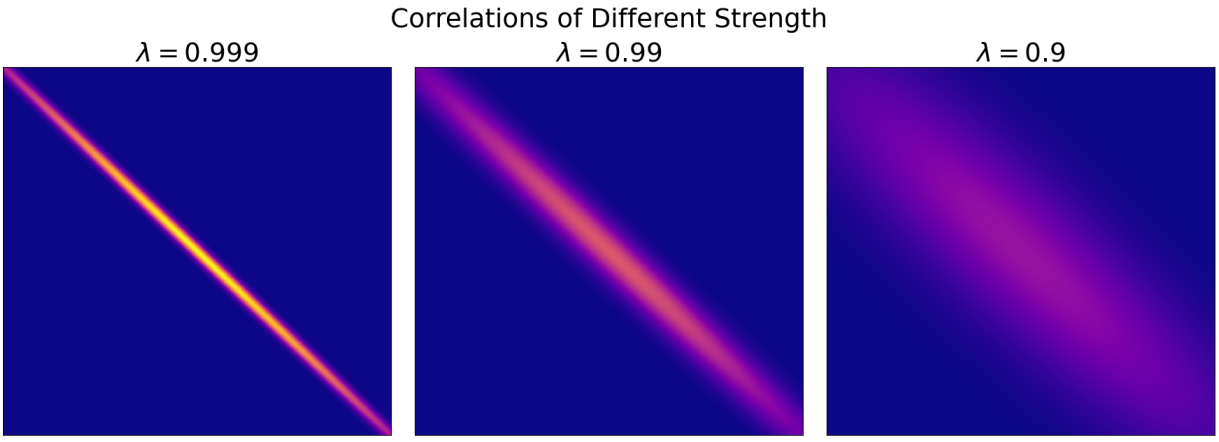

Figure 4.5: **Correlations of Different Strength.** A depiction of differing strengths for spatial correlations which can be used in generating random positions for pairs in SPDC. The brighter colors indicate a higher likelihood of generating a pair where the x-coordinate of the pair is for the idler, while the y-coordinate of the pair is for the signal.

where $\langle n \rangle$ is the expected number of pairs generated per unit time and n is the number of pairs being potentially generated. Once the ToA of the pair is generated, the variance in the ToA between the two photons is offset by a Gaussian distribution, in order to represent the uncertainty in the detector as referenced in Chapter A.1. This results in an accurate simulation of the SDPC photon pair ToAs.

The spatial distributions are again a complex matter. Due to the spatial correlations of the SPDC photons with one another, careful consideration must be taken when approaching the position generation. If the position correlations were perfect as described in Equation (A.12), then the generations of all positions could be done by generating the position of the idler $\vec{x_i}$, and then taking the position of the signal to be $\vec{x_s} = -\vec{x_i}$. Unfortunately, as shown in Equation (A.16), the correlations are not perfect. In fact, with an improper alignment of the system, it is possible for the correlations to be much worse than those outlined in Equation (A.16). Fortunately, this relationship can be easily described by a multivariate normal distribution (Figure 4.5). The spread of an n-variable multivariate distribution is described by an n-tensor called the covariance matrix, rather than the typical scalar variance for monovariate distributions. Here, a two variable multivariate normal distribution is used, and the correlations can be properly adjusted in strength using a covariance matrix of the form

$$\mathrm{K}_{\mathbf{xx}} = \begin{bmatrix} 1 & -\lambda \\ -\lambda & 1 \end{bmatrix} \tag{4.7}$$

where $0 \leq \lambda \leq 1$ is the correlation strength. Two separate distributions are used, one for the x-coordinates of the idler-signal pair, and one for the y-coordinates of the idler-signal pair. After pairs are generated, the pairs are re-scaled to fit within a given beam size. The result is that, individually, the idler and signal positions are distributed with a 2D normal distribution. Considered together, however, the idler-signal pair positions are related by a correlation similar to the one described in Equation (A.16).

Beam modifications were also simulated, though with varying success. As a result, this implementation is discussed in Appendix A.6.1. In short, beam masking was properly implemented, while beam distorting was approximated, though improvements could be made.

Chapter 5

Results

5.1 Validating Algorithms

5.1.1 Simulating Quantum Imaging

An example of a purely simulated TSFQCI system is shown in Figure 5.1 compared to a similar real TSFQCI system output. This system was designed to emulate the included real system, which was initially shown in Figure 4.1. The initial SBR of each of the systems are $1:1.30$ and $1:1.28$ for the simulated and real systems, respectively. This establishes that the initial formulation of the systems in terms of photon counts is comparable. It is clear that the ToA distributions are very similar, though the simulated system appears to have a slightly lower signal-to-noise ratio (5.1b.B vs. 5.1a.B). As a result, the time filtered image in 5.1b.(C2) has a higher SBR of $1:0.36$ as compared to the corresponding real image in 5.1a.(C2) with an SBR of $1:0.53$. The spatial correlations of the simulated system (5.1b.(D)) are more tight and simple than in the real system (5.1a.(D)). This is an effect of the more simplistic distorting algorithm of the simulated system as compared to real distortions from turbulent media. This can also be seen in the noise-reduced direct image, where in the simulated data set (5.1b.(E1)) the distortions are very weak as compared to the real data set (5.1a.(E1)). Due to the combination of the better SNR of the temporal correlations, and the weaker scattering, the fidelity of the simulated system's TSFQCI image is 72.6% (5.1b.(E2)), which is higher than the fidelity of the real system's TSFQCI image of 61.2% (5.1a.(E2)).

It is clear that the simulated system is comparable to a real system, and qualitatively the resultant TSFQCI images are similar. There are some differences however between

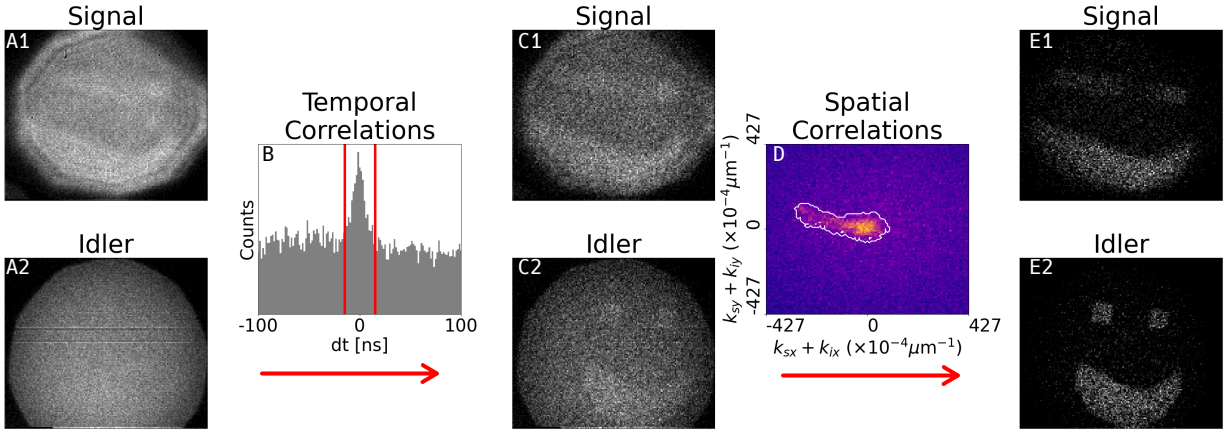

(a) Real System

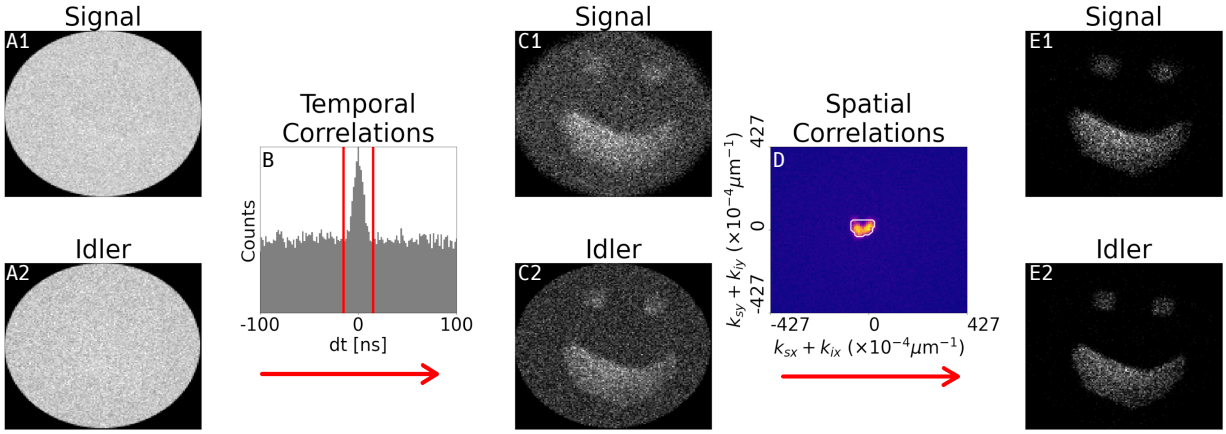

(b) Simulated System

Figure 5.1: **Simulated vs Real Quantum Imaging.** Shown here are the results from a real (a) and a purely simulated TSFQCI system (b). The real system is outlined in Figure 4.1. In the simulated system, 60,000 photon pair events are generated as SPDC pairs (120,000 individual photon events), and 7,200,000 photon events are generated as background events. Of the SPDC pairs, 60% of the signal events are removed by the object mask. After coincidencing ((b).A1), the effective SBR of the initial data set is $1 : 1.30$ before any filtering is performed. The real system has a pre-filtering SBR of $1 : 1.28$ ((a).A1). The signal beam is distorted using a random 5×5 kernel convolved over the entire beam ((b).C). The final fidelity of the simulated TSFQCI image is 72.6%, while for the real image it is 61.2%.

the two, mostly regarding the temporal and spatial correlations. These differences are biased towards more efficient filtering of the simulated system as compared to the real system. Notably however, the time statistics are still quite similar between the two systems. Further, the background noise events' spatial distributions appear very similar, both for the raw events in column A, and also the filtered accidentals in column C. Similarly, the effect of masking the beam to include an image appears very similar between both the time filtered events in column C, and the spatio-temporal filtered events in column E. Likewise, the manifestation of a comparable TSFQCI image for the simulated data indicates that the momentum anti-correlation between the signal and idler photons is a good approximation. In conclusion, while the distortion simulation does not seem trustworthy, the simulations of the noise and SDPC events seem to be sufficiently similar to real events to indicate somewhat about the effectiveness of the TSFQCI imaging process, albeit with the caveat that the process will probably work marginally better on the simulated data.

5.2 Experimental Imaging Results

Overview

Using the experimental system outlined in Chapter 3.1, TSFQCI images were acquired. Images were acquired at two different timescales: the short exposure timescale with 0.5 second integration time, and the medium exposure timescale with 5 second integration time. Within each of these timescale exposures, three different turbulent media regimes are considered: no turbulent media, static turbulent media, and dynamic turbulent media. For each regime, images are through an increasing ratio of background noise intensity to signal intensity, ranging from effective SBRs as low as $1:0.8$, up to $1:82.8$ (that is, $82.8\times$ more noise intensity than signal intensity). The fidelity metric, as described in Chapter A.3.3, is utilized to indicate the similarity of a resultant image to the objective target. The medium exposure data set will be discussed first as the conclusions which can be drawn from it are clearer than those from the shorter data set.

5.2.1 Medium Length Exposures

These data sets show a clear improvement in the fidelity of TSFQCI over direct imaging, for all regimes and noise levels. TSFQCI effectively mitigates both background noise and the distortion effects from turbulent media. The primary benefit of the three regimes is in determining whether TSFQCI is further superior to ghost imaging and quantum

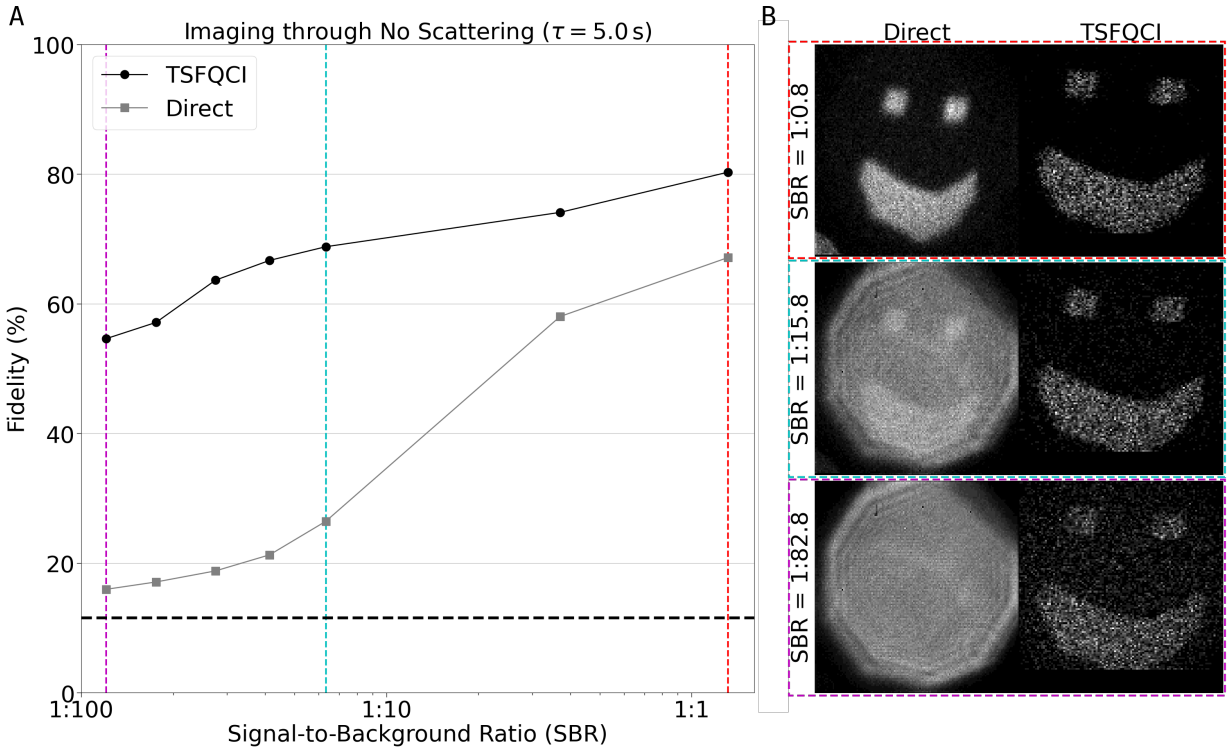

Figure 5.2: **TSFQCI Through No Turbulent Media (5 Seconds).** The fidelity trend for TSFQCI vs direct imaging as noise levels increase for a 5-second integration time and no scattering from a lack of turbulent media in the signal arm (A). TSFQCI has consistently higher fidelity as compared to the corresponding direct image. Samples of the images for selected SBR levels are shown in (B). The black dashed line indicates the fidelity of a beam with no target masking in the signal arm.

illumination individually, and to give an example of a realistic scenario with dynamic turbulent media.

No Turbulent Media

First, in order to establish a baseline, TSFQCI was performed for increasing background intensity with no turbulent media present in the signal arm (Fig. 5.2). This baseline allows for determining whether the fidelity improvement comes purely from the noise robustness granted by the spatial filtering, or if it comes from a combination of the distortion and noise robustnesses from the total TSFQCI imaging and filtering processes. Notably, when no

noise is added into the system intentionally (the SBR of 1 : 0.8 data point), the fidelity of the TSFQCI (80.3%) improves over the fidelity of the corresponding direct image (67.1%) by a relative improvement of 19.7%.

Static Turbulent Media

Figure 5.3 displays the results of TSFQCI through a static turbulent media, and thus static scattering. Here there is a relative improvement with no intentionally added noise of 29.8% (for fidelity scores of 72.8% and 56.1% for the TSFQCI and direct images, respectively). Comparing this to the no turbulent media data set relative improvement of 19.7%, it is clear that the improvement in the fidelity is not exclusively from the noise robustness, but also from the distortion robustness.

Dynamic Turbulent Media

Similar trends in the improvement of the robustness against the noise and distortion can be seen in the data set with dynamic scattering. This dynamic scattering originates from a dynamic turbulent media source updating randomly at 3000 Hz (Fig. 5.4). Comparing the relative improvement for this data set with no intentionally added noise shows a 30.1% improvement (for fidelity scores of 67.7% and 51.7% for the TSFQCI and direct images, respectively), which again is greater than the relative improvement in the baseline, and is comparable to the relative improvement in the static scattering data set. At higher background intensity levels, the improvement in fidelity from the filter begins to fall off quickly. This is due to the lowering of the filter efficacy due to strong scattering, combined with the increase in uncorrelated light $g^{(2)}$ variance due to larger shot-noise effects at higher intensity. Even still, as can be seen in the sample image for an SBR of 1 : 82.8, the target is at least partially distinguishable form the background in TSFQCI, while the same cannot be said of the direct image.

Comparison to Theory

Much of these results are inline with the visibility predictions shown in Figure 2.4. Specifically, the constant visibility of the TSFQCI image at higher noise seems to hold true, at least for the static and no turbulent media cases. Further, the convergence towards being equivalent to direct imaging at lower noise levels is also observed in all three cases.

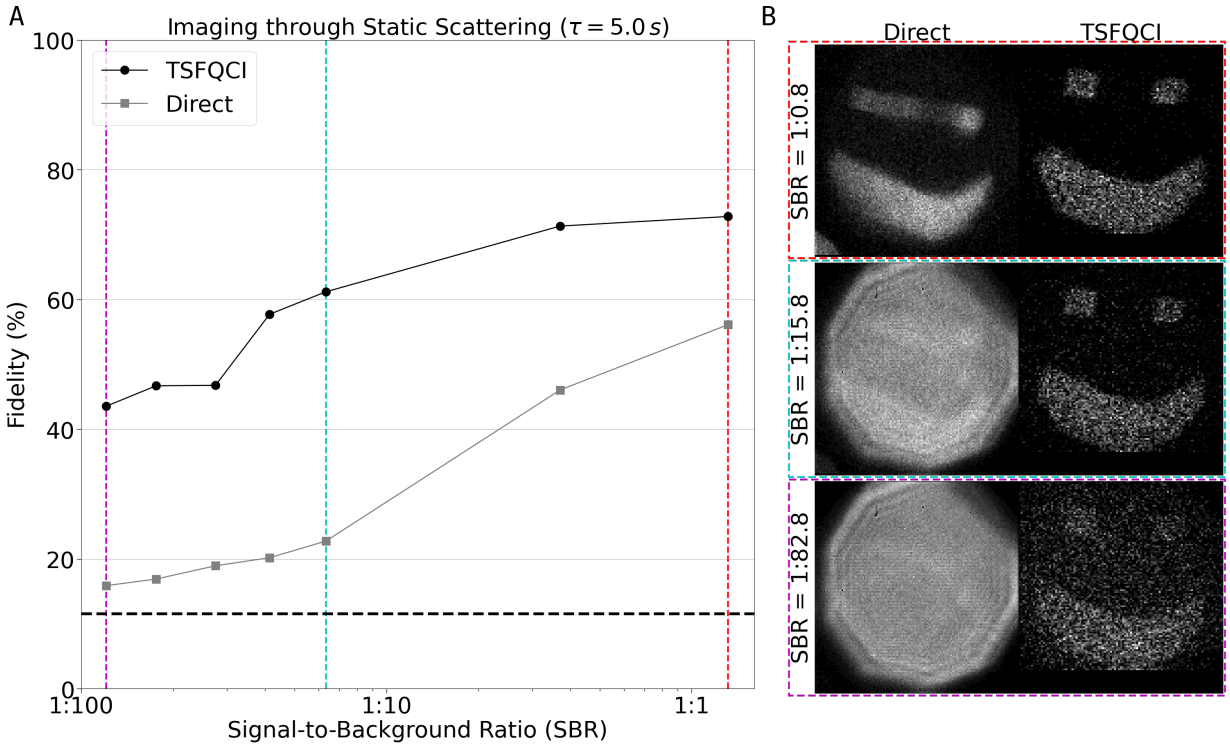

Figure 5.3: **TSFQCI Through Static Turbulent Media (5 Seconds).** (A) The fidelities of the direct imaging vs TSFQCI taken with 5 second integration time through static turbulent media. Examples of the direct imaging vs TSFQCI are shown in (B) for three different SBR levels. The fidelity of the image is consistently higher for TSFQCI than it is for the direct image, across all noise levels. The black dashed line indicates the fidelity of a beam with no mask. Each image displayed here is normalized to have a max intensity of 1.

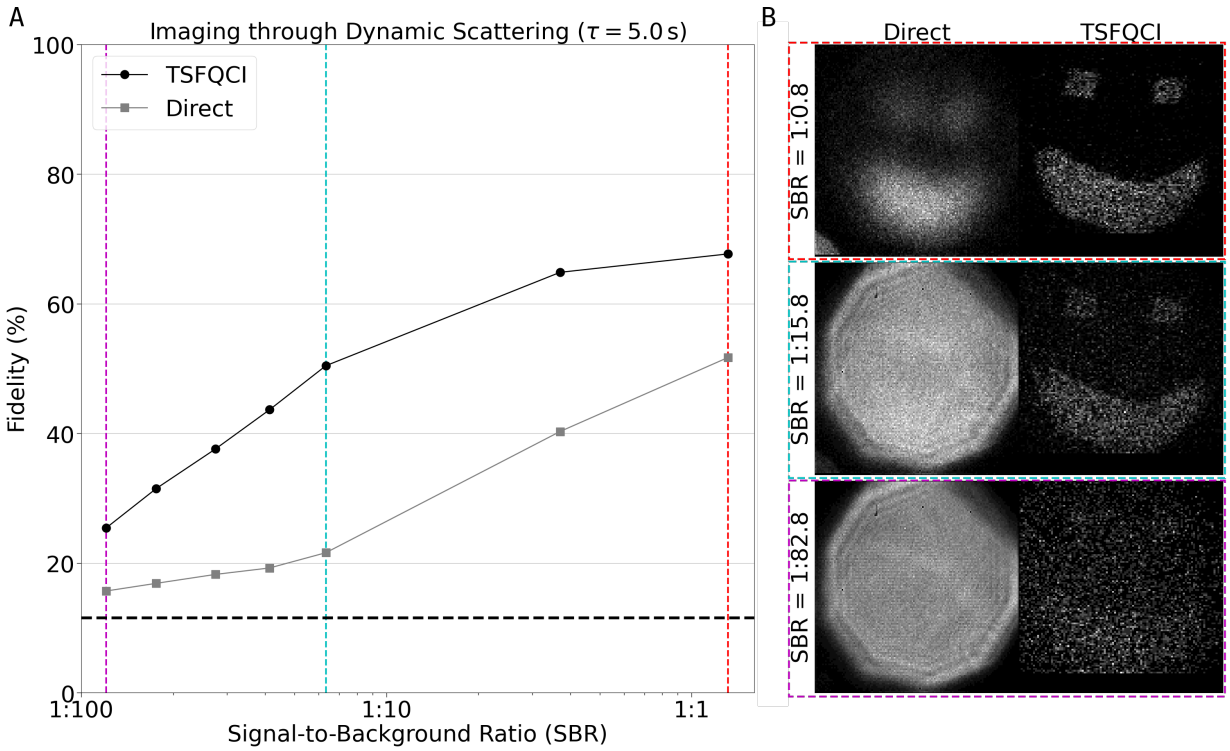

Figure 5.4: **TSFQCI Through Dynamic Turbulent Media (5 Seconds).** The fidelity trend for TSFQCI vs direct imaging as noise levels increase for a 5-second integration time and dynamic scattering from turbulent media changing at a rate of 3000 Hz (A). TSFQCI has consistently higher fidelity as compared to the corresponding direct image. Samples of the images for selected SBR levels are shown in (B). The black dashed line indicates the fidelity of a beam with no target masking in the signal arm.

5.2.2 Short Exposures

These data sets show an increase in fidelity for all regimes and background intensities, however the quantitative improvement is not large. This is a result of low photon counts in the TSFQCI image after filtering, thus lowering the fidelity such that confidence in the increase is not as clear. Since the number of observed events in the shorter data sets are approximately 1/10 of those in the medium data set, the resolution of the camera was dropped to be 1/3 of the native resolution, increasing the number of events per pixel by ~ 9 times. This was accomplished by performing a 3×3 spatial binning of the data after coincidencing and performing the time filter.

No Turbulent Media

A quick drop off in the fidelity is well illustrated for the shorter data set with no scattering (Fig. 5.5). Notably, while the relative fidelity improvement starts off at a 23.1%, which is comparable to the 19.7% improvement shown above for the longer data set, the improvement ends with a relative improvement of 89.3% over the direct image fidelity, while the longer data set showed a relative improvement of 242.1%. It can also be seen that the direct image fidelity here is comparable to the direct image fidelity for the longer data set, which supports that the decision to spatially bin the data is valid. Otherwise, without spatially binning the data, the direct image fidelity is much lower.

Static Turbulent Media

Similar to the data set with no scattering, the shorter data set with static scattering shows an improvement over the direct image fidelity with a faster drop-off when compared to the corresponding longer data set (Fig 5.6). The initial relative fidelity improvement is 27.5%, again comparable to the longer data set, but the final relative improvement is 111.3%, while for the longer data set it was 174.2%. It is worth noting that because the configuration of the deformable mirror was set randomly, the static scattering for the short data set seems to be subjectively stronger than it was in the longer data set. This may be why the drop-off in this case was comparatively slower than it was in the short no scattering case, as the fidelity improvement resulting from the distortion robustness will be greater in this case compared to the longer data set.

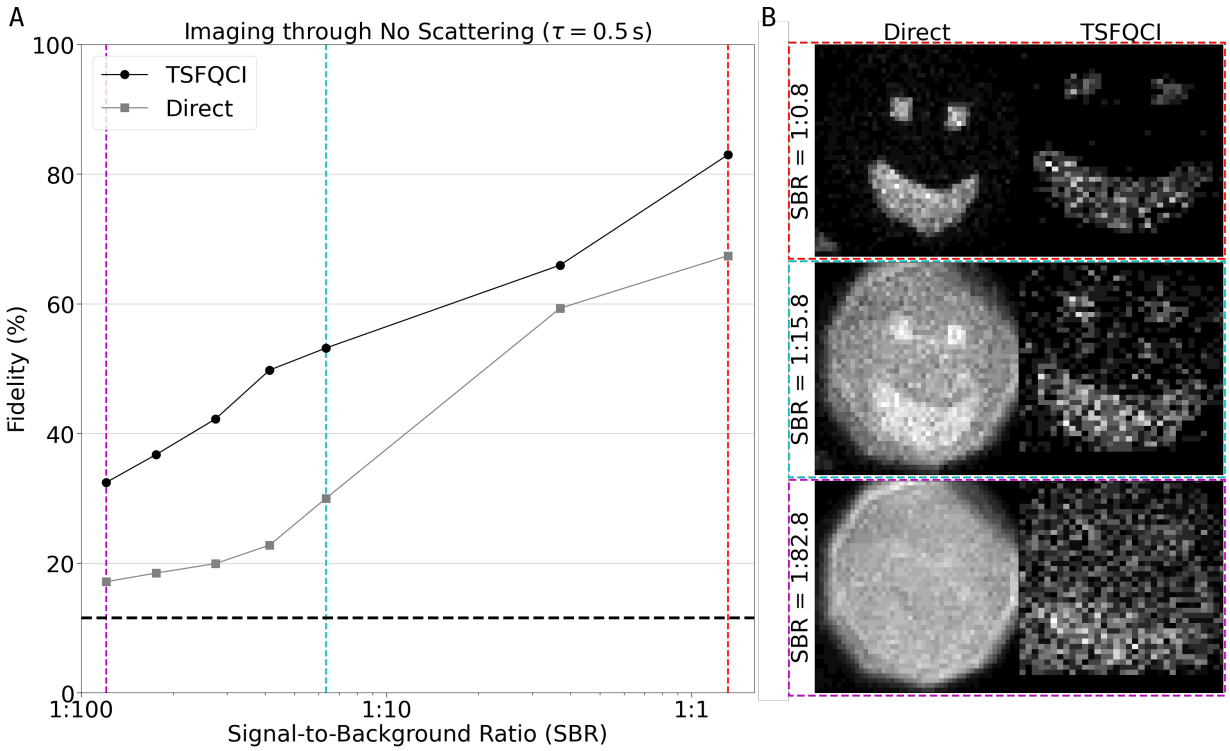

Figure 5.5: **TSFQCI Through No Turbulent Media (0.5 Seconds).** The fidelity trend for TSFQCI vs direct imaging as noise levels increase for a 0.5-second integration time and no scattering from a lack of turbulent media in the signal arm (A). A 3×3 spatial binning was applied to both data sets to account for the low number of photons in the images. TSFQCI has consistently higher fidelity as compared to the corresponding direct image. Samples of the images for selected SBR levels are shown in (B). The black dashed line indicates the fidelity of a beam with no target masking in the signal arm.

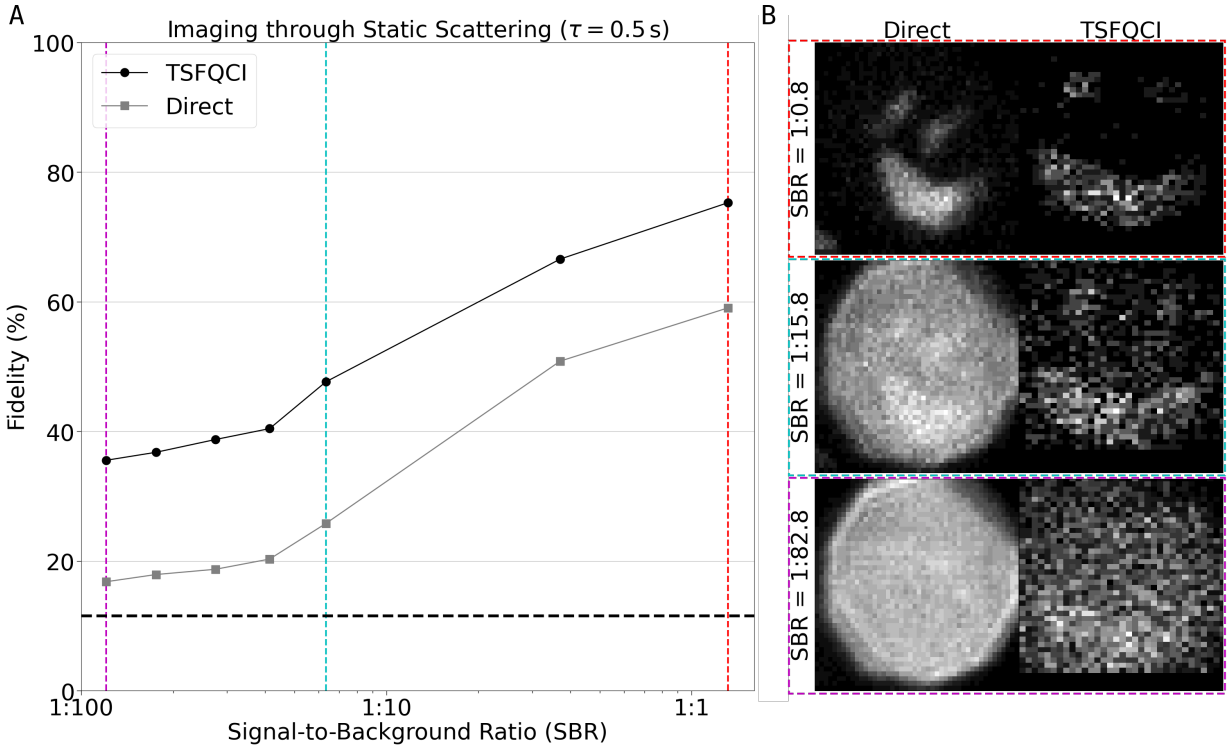

Figure 5.6: **TSFQCI Through Static Turbulent Media (0.5 Seconds).** The fidelity trend for TSFQCI vs direct imaging as noise levels increase for a 0.5-second integration time and static scattering from turbulent media in the signal arm (A). A 3×3 spatial binning was applied to both data sets to account for the low number of photons in the images. TSFQCI has consistently higher fidelity as compared to the corresponding direct image. Samples of the images for selected SBR levels are shown in (B). The black dashed line indicates the fidelity of a beam with no target masking in the signal arm.

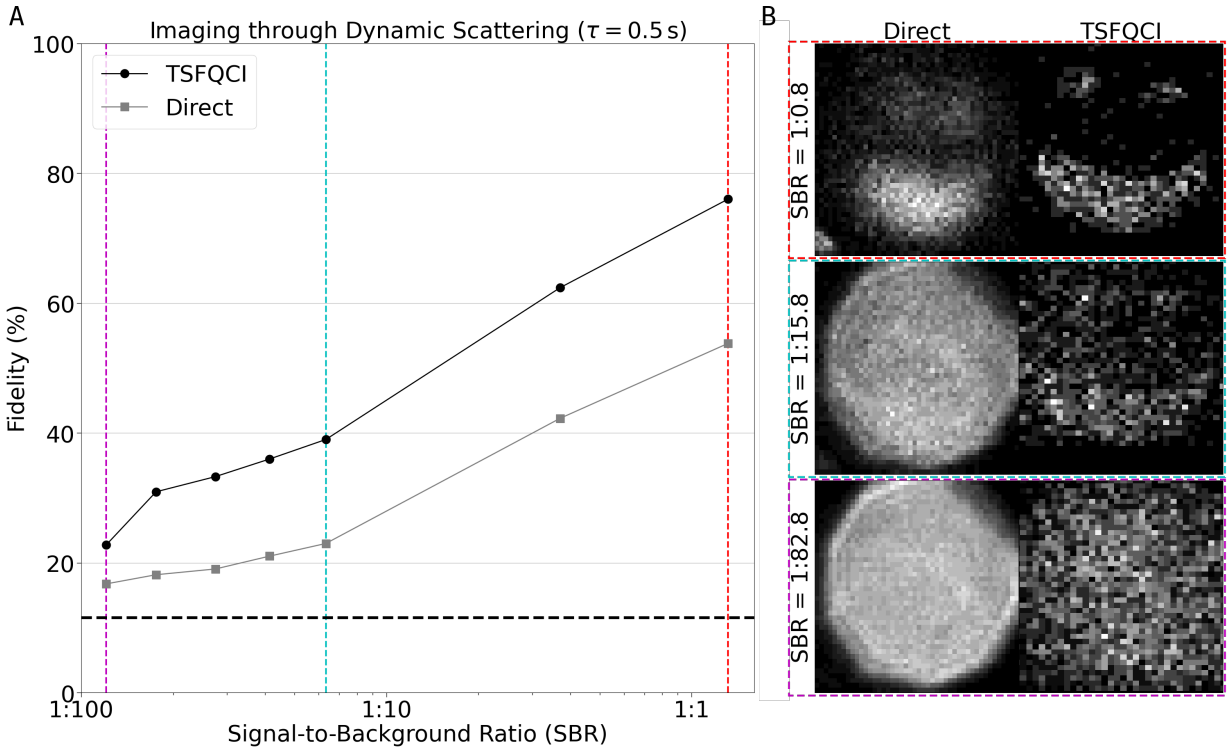

Figure 5.7: **TSFQCI Through Dynamic Turbulent Media (0.5 Seconds).** The fidelity trend for TSFQCI vs direct imaging as noise levels increase for a 0.5-second integration time and dynamic scattering from turbulent media changing at a rate of 3000 Hz (A). A 3×3 spatial binning was applied to both data sets to account for the low number of photons in the images. TSFQCI has consistently higher fidelity as compared to the corresponding direct image. Samples of the images for selected SBR levels are shown in (B). The black dashed line indicates the fidelity of a beam with no target masking in the signal arm.

Dynamic Turbulent Media

Finally, the shorter data set with dynamic scattering shows similar results, though for higher background noise intensity the TSFQCI process seems to cease being effective (Fig. 5.7). The original relative fidelity improvement is 41.3% and in-line with the longer data set, but at the end the relative fidelity improvement starkly drops to 35.9%. It is clear from the inset that any spatial information about the target has been lost at this noise level. This is because the SNR of the signal to the noise from the added background signal is so low that there is almost no way for the filter to distinguish these two types of information in the $g^{(2)}$.

Comparison to Theory

It is worth noting that the worse improvement at high noise of the shorter data set is inline with the theoretical visibility shown in Figure 2.3. This is because in this case the ratio of the filter variance to sensor size is higher due to the spatial binning of the data.

5.2.3 Comparing TSFQCI to GI with Background Subtraction

It is important to note that the drop in fidelity at higher background intensities is not due to an increase in the signal-to-noise ratio (SNR). To support this, a measurement set was processed in two ways: via the TSFQCI method described here, and via a flat background subtraction which maximized fidelity. It was shown that no matter how much flat background was subtracted, the TSFQCI image has higher fidelity, supporting this noise robustness argument.

Overview of GI with Background Subtraction

Since the main observed effect of the TSFQCI process is an increase in the SBR of the original image, and further an increase in the SBR of a corresponding ghost image, an often raised question has been whether this method is equivalent or comparable to performing a simple background subtraction on a ghost image. The results in Figure 5.8 clearly show that the TSFQCI process is both different from and superior to GI with a background subtraction. For the TSFQCI in this case the fidelity was observed to be 57.7%, while for the GI where the background was subtracted in order to be at the same level as in the TSFQCI image, the fidelity was observed to be 31.2%. Thus, there is a relative increase

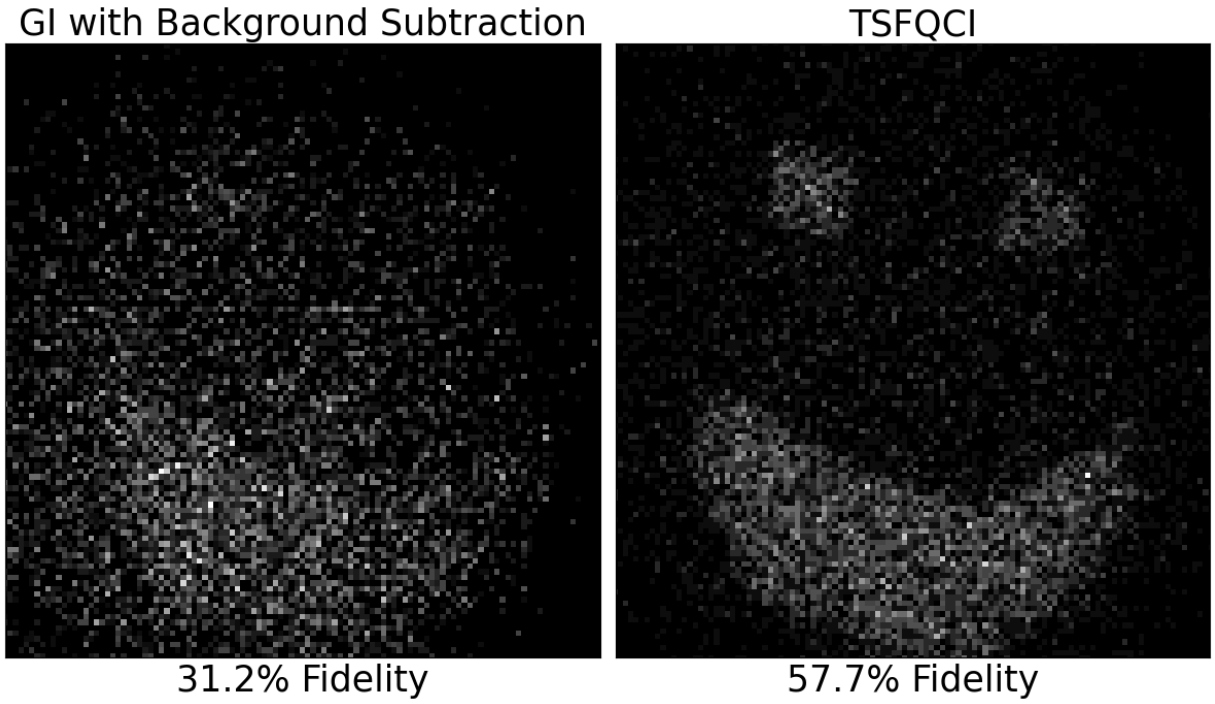

Figure 5.8: **TSFQCI vs. GI with Background Subtraction.** A comparison between performing a simple background subtraction on a ghost image (A) and the TSFQCI process (B) on the same original image. Here background was added to the original image experimentally to make an observed SBR of $1 : 24.2$. The background subtraction is simply a flat subtraction from the already time-filtered image to make the background region of the subtracted image to have the same mean level as in the TSFQC image.

in fidelity of the TSFQCI over the background subtracted image of 84.9% and this effect can be seen qualitatively in the resultant images shown in Figure 5.8.

This indicates that the TSFQCI process works to selectively prioritize lowering the background intensity more than the intensity of the signal. This is inline with filtering by the momenta anti-correlations, as the filtering specifically targets removing photon events which originate from accidental coincidences rather than photon events which originate from the SPDC source, or generally any random photon event, as is the case in GI with flat background subtraction. A reasonable equivalence to be made would be a scenario where the signal region was already known, and then background subtraction was performed on GI only outside the signal region. Here, rather than the signal region being known beforehand, it is instead inferred from the correlations between the SPDC photon pairs, thus performing the image reconstruction of ghost imaging at the same time as performing the decrease in background intensity of quantum illumination.

5.3 Recording Results

5.3.1 Video through Dynamic Scattering

To simulate a changing signal being transmitted through turbulent media, the object was recorded translating across the beam at a constant velocity. Dynamic scattering was performed by reassigning the random weights of the fourth to fifteenth Zernike polynomial terms with a refresh rate of 100 Hz. This rate is similar to the rate of change of turbulence in water [13], and was chosen to make the distortion appear more dynamic in real time. It is important to note that a higher refresh rate would produce comparable results for the TSFQCI frames since the filtering is dependent on the distribution of the correlations, and for any rates including 100 Hz and above the distribution is a similar Gaussian. The integration time of frames in the recording was such that the effective frames per second came out to be 5 FPS. To achieve these integration times, 3×3 spatial binning was performed, resulting in an effective pixel size of $165\,\mu\text{m} \times 165\,\mu\text{m}$ ($25.599 \times 10^{-4}\,\mu\text{m}^{-1}$ in reciprocal space at the target plane).

5.3.2 Object Tracking

Cross Correlation Position Information

In order to compare the raw and TSFQCI recordings against one another, the location of the cross-correlation peak is used to determine where the object is located within the transverse beam profile for both recording cases as outlined in Equation (A.48) The tracking of the object position is shown in Figure 5.9.

Comparing TSFQCI Recording vs Conventional Object Tracking

For the object tracking, the variance in the position of the object in each recording is calculated as the sum of the squares of the deviations from the actual position of the object, as given by the readout of an automatic translation stage. The variance of the position of the observed image dropped from 263.821 μm for the raw recording to 146.043 μm for the TSFQCI recording (Figure 5.9). This corresponds to a drop in variance from 10.55% of the object's actual width for the raw recording to only 5.84% of the object's width for the TSFQCI recording. While this already is a nearly twofold improvement in tacking accuracy, the variance in the TSFQCI recording is possibly being limited by the effective resolution of the camera. This is because a spatial resolution of 165 μm on at the camera, along with the magnification of the setup, means that the minimum possible variance in the measurement for this object speed would be 90.318 μm. Thus, with a better camera resolution, the actual improvement in accuracy of object tracking may be even better than what is seen in the results here.

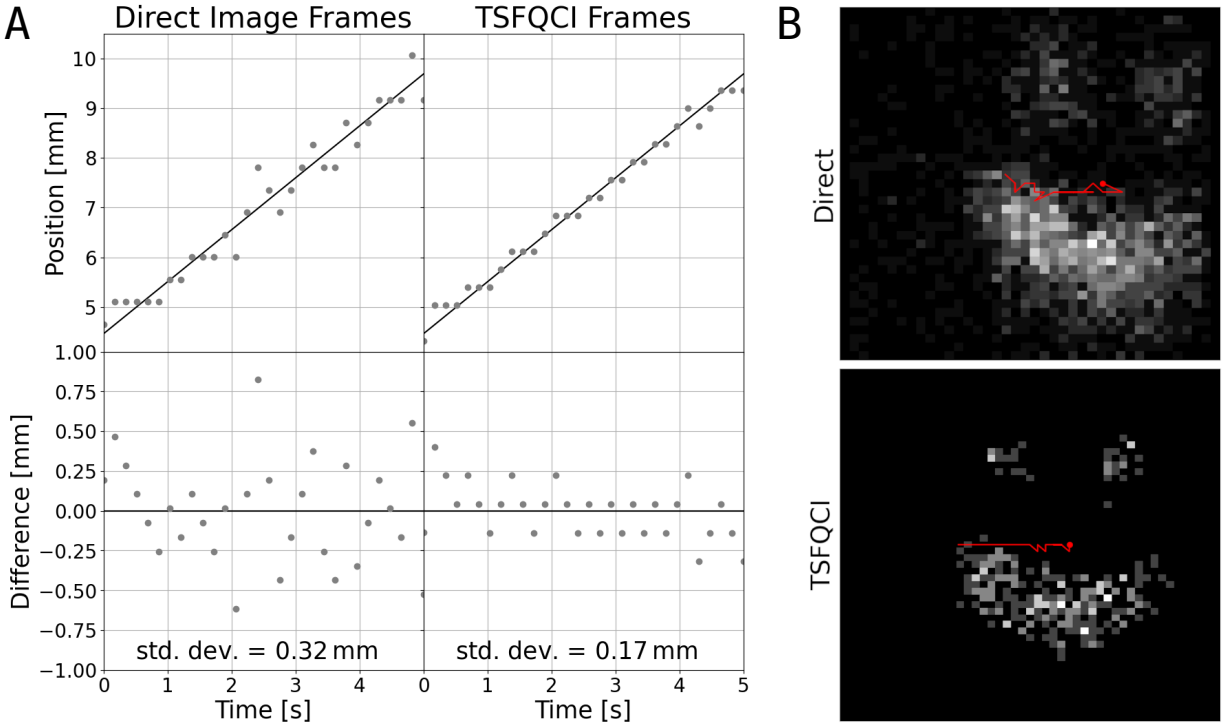

Figure 5.9: **TSFQCI Recording and Object Tracking.** The measured positions of the image in both forms of the recording, as compared to the actual position of the object. See the accompanying video for an example of these real-time recordings. The frame rate for both recordings is 5 FPS. Note that the width of the object is roughly 2.5mm and thus the variances are equivalent to 10.55% and 5.84% of the overall width of the object for the raw and TSFQCI recordings, respectively.

Chapter 6

Discussion

6.1 Improvements to Multiple Quantum Imaging Techniques

Taking advantage of the inherent robustness of GI against turbulent media along with the speed and noise robustness of QI, TSFQCI opens the door to recording optically encoded information through turbulent media with robustness against a noisy background on a sub-second timescale. This brings quantum correlated imaging one step closer to real world applications. These properties combined could establish the baseline for new developments in quantum communication and sensing.

6.1.1 Speed of General Quantum Imaging

The TSFQCI technique demonstrates a clear advantage over direct imaging at the same light level across all tested scenarios. This is true for the 5 second exposures, which are at the speed of contemporary quantum imaging techniques. This further holds true for the 0.5 second exposures, which is faster image acquisition than contemporary quantum imaging techniques. Even further still, the 0.2 second exposures which make up the recording is the first demonstration of a quantum imaging-based recording with such a high frame rate. All of this is a consequence of the superior noise robustness of TSFQCI as compared to other quantum imaging techniques.

Improving the Speed of Quantum Correlated Imaging Techniques

As mentioned in Chapter 1.2.4, quantum correlated imaging techniques generally suffer from slow acquisition time, as a consequence of external noise sources. By modifying quantum correlated imaging techniques to measure both time and space information of each arm, alongside the other degree of freedom, the noise robustness can be significantly improved. This is already shown here, as TSFQCI is equivalent to modifying ghost imaging in this way, where it is evident that the noise robustness improved significantly, by comparing the time filtered results to the TSFQCI results (compare Figure 4.1.C2 to E2).

6.1.2 Accuracy of General Quantum Imaging

The TSFQCI technique also demonstrates a clear advantage over direct imaging when it comes to the robustness against distortions from turbulent media. Even when no noise is added, the TSFQCI images depict an accurate image of the target as opposed to the direct images which show distortions. This is unsurprising as this is the case for traditional ghost imaging as well, however unlike in traditional ghost imaging, when external noise is added to the system the TSFQCI image still is robust against distortions. While benefits from ghost imaging were previously too sensitive to be utilized in any practical sense, the improvements from TSFQCI allow for it to be practically applied.

Improving the Accuracy of Quantum Correlated Imaging Techniques

Quantum correlated imaging techniques have so far been limited to use in controlled laboratory settings. As the technologies prove more and more useful, there is a chance that they will be desired to be applied in outside of lab scenarios. Such scenarios bring with them the issues of imaging through atmosphere, which can notoriously distort the light used in the measurement, and thus the final measurement results. Further, even within the laboratory setting, it is not uncommon for samples which are to be measured to need to be contained within something in order to be measured. In microscopy, for example, samples often cannot be suspended in free-space, and instead are often held between microscope slides. These slides can introduce aberrations which are not trivial to correct for [26]. Similar aberrations can be imagined to be introduced in quantum correlated imaging as the technology matures to the point of practical use.

In both cases outlined above, the distortions will lead to a decrease in accuracy of the quantum correlated imaging as a result of the presence of distortions from turbulent media.

The techniques described here for performing TSFQCI provide a mechanism which already takes advantage of the quantum sources utilized in quantum correlated imaging in order to solve this problem with minimal modification.

Improving the Accuracy of Real World Quantum LiDAR

Quantum LiDAR is a good early example of a quantum correlated imaging technique which is already finding uses outside the controlled lab environment. As such, similar to classical LiDAR, quantum LiDAR can easily suffer in accuracy from the effects of atmospheric distortions of the signal. While the implementation would require some clever engineering, quantum LiDAR could be made robustness against at least some portion of these distortions utilizing techniques from TSFQCI.

6.2 Novel Techniques from TSFQCI

6.2.1 A Novel Object Tracking Technique in Noisy and Turbulent Channels

For the first time ever, quantum imaging techniques were utilized to create a recording for the sake of measuring the real time information of an object, specifically here the location of the object. The object tracking accuracy showed an improvement when using this TSFQCI method, including the qualitative assessment of the actual output recordings (see attached video). The accuracy in tracking the position of the object was much higher in the TSFQCI recording than in the raw recording, and is possibly limited from further improvement by the resolution of the camera. Such a technique may have applications in tracking objects within a noisy or highly turbulent environment. Generally, this shows strong evidence supporting the effective use of quantum sources to measure dynamic processes.

6.2.2 Semi-Classical Encryption with Quantum Sources

Throughout the discussion of applications, it has been assumed that the distortions of the wavefront of the light signal have been unintentionally caused. This does not generally need to be the case, as the distortions can potentially be caused intentionally in order to hide information. Consider the case of somehow spatially encoding information onto the signal photons from SPDC using a transmissive mask (Figure 6.1). This information

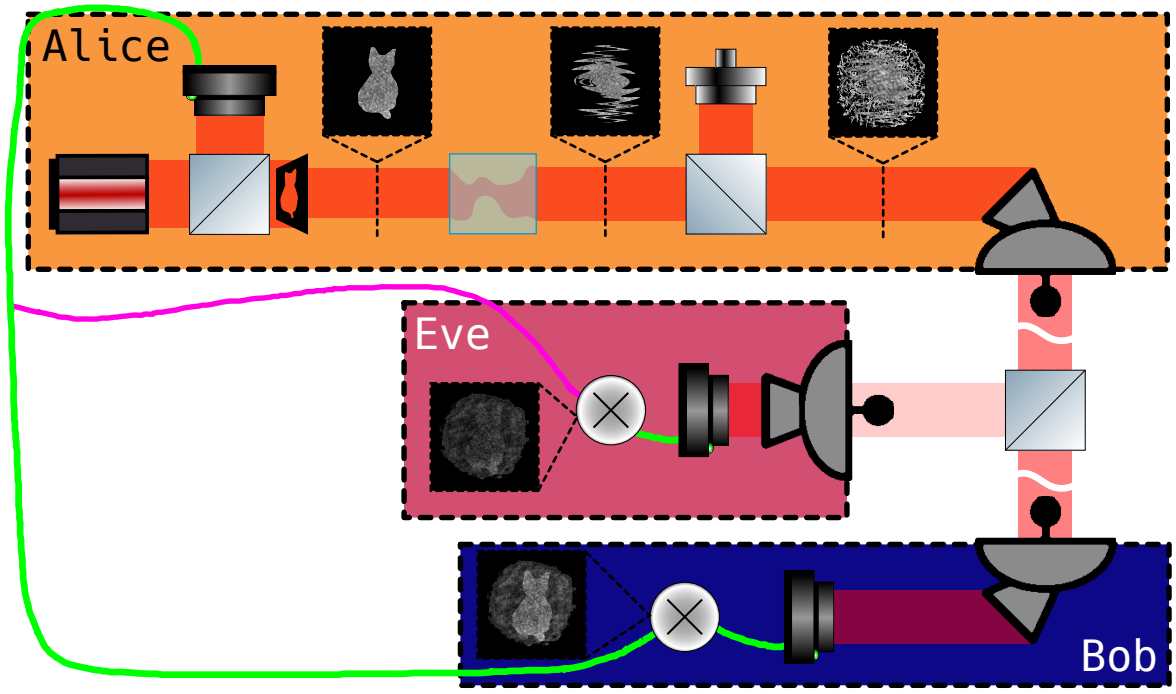

Figure 6.1: **Semi-Classical Encryption.** A schematic example of semi-classical encryption is shown here. The secret information to encode in this case is the image of a silhouette of a cat, which the sender Alice encodes onto the signal photons from an SPDC pair. The secret image is then intentionally distorted by Alice, and mixed with a background signal. Alice also measures the time of arrival and spatial information of all idler photons from the source. Alice sends the encrypted image to the receiver Bob over a free-space channel, and sends the time of arrival and spatial information of the idler source to Bob over a clear channel. Bob receives both sets of information, and uses them to decode the secret message. A third party, Eve, attempts to intercept the message. Eve can tap into the clear channel to gain the idler information, but to intercept the message requires splitting off an irreplaceable percentage of the signal. To preserve Bob's use of the message, the percent must be low, and thus Eve is unable to resolve the secret properly.

could then be intentionally significantly distorted to the point of no longer having any directly recognizable spatial structure, and further could be mixed with some external source, thus encoding the information. The signal and external photons can then be transmitted through free-space channels, in which case at the measurement side they would be measured along with more noise photons. On the sender's side, the time of arrival and position information of the idler photons can be measured, and this information would not directly contain any information about the secret encrypted on the signal. This idler information can be sent over clear channels. The sender would also need to communicate full information about the optical setup on their side, in order for the receiver to know how far from the source the idler information is measured, and also how far the source is from the point of sending. This information could be communicated ahead of time, and even further could simply be standardized. The system information, along with the idler information, is considered with the measured mixed signal-noise photons information from the free-space channel, and allows for the receiver to perform TSFQCI, and thus retrieve the encrypted secret.

Reasonably, the question of how this is resilient to message interception is a fair one. Consider a third party attempting to intercept the message. The third party would need both the signal and idler information in order to retrieve the secret message. The idler information is simple to retrieve since it is communicated via a typical clear channel, however the signal information is not so simple. First, the third party can only intercept a proportion of the signal information. This is because the amount of time it takes for the signal to arrive at the receiver is a key part of how the secret message will be decrypted. Further, since the signal propagates at the speed of light, there is no way for a third party to intercept and then reproduce the signal without creating a time delay, which would render the signal useless to the receiver. Second, even under the assumption that the engineering feat of intercepting only a part of the signal is successful, it is important to acknowledge that the signal is at a very low photon count, especially compared to the added background noise. As such, much of the signal must be split off in order for the third party to retrieve the secret. If much of the signal is split off however, the receiver would not be able to recover the secret. As such, even if a third party is able to overcome the high technical barrier of intercepting part of the signal, the secret message would be rendered indistinguishable.

6.3 Limitations of the Technique

For as beneficial as the TSFQCI technique is, it also has its limitations. Some of them are clear from the prior discussion and interpretation of the results. Others are more subtle and require careful explanation of more technical aspects of the TSFQCI process.

6.3.1 Extreme Scattering

The previous section lays out the upper and lower limits of the TSFQCI algorithm. Most notably for discussion here is that of the upper limit. As mentioned, it is a consequence of the total mixing of spatial information from signal photons with noise photons, resulting in no extra noise benefits. This leads to TSFQCI being equivalent to traditional ghost imaging.

6.3.2 Short Integration Times — Shot Noise

With very short integration times, the signal-to-noise ratios of both the temporal and spatial correlations are very low. This is as a result of shot noise, where the variation in the statistics of differing sources of light are indistinguishable from the variance due to low photon counts. While this has minimal effect on the temporal filtering, due to the smoothing procedure of the $g^{(2)}$ filter, the effect on the spatial filter is significant. This renders the ability for the algorithm to distinguish between real and accidental coincidences minimal when distortions from turbulent media are present. This relates to the discussion of the visibility vs. fidelity around Equation (2.36) as well, making the choice of system and filter parameters in this case difficult. A full theory of TSFQCI would provide a guide to minimize this problem.

6.3.3 High Noise

At very high background noise levels, specifically when the average number of photons per pixel per time window approaches and exceeds $|\alpha|^2 \geq 1$, there begins to be a new problem. In this case, the likelihood for not only a noise photon to show up simultaneously in time with an idler photon, but also in the expected anti-correlated location as an idler photon becomes exceedingly high. This results in at least a 50% probability that an accidental signal-noise pair will be chosen over a real idler-signal pair. Not only does this have the

effect of missing over half of all possible real pairs, but also replaces those values with accidental pairs. This results in a fourfold decrease in the signal-to-background ratio of the resultant image, and such a drop in SBR scales quadratically with the increase in external noise intensity.

6.4 Future Work

Since this work is at the forefront of a new and quickly expanding field, there are many avenues down which future work can be pursued. A handful of ideas are mentioned conceptually and briefly here.

6.4.1 Broadband Quantum Imaging

In Chapter A.1.1, it is mentioned that spectral filtering of the photons from SDPC helps in assuring symmetric optical interaction of both photons from the pair when interacting with the system and detectors. This allows for the high degree of temporal and spatial correlations mentioned in Equations (A.16) and (A.9) to hold true. It is noted however that one of the significant limitations of most quantum imaging techniques is the low flux of the quantum sources. By considering a wider spectral range, quantum imaging could be performed over a broadband range of frequencies. This could potentially modify the temporal and spatial correlations, likely for the worse, however the improvement in photon flux may be enough to counteract these losses. Further, the temporal correlations are already orders of magnitude stronger than is detectable by convenient measurement devices, and as such there is a lot of room for those correlations to weaken. The spatial correlations are not as forgiving, however less spatial resolution may be practical for some applications. For example, quantum correlated phase imaging only utilizes an effective 3×3 pixel resolution in the direction of propagation for measurement [76, 79].

6.4.2 Scattering Characterization

Figure 6.2 depicts the basic concept of a characterization strategy based around TSFQCI. In short, after performing TSFQCI through turbulent media (and GI through turbulent media, though with lesser clarity), both the signal and idler images have the same SBR, yet the signal image is distorted by the turbulent media, while the idler image is not. Since the pairing of the photons between the two images is known, this paring can be used to

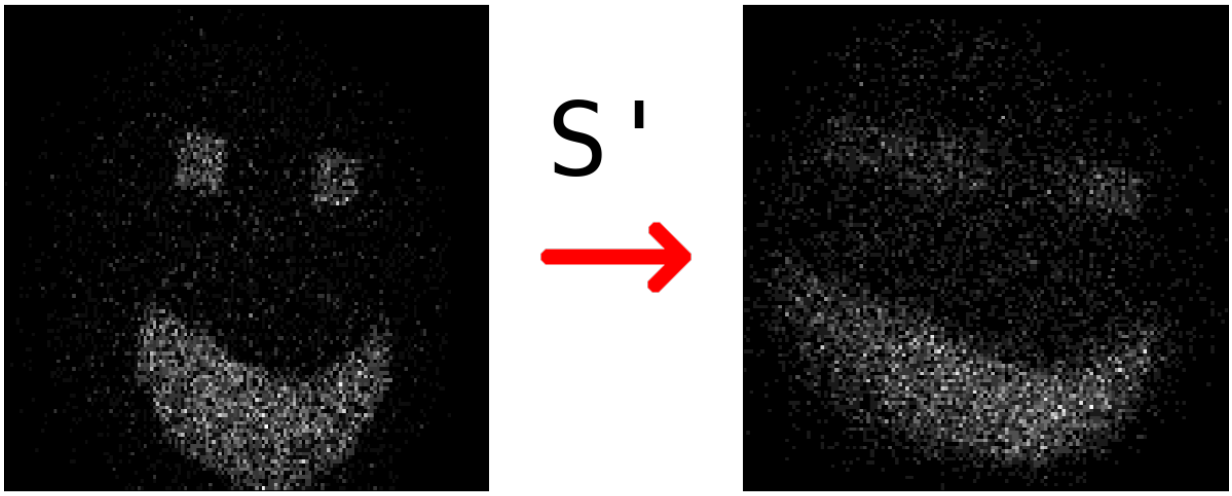

Figure 6.2: **Mapping from Undistorted to Distorted.** Depicted here are the idler (left) and signal (right) images after TSFQCI is performed through turbulent media. The signal image is directly imaged through the turbulent media, and thus is distorted by the media. The idler image never directly interacted with the turbulent media, and thus is undistorted. The proposition is to determine what mapping $\mathbf{S}'$ exists between the left and right images, as this should explain the effect of the turbulent media.

describe the mapping $\mathbf{S}'$ from the undistorted image to the distorted image. This mapping is the same as the mapping which takes the image before propagating through turbulent media to the image after propagating through turbulent media. Thus, the mapping $\mathbf{S}'$ is equivalent to the mapping $\mathbf{S}$ from Equation (2.6), which described the effect of turbulent media. In short, this characterizes the turbulent media in a single-shot measurement.

Unfortunately, there is another consideration which needs to be made. While this describes the effect of the turbulent media in the far field, it does not describe the effect in the near field, or any other optical plane. This is because distortions from turbulent media not only affect the position information of light as it propagates through it, but also the momentum information. This can be summarized as a phase profile being applied to the input light. As a result, in order to characterize this mapping, both position and momentum information must be measured. This is technologically no problem, as there exists measurement devices which can measure both these degrees of freedom simultaneously, like the aforementioned Shack-Hartmann wavefront sensor, or even quantum correlated phase imaging. One consideration is that as an effect of uncertainty, it is not possible to measure both the position and momentum information of a single photon with absolute accuracy. This means that the scattering can only be characterized so well, though in practice this physical limit is well outside the precision of the detectors.

A further consideration which needs to be made is that the phase profile approximation of scattering only holds true for non-volumetric scattering. When volumetric scattering is introduced, a set of possible phase profiles can be applied to the input light as it propagated through the turbulent media. Each phase profile is applied with potentially different probability. This overall effect from turbulent media can be described as a general quantum process. Quantum processes have been showed to be able to be characterized by a technique called quantum process tomography, and in the context of using an entangled photon system, can more specifically be characterized using ancilla-assisted quantum process tomography [3, 4]. The theory to support the functioning of this proposed work could take up a whole chapter on its own, however it is still in the early stages of being developed. As a result, this is a very fruitful avenue to continue work in the realm of quantum imaging, which would push TSFQCI towards a very practical real world application.

References

[1] European Data Relay Satellite System (EDRS) Overview.

[2] Rust Programming Language.

[3] J. B. Altepeter, D. Branning, E. Jeffrey, T. C. Wei, P. G. Kwiat, R. T. Thew, J. L. O'Brien, M. A. Nielsen, and A. G. White. Ancilla-assisted quantum process tomography. *Physical Review Letters*, 90(19):193601, May 2003. arXiv:quant-ph/0303038.

[4] Joseph B. Altepeter, Daniel F.V. James, and Paul G. Kwiat. 4 Qubit Quantum State Tomography. In Matteo Paris and Jaroslav Řeháček, editors, *Quantum State Estimation*, pages 113–145. Springer, Berlin, Heidelberg, 2004.

[5] Yasuhiko Arakawa and Mark J. Holmes. Progress in quantum-dot single photon sources for quantum information technologies: A broad spectrum overview. *Applied Physics Reviews*, 7(2):021309, June 2020.

[6] Reuben S. Aspden, Nathan R. Gemmell, Peter A. Morris, Daniel S. Tasca, Lena Mertens, Michael G. Tanner, Robert A. Kirkwood, Alessandro Ruggeri, Alberto Tosi, Robert W. Boyd, and et al. Photon-sparse microscopy: Visible light imaging using infrared illumination. *Optica*, 2(12):1049, 2015.

[7] Reuben S Aspden, Daniel S Tasca, Robert W Boyd, and Miles J Padgett. Epr-based ghost imaging using a single-photon-sensitive camera. *New Journal of Physics*, 15(7):073032, 2013.

[8] Nicolas Auger, Cyril Nicaud, and Carine Pivoteau. Merge Strategies: from Merge Sort to TimSort. December 2015.

[9] S. Barzanjeh, S. Pirandola, D. Vitali, and J. M. Fink. Microwave quantum illumination using a digital receiver. *Science Advances*, 6(19):eabb0451, May 2020. Publisher: American Association for the Advancement of Science.

[10] Charles H. Bennett and Gilles Brassard. Quantum cryptography: Public key distribution and coin tossing. *Theoretical Computer Science*, 560:7–11, December 2014.

[11] Ryan S. Bennink, Sean J. Bentley, and Robert W. Boyd. "two-photon" coincidence imaging with a classical source. *Physical Review Letters*, 89(11), 2002.

[12] Oliver Bimber and David Schedl. Light-Field Microscopy: A Review. *Journal of Neurology & Neuromedicine*, 4(1):1–6, January 2019.

[13] Frédéric Bouchard, Alicia Sit, Felix Hufnagel, Aazad Abbas, Yingwen Zhang, Khabat Heshami, Robert Fickler, Christoph Marquardt, Gerd Leuchs, Robert w. Boyd, and et al. Quantum cryptography with twisted photons through an outdoor underwater channel. *Optics Express*, 26(17):22563, 2018.

[14] Mohamed Bourennane, Anders Karlsson, and Gunnar Björk. Quantum key distribution using multilevel encoding. *Physical Review A*, 64(1):012306, June 2001. Publisher: American Physical Society.

[15] Robert W. Boyd. 2.12 Advanced Phase Matching Methods. In *Nonlinear optics*. Academic Press is an imprint of Elsevier, San Diego, 4 edition, 2019.

[16] Canada Forestry Branch and Willis Norman Millar. *Methods of Communication Adapted to Forest Protection*. T. Mulvey, printer to the King's Most Excellent Majesty, 1920. Google-Books-ID: CI5OAAAAMAAJ.

[17] Nianwen Cao, Cunxiong Zhu, Yangfeng Kai, and Peng Yan. A method of background noise reduction in lidar data. *Applied Physics B*, 113(1):115–123, October 2013.

[18] Yuan Cao, Yu-Huai Li, Kui-Xing Yang, Yang-Fan Jiang, Shuang-Lin Li, Xiao-Long Hu, Maimaiti Abulizi, Cheng-Long Li, Weijun Zhang, Qi-Chao Sun, Wei-Yue Liu, Xiao Jiang, Sheng-Kai Liao, Ji-Gang Ren, Hao Li, Lixing You, Zhen Wang, Juan Yin, Chao-Yang Lu, Xiang-Bin Wang, Qiang Zhang, Cheng-Zhi Peng, and Jian-Wei Pan. Long-Distance Free-Space Measurement-Device-Independent Quantum Key Distribution. *Physical Review Letters*, 125(26):260503, December 2020. Publisher: American Physical Society.

[19] Kam Wai Chan, D. S. Simon, A. V. Sergienko, Nicholas D. Hardy, Jeffrey H. Shapiro, P. Ben Dixon, Gregory A. Howland, John C. Howell, Joseph H. Eberly, Malcolm N. O'Sullivan, and et al. Theoretical analysis of quantum ghost imaging through turbulence. *Physical Review A*, 84(4), 2011.

[20] Jing Cheng. Ghost imaging through turbulent atmosphere. *Optics Express*, 17(10):7916, 2009.

[21] Archibald Constable. Telegraph. In *Encycopædia Britannica*, volume 10, pages 645–651. 6 edition, 1824. Google-Books-ID: MsYnAAAAMAAJ.

[22] Christophe Couteau. Spontaneous parametric down-conversion. *Contemporary Physics*, 59(3):291–304, July 2018. arXiv:1809.00127 [physics, physics:quant-ph].

[23] Hugo Defienne and Sylvain Gigan. Spatially entangled photon-pair generation using a partial spatially coherent pump beam. *Physical Review A*, 99(5), 2019.

[24] P. Ben Dixon, Gregory A. Howland, Kam Wai Chan, Colin O'Sullivan-Hale, Brandon Rodenburg, Nicholas D. Hardy, Jeffrey H. Shapiro, D. S. Simon, A. V. Sergienko, R. W. Boyd, and et al. Quantum ghost imaging through turbulence. *Physical Review A*, 83(5), 2011.

[25] Damian H. Evans, Roland J. Fletcher, Christophe Pottier, Jean-Baptiste Chevance, Dominique Soutif, Boun Suy Tan, Sokrithy Im, Darith Ea, Tina Tin, Samnang Kim, Christopher Cromarty, Stéphane De Greef, Kasper Hanus, Pierre Bâty, Robert Kuszinger, Ichita Shimoda, and Glenn Boornazian. Uncovering archaeological landscapes at Angkor using lidar. *Proceedings of the National Academy of Sciences of the United States of America*, 110(31):12595–12600, July 2013.

[26] Yilun Fan and Andrew P. Bradley. A two-stage method to correct aberrations induced by slide slant in bright-field microscopy. *Micron*, 87:18–32, August 2016.

[27] Nicholas Ferrante, Jérôme Gilles, and Shibin Parameswaran. Investigation of moving objects through atmospheric turbulence from a non-stationary platform. *Applications of Digital Image Processing XLII*, 11137:111370X, September 2019. Conference Name: Applications of Digital Image Processing XLII ADS Bibcode: 2019SPIE11137E..0XF.

[28] F. Ferri, D. Magatti, A. Gatti, M. Bache, E. Brambilla, and L. A. Lugiato. High-resolution ghost image and ghost diffraction experiments with thermal light. *Physical Review Letters*, 94(18), 2005.

[29] Kent A. Fredriksson and Hans M. Hertz. Evaluation of the DIAL technique for studies on NO_2 using a mobile lidar system. *Applied Optics*, 23(9):1403–1411, May 1984. Publisher: Optica Publishing Group.

[30] Nahum Gat. Imaging spectroscopy using tunable filters: a review. In *Wavelet Applications VII*, volume 4056, pages 50–64. SPIE, April 2000.

[31] Marco Genovese. Real applications of quantum imaging. *Journal of Optics*, 18(7):073002, 2016.

[32] Christopher Gerry and Peter Knight. 9.1 Photon sources: spontaneous parametric down-conversion. In *Introductory Quantum Optics*, pages 214–217. 1 edition, 2004.

[33] Valerio Flavio Gili, Dupish Dupish, Andres Vega, Massimo Gandola, Enrico Manuzzato, Matteo Perenzoni, Leonardo Gasparini, Thomas Pertsch, and Frank Setzpfandt. Quantum ghost imaging based on a "looking back" 2d spad array. *Applied Optics*, 62(12):3093, 2023.

[34] Robert O Green, Michael L Eastwood, Charles M Sarture, Thomas G Chrien, Mikael Aronsson, Bruce J Chippendale, Jessica A Faust, Betina E Pavri, Christopher J Chovit, Manuel Solis, Martin R Olah, and Orlesa Williams. Imaging Spectroscopy and the Airborne Visible/Infrared Imaging Spectrometer (AVIRIS). *Remote Sensing of Environment*, 65(3):227–248, September 1998.

[35] T. Gregory, P.-A. Moreau, E. Toninelli, and M. J. Padgett. Imaging through noise with quantum illumination. *Science Advances*, 6(6), 2020.

[36] R.J. Hill, R.A. Bohlander, S.F. Clifford, R.W. McMillan, J.T. Priestly, and W.P. Schoenfeld. Turbulence-induced millimeter-wave scintillation compared with micrometeorological measurements. *IEEE Transactions on Geoscience and Remote Sensing*, 26(3):330–342, May 1988. Conference Name: IEEE Transactions on Geoscience and Remote Sensing.

[37] Hazel Hodgson, Yingwen Zhang, Duncan England, and Benjamin Sussman. Reconfigurable phase contrast microscopy with correlated photon pairs. *Applied Physics Letters*, 122(3):034001, January 2023.

[38] Disen Hu and Nantheera Anantrasirichai. Object recognition in atmospheric turbulence scenes, May 2023. arXiv:2210.14318 [cs].

[39] Haroon Idrees, Khurram Soomro, and Mubarak Shah. Detecting Humans in Dense Crowds Using Locally-Consistent Scale Prior and Global Occlusion Reasoning. *IEEE Transactions on Pattern Analysis and Machine Intelligence*, 37(10):1986–1998, October 2015. Conference Name: IEEE Transactions on Pattern Analysis and Machine Intelligence.

[40] M. V. Jabir and G. K. Samanta. Robust, high brightness, degenerate entangled photon source at room temperature. *Scientific Reports*, 7(1):12613, October 2017. Publisher: Nature Publishing Group.

[41] Kyle Jordan, Andrew Proppe, Jeff Lundeen, and Benjamin Sussman. Quantum-Enhanced Absorption and Phase Metrology Using Two-Photon Interference. page JTu5A.51. Optica Publishing Group, October 2023.

[42] Hugo Larocque, Alessio D'Errico, Manuel F. Ferrer-Garcia, Avishy Carmi, Eliahu Cohen, and Ebrahim Karimi. Optical framed knots as information carriers. *Nature Communications*, 11(1):5119, October 2020. Publisher: Nature Publishing Group.

[43] Martin P. Lavery, Christian Peuntinger, Kevin Günthner, Peter Banzer, Dominique Elser, Robert W. Boyd, Miles J. Padgett, Christoph Marquardt, and Gerd Leuchs. Free-space propagation of high-dimensional structured optical fields in an urban environment. *Science Advances*, 3(10), 2017.

[44] Zheng-Ping Li, Xin Huang, Peng-Yu Jiang, Yu Hong, Chao Yu, Yuan Cao, Jun Zhang, Feihu Xu, and and Jian-Wei Pan. Super-resolution single-photon imaging at 8.2 kilometers. *Optics Express*, 28(3):4076–4087, February 2020. Publisher: Optica Publishing Group.

[45] Sheng-Kai Liao, Hai-Lin Yong, Chang Liu, Guo-Liang Shentu, Dong-Dong Li, Jin Lin, Hui Dai, Shuang-Qiang Zhao, Bo Li, Jian-Yu Guan, Wei Chen, Yun-Hong Gong, Yang Li, Ze-Hong Lin, Ge-Sheng Pan, Jason S. Pelc, M. M. Fejer, Wen-Zhuo Zhang, Wei-Yue Liu, Juan Yin, Ji-Gang Ren, Xiang-Bin Wang, Qiang Zhang, Cheng-Zhi Peng, and Jian-Wei Pan. Long-distance free-space quantum key distribution in daylight towards inter-satellite communication. *Nature Photonics*, 11(8):509–513, August 2017. Publisher: Nature Publishing Group.

[46] Seth Lloyd. Enhanced sensitivity of photodetection via quantum illumination. *Science*, 321(5895):1463–1465, 2008.

[47] E. D. Lopaeva, I. Ruo Berchera, I. P. Degiovanni, S. Olivares, G. Brida, and M. Genovese. Experimental realization of quantum illumination. *Physical Review Letters*, 110(15), 2013.

[48] Thobois Ludovic P., Raghavendra Krishnamurthy, Sophie Loaec, Jean Pierre Cariou, Agnès Dolfi-Bouteyre, and Mathieu Valla. Wind and EDR Measurements with Scanning Doppler LIDARs for Preparing Future Weather Dependent Separation Concepts (Invited), June 2015.

[49] M. Piccardi. Background subtraction techniques: a review, 2004.

[50] Aurora Maccarone, Kristofer Drummond, Aongus McCarthy, Ulrich K. Steinlehner, Julian Tachella, Diego Aguirre Garcia, Agata Pawlikowska, Robert A. Lamb, Robert K. Henderson, Stephen McLaughlin, Yoann Altmann, and Gerald S. Buller. Submerged single-photon LiDAR imaging sensor used for real-time 3D scene reconstruction in scattering underwater environments. *Optics Express*, 31(10):16690–16708, May 2023. Publisher: Optica Publishing Group.

[51] A. Meda, A. Caprile, A. Avella, I. Ruo Berchera, I. P. Degiovanni, A. Magni, and M. Genovese. Magneto-optical imaging technique for hostile environments: The ghost imaging approach. *Applied Physics Letters*, 106(26), 2015.

[52] Meriwether Lewis and William Clark. July 20, 1805 | Journals of the Lewis and Clark Expedition, July 1805.

[53] Ronald E. Meyers, Keith S. Deacon, and Yanhua Shih. Turbulence-free ghost imaging. *Applied Physics Letters*, 98(11):111115, March 2011.

[54] Janusz Mikolajczyk, Zbigniew Bielecki, Maciej Bugajski, Jozef Piotrowski, Jacek Wojtas, Waldemar Gawron, Dariusz Szabra, and Artur Prokopiuk. Analysis of Free-Space Optics Development. *Metrology and Measurement Systems*, 24, December 2017.

[55] Paul-Antoine Moreau, Ermes Toninelli, Thomas Gregory, and Miles J. Padgett. Ghost imaging using optical correlations. *Laser & Photonics Reviews*, 12(1), 2017.

[56] Peter A. Morris, Reuben S. Aspden, Jessica E. Bell, Robert W. Boyd, and Miles J. Padgett. Imaging with a small number of photons. *Nature Communications*, 6(1), 2015.

[57] Andrei Nomerotski. Imaging and time stamping of photons with nanosecond resolution in timepix based optical cameras. *Nuclear Instruments and Methods in Physics Research Section A: Accelerators, Spectrometers, Detectors and Associated Equipment*, 937:26–30, 2019.

[58] T. B. Pittman, Y. H. Shih, D. V. Strekalov, and A. V. Sergienko. Optical imaging by means of two-photon quantum entanglement. *Physical Review A*, 52(5), 1995.

[59] Meghavi Rana and Megha Bhushan. Machine learning and deep learning approach for medical image analysis: diagnosis to detection. *Multimedia Tools and Applications*, pages 1–39, December 2022.

[60] Rayleigh. The Problem of the Random Walk. *Nature*, 72(1866):318–318, August 1905. Publisher: Nature Publishing Group.

[61] Jennifer C. Ricklin and Frederic M. Davidson. Atmospheric turbulence effects on a partially coherent Gaussian beam: implications for free-space laser communication. *JOSA A*, 19(9):1794–1802, September 2002. Publisher: Optica Publishing Group.

[62] Bahaa Saleh and Malvin Teich. 22.4 Second-Order Nonlinear Optics: Coupled Waves. In *Fundamentals of Photonics, 3rd Edition*. February 2019.

[63] Henry Serruys. Towers in the Northern Frontier Defenses of the Ming. *Ming Studies*, 1982(1):9–76, January 1982. Publisher: Routledge _eprint: https://doi.org/10.1179/014703782788764701.

[64] Alicia Sit, Frédéric Bouchard, Robert Fickler, Jérémie Gagnon-Bischoff, Hugo Larocque, Khabat Heshami, Dominique Elser, Christian Peuntinger, Kevin Günthner, Bettina Heim, and et al. High-dimensional intracity quantum cryptography with structured photons. *Optica*, 4(9):1006, 2017.

[65] Si-Hui Tan, Baris I. Erkmen, Vittorio Giovannetti, Saikat Guha, Seth Lloyd, Lorenzo Maccone, Stefano Pirandola, and Jeffrey H. Shapiro. Quantum illumination with gaussian states. *Physical Review Letters*, 101(25), 2008.

[66] Larry N. Thibos, Raymond A. Applegate, James T. Schwiegerling, and Robert Webb. Standards for Reporting the Optical Aberrations of Eyes. *Journal of Refractive Surgery*, 18(5):S652–S660, September 2002. Publisher: SLACK Incorporated.

[67] Rachael Tobin, Abderrahim Halimi, Aongus McCarthy, Martin Laurenzis, Frank Christnacher, and Gerald S. Buller. Three-dimensional single-photon imaging through obscurants. *Optics Express*, 27(4):4590–4611, February 2019. Publisher: Optica Publishing Group.

[68] Ricardo Gallego Torrome and Shabir Barzanjeh. Advances in Quantum Radar and Quantum LiDAR. *Progress in Quantum Electronics*, page 100497, December 2023. arXiv:2310.07198 [quant-ph].

[69] A. Trifonov and A. Zavriyev. Secure communication with a heralded single-photon source. *Journal of Optics B: Quantum and Semiclassical Optics*, 7(12):S772, November 2005.

[70] Victor Vidyapin, Yingwen Zhang, Duncan England, and Benjamin Sussman. Characterisation of a single photon event camera for quantum imaging. *Scientific Reports*, 13(1), 2023.

[71] Pauli Virtanen, Ralf Gommers, Travis E. Oliphant, Matt Haberland, Tyler Reddy, David Cournapeau, Evgeni Burovski, Pearu Peterson, Warren Weckesser, Jonathan Bright, Stéfan J. van der Walt, Matthew Brett, Joshua Wilson, K. Jarrod Millman, Nikolay Mayorov, Andrew R. J. Nelson, Eric Jones, Robert Kern, Eric Larson, C J Carey, İlhan Polat, Yu Feng, Eric W. Moore, Jake VanderPlas, Denis Laxalde, Josef Perktold, Robert Cimrman, Ian Henriksen, E. A. Quintero, Charles R. Harris, Anne M. Archibald, Antônio H. Ribeiro, Fabian Pedregosa, Paul van Mulbregt, and SciPy 1.0 Contributors. SciPy 1.0: Fundamental Algorithms for Scientific Computing in Python. *Nature Methods*, 17:261–272, 2020.

[72] Patrick Vrancken, Gerhard Ehret, Hervé Barny, Henk Veerman, and Laurent Lombard. Aeronautics Lidar Applications - Airborne LIDAR Detection of Clear Air Turbulence (CAT) within the FP7 DELICAT project. October 2014.

[73] Z. Wang, J. Zhou, H. Hu, and Z. Gong. Evaluation of dual differential absorption lidar based on Raman-shifted Nd:YAG or KrF laser for tropospheric ozone measurements. *Applied Physics B Lasers and Optics*, 62(2):143–147, February 1996.

[74] F. N. C. Wong, J. H. Shapiro, and T. Kim. Efficient generation of polarization-entangled photons in a nonlinear crystal. *Laser Physics*, 16(11):1517–1524, November 2006.

[75] Kai Xiao, Logan Engstrom, Andrew Ilyas, and Aleksander Madry. *Noise or Signal: The Role of Image Backgrounds in Object Recognition.* June 2020.

[76] Yingwen Zhang, Duncan England, Antony Orth, Ebrahim Karimi, and Benjamin Sussman. Quantum light-field microscopy for volumetric imaging with extreme depth of field. *Phys. Rev. Appl.*, 21:024029, Feb 2024.

[77] Yingwen Zhang, Duncan England, and Benjamin Sussman. Snapshot hyperspectral imaging with quantum correlated photons. *Optics Express*, 31(2):2282, 2023.

[78] Yingwen Zhang, Paul-Antoine Moreau, Duncan England, Ebrahim Karimi, and Benjamin Sussman. Background resilient quantitative phase microscopy using entangled photons, June 2024. arXiv:2406.06377 [physics, physics:quant-ph].

[79] Yingwen Zhang, Antony Orth, Duncan England, and Benjamin Sussman. Ray tracing with quantum correlated photons to image a three-dimensional scene. *Physical Review A*, 105(1), 2022.

[80] Yingwen Zhang, Alicia Sit, Frédéric Bouchard, Hugo Larocque, Florence Grenapin, Eliahu Cohen, Avshalom C. Elitzur, James L. Harden, Robert W. Boyd, and Ebrahim Karimi. Interaction-free ghost-imaging of structured objects. *Optics Express*, 27(3):2212, 2019.

APPENDICES

A.1 SPDC as It Relates to Quantum Imaging

The process by which one pump photon is converted into a signal and idler photon is certainly an interesting subject in and of itself, however in the context of quantum imaging the total details are not so important. Briefly, SDPC is made possible via a pump electromagnetic field undergoing a nonlinear optical process in a medium with a $\chi^{(2)}$ nonlinearity (e.g. a crystal with a non-centrosymmetric crystal structure like potassium titanyl phosphate (KTP) crystals, or barium borate (BBO) crystals), resulting in the spontaneous production of a biphoton state made up of a signal and idler photon entangled with one another. Of principal interest to quantum imaging are the correlations between these signal and idler photons as they relate to the pump field.

The energy and position correlations were conceptually introduced previously, but will be investigated in more detail here. Specifically, it is common to discuss these correlations under the assumption of a perfect pump and perfect nonlinear medium. In reality, the pump is typically a real coherent beam with a Gaussian profile and the nonlinear medium is a nonlinear crystal with finite size. These details are important when it comes to properly creating the system design and filters necessary for TSFQCI to function. Most of the ideal theory here comes from the following sources: [15, 22, 62, 74], which are all rich references for overviews on the classical and quantum descriptions of SPDC.

It is worth noting that the version of SPDC in mind here is that of type-II, though most of the theory, aside from some of the phase matching details, applies to SPDC of type-0 and type-I as well.

A.1.1 Energy Correlation

As mentioned previously, the energy correlation of SPDC leads to a degeneracy in the signal and idler energies, and is important for assuring symmetric optical interaction and filtering efficiency of the two photons. One unmentioned importance, however, is that the energy and momentum of a photon are not independent properties. In fact, since the speed of light in a media is a wavelength dependent property, the momenta anti-correlation necessary for quantum imaging to function will need to consider the wavelength of the photons as well. This introduces two new degrees of freedom which need to be considered, and increases the state space of the problem significantly by adding two new dimensions to it. Such a state space would be too complex to sufficiently filter, and as such nearly perfect degeneracy of the SPDC photons' energies must be assured.

Ideal

The energy correlation of the photons was depicted visually in Figure 1.1.C, and this depiction will be described with mathematical rigor here. Variables subscripted with i and s will indicate whether the variable refers to either the idler or signal fields, respectively. Likewise, variables subscripted with p will indicate that the variable refers to the pump field. Using this convention, the energy of the signal and idler fields are related to the energy of the pump field as

$$\hbar\omega_p = \hbar\omega_s + \hbar\omega_i \tag{A.1}$$

where ω is the angular frequency of the respective field. Since SPDC is an isolated process where a single pump photon is annihilated resulting in the signal and idler photons being created, this relation is absolute because of energy conservation. In the case of degenerate SPDC this is often simplified to

$$\omega_s = \omega_i = \frac{\omega_p}{2}. \tag{A.2}$$

While Equation (A.1) is exact, Equation (A.2) is not necessarily. Instead, there is some uncertainty in the degeneracy which results in

$$\omega_s = \frac{\omega_p}{2} \pm \delta\omega \quad \text{and} \quad \omega_i = \frac{\omega_p}{2} \mp \delta\omega \tag{A.3}$$

where $\delta\omega$ is the uncertainty.

With a Coherent Guassian Pump

The previous discussion assumes that there is an exact frequency of the pump photon, however when considering a real source for the pump this is generally not true. Instead, real single frequency sources have a linewidth. In this case, the linewidth can be indicated by an uncertainty in the pump frequency, resulting in the frequencies of the signal and idler fields becoming

$$\omega_s = \frac{\omega_p \pm \delta\omega_p}{2} \pm \delta\omega \quad \text{and} \quad \omega_i = \frac{\omega_p \pm \delta\omega_p}{2} \mp \delta\omega. \tag{A.4}$$

The result of these two considerations is that the total variance between the frequencies of the signal and idler fields becomes

$$\delta\left(|\omega_s - \omega_i|\right) = \delta\omega + \frac{\delta\omega_p}{2}. \tag{A.5}$$

After Filtering

In order to assure the energy degeneracy of the photons, spectral filtering is necessary. A spectral filter will set an alternative limit to the variance between the frequencies of the signal and idler fields described in Equation (A.5), resulting in

$$\delta\left(|\omega_s - \omega_i|\right) = \min\left[\delta\omega + \frac{\delta\omega_p}{2},\ \delta_{\text{filter}}\right] \tag{A.6}$$

where δ_{filter} is the width of the filter. In order to prevent the issues from the non-degeneracy of the signal and pump energies, $\delta\left(|\omega_s - \omega_i|\right)$ must be small enough that the difference between the final displacement of the signal and idler photons at the measurement plane is less than the spatial and temporal resolution of the measurement device. If this is guaranteed, then the perfect energy degeneracy described in Equation (A.2) can be considered to be sufficiently true.

A.1.2 Spatial Correlation

Unlike the energy correlation, the spatial correlations between the signal and idler photons is crucial to the function of quantum imaging. Without spatial correlations between the photons, there would be no way to perform quantum imaging of the system. A weakening of the correlations still allows quantum imaging, but the resolution of the resultant image

will worsen proportionally. As such, understanding the actual correlation strength at the image plane is important in determining the possible final resolution of the system, which further affects the design of the TSFQCI filters.

Ideal

The spatial correlations of the photons are depicted visually in Figure 1.1.A and 1.1.B. The two correlations, in the location of generation of the pair, and in the momentum of the photons in the pair, have different effects on the final system. First considering the location of generation correlation, if the generation of the pair to is considered to occur at time $t = 0$, then

$$\vec{x_s}(0) = \vec{x_i}(0) = \vec{x}(0) \tag{A.7}$$

where $\vec{x_{\{s,i\}}}(t)$ denotes the (x, y, z) position at time t of the signal and idler photons, respectively, and $\vec{x}(0)$ is a convenient label to more directly discuss this actual position in space. As a result, the optical path length traveled by both of the photons in the same amount of time is identical and given as

$$\Lambda_{\{s,i\}} = \int_0^t \|\vec{x_s}(\tau)\| \, d\tau = \int_0^t \|\vec{x_i}(\tau)\| \, d\tau. \tag{A.8}$$

If there is an optical path length difference between the two photons upon arrival at the measurement devices, then the expected dToA of the two photons can be directly calculated as

$$\text{dToA} = \frac{|\Lambda_s - \Lambda_i|}{c} \tag{A.9}$$

where c is the speed of light in vacuum.

The other spatial correlation, which is the key component that allows for quantum imaging with SPDC, is that of momentum correlation. More specifically, it is a momentum *anti*-correlation which occurs at generation of the photon pair. This anti-correlation is a consequence of the phase matching conditions required for SPDC to occur. Assuming perfect phase matching, the momentum anti-correlation can be represented as

$$\hbar\hat{k_s} + \hbar\hat{k_i} = \hbar\hat{k_p} \tag{A.10}$$

where the $\hat{k}$ is the normalized direction of the momentum, also referred to as the wavevector. Typically, the $\hbar$ factors are left out, and further the wavevector of the pump photon is often

assumed to be orthogonal to the measurement plane. Thus, only the transverse components of the signal and idler wavevectors are considered such that the correlation becomes

$$k_{s,x} + k_{i,x} = 0 \quad \text{and} \quad k_{s,y} + k_{i,y} = 0. \tag{A.11}$$

Assuming that $\vec{k_T} = (k_x, k_y)$, this can be simplified to

$$\vec{k_{Ts}} + \vec{k_{Ti}} = \vec{0} \tag{A.12}$$

where $\vec{0} = (0, 0) \in \mathbb{R}^2$.

With a Coherent Gaussian Pump

The previous discussion makes the assumption that the pump photon is a plane wave which is always propagating orthogonal to the measurement plane, and also along the non-linear susceptibility axis of the medium. In reality, the pump photon will be coming from a coherent Gaussian beam, and thus there will be some variation in the direction of the pump photons' propagations. This variation is partially in the transverse component of the pump photons' wavevectors, and so this modifies Equation (A.12) to become

$$\|\vec{k_{Ts}} + \vec{k_{Ti}}\| = \delta_p(\|\vec{k_{Ts}} + \vec{k_{Ti}}\|) \tag{A.13}$$

where $\delta_p(\|\vec{k_{Ts}} + \vec{k_{Ti}}\|)$ is related to the transverse component of the pump variation. This transverse component has been show to be equivalent to

$$\delta_p(\|\vec{k_{Ts}} + \vec{k_{Ti}}\|) = \sqrt{\frac{1}{\ell_c^2} + \frac{1}{4w^2}} \tag{A.14}$$

where ℓ_c^2 is the coherence length of the pump and w is the beam waist of the pump [23].

With a Finite Sized Crystal

The use of a finite sized crystal as the nonlinear medium also affects both of the spatial correlations mentioned here. While the difference in location of generation of the individual photons in the pair is not changed by a finite-size crystal, the location where the pair is produce within the crystal is no longer fixed to one spot as previously assumed. While Equation (A.7) still holds true, position $\vec{x}(0)$ is varied such that it could occur anywhere within the nonlinear crystal. This results in some added variance in the expected dToA:

$\delta(\text{dToA}) \propto L/c$, where L is the length of the nonlinear crystal. Typically, the crystal length is on the scale of 10^{-3} m, and as such $\delta(\text{dToA}) \propto 10^{-12}$ s, which is orders of magnitude less than the precision of typical ToA measurements for quantum imaging. As such, this effect is negligible in the context of the location of generation correlation.

For the momentum anti-correlation however, this effect is non-negligible. The momentum anti-correlation of the transverse components of the signal and idler photons described in Equation (A.14) is not effected at the plane of creation of the photon pair, however since the plane of the photon creation varies, while the position of the measurement plane does not, this will have an effect at the point of measurement. This can be understood by considering the angular spread of the photons when they are generated. Typically, for type-II SPDC in a periodically poled KTP (ppKTP) crystal, the angle of the photons from the optical axis is dependent on the temperature of the crystal [40]. This dependency is non-trivial, and related to phase matching in a periodically poled crystal, and so for the sake of this discussion will simply be represented as $\theta_{\text{OA}}(T)$. Photon pairs which are produced at opposite ends of the crystal will both have the same angular spread, but since the photons in the pair produced at the leading edge of the crystal will be diverging from the optical axis at a rate of $c \sin \theta_{\text{OA}}(T)$, this will result in the maximum of the uncertainty in the measured photon pair momenta difference being

$$\delta_c(\|\vec{k_{Ts}} + \vec{k_{Ti}}\|) = Lc \sin \theta_{\text{OA}}(T). \tag{A.15}$$

Thus, at the measurement plane, the variance in the anti-correlation of the momenta between signal and idler photons can be taken as

$$\begin{aligned} \delta k &= \delta_p(\|\vec{k_{Ts}} + \vec{k_{Ti}}\|) + \delta_c(\|\vec{k_{Ts}} + \vec{k_{Ti}}\|) \\ &= \sqrt{\frac{1}{\ell_c^2} + \frac{1}{4w^2}} + Lc \sin \theta_{\text{OA}}(T) \end{aligned} \tag{A.16}$$

which it is worth noting is a positive scalar quantity.

With the proper choice of pump, crystal, and temperature, δk can typically be constrained to be on the scale of 10^{-3} m or less at the imaging plane. This scale determines the lower bound for the spatial resolution of a quantum imaging setup.

A.1.3 Other Theoretical Considerations

A few more details are important regarding SPDC as it will be utilized in this quantum imaging setup. As alluded to in the previous section, type-II SPDC is the type of SPDC

which is considered for this setup. In type-II SPDC, assuming a pump photon with a linear polarization $|H\rangle_p$, the biphoton state produced will be

$$|\Phi\rangle = \frac{|H\rangle_i \otimes |V\rangle_s + |V\rangle_i \otimes |H\rangle_s}{\sqrt{2}} \tag{A.17}$$

where $|\cdot\rangle_{i,s}$ represents the polarization state of the idler and signal photons, respectively. Note that $|A\rangle_i \otimes |B\rangle_s$ may be used interchangeably with $|A, B\rangle$ for any properties A and B that are entangled in the biphoton pair state.

Another alluded to detail is that the crystal used will be a periodically poled crystal. This has an effect on the phase matching outlined in Equation (A.10). Namely, it results in the addition of a term relating to the poling period of the crystal on the left-hand side of the phase matching equation. This term is temperature dependent, and is typically denoted as $\Lambda(T)$ (not to be confused with the optical path length $\Lambda_{\{s,i\}}$ from Equations (A.9) and (A.9)). This temperature dependency of $\Lambda(T)$ is what gives rise to the temperature dependence of $\theta_{\text{OA}}(T)$, but otherwise does not affect the final correlations.

The last detail to mention is that, especially when the intensity of the pump is high, SDPC is not limited to producing only single pairs of photons at one time. Generally, the quantum state output from SPDC can be described by a two mode squeezed vacuum state, which in the photon-number basis is represented as

$$|S(r,\phi)\rangle = \frac{1}{\cosh r} \sum_{n=0}^{\infty} \left(-e^{-i\phi} \tanh r\right)^n |n_i, n_s\rangle \tag{A.18}$$

where r is the strength of the squeezing and ϕ the phase of the squeezing. For SPDC $r \propto \chi^{(2)} E_p L$ and ϕ is just the phase of the pump field [22]. Thus, the probability of generating any SPDC light from each pump photon is

$$\sum_{n=1}^{\infty} |S(r,\phi)\rangle\langle n,n| = \frac{1}{\cosh^2 r} \sum_{n=1}^{\infty} \tanh^{2n} r = \tanh^2 r \approx r^2 \quad \text{s.t. } r \ll 1 \tag{A.19}$$

and thus is $\propto \left(\chi^{(2)} E_p L\right)^2$. Similarly, the probability of generating multiple pairs is

$$\sum_{n=2}^{\infty} |S(r,\phi)\rangle\langle n,n| = \frac{1}{\cosh^2 r} \sum_{n=2}^{\infty} \tanh^{2n} r = \tanh^4 r \approx r^4 \quad \text{s.t. } r \ll 1 \tag{A.20}$$

and thus is $\propto \left(\chi^{(2)} E_p L\right)^4$. The chance of generating the states $|2,2\rangle$, $|3,3\rangle$, ... is not very likely with a weak pump, however the ratio of multiple pair states to single pair states is

$$\frac{|S(r,\phi)\rangle\langle 1,1|}{\sum_{n=2}^{\infty} |S(r,\phi)\rangle\langle n,n|} = \frac{\tanh^2 r}{\cosh^2 r} \approx r^4 \quad \text{s.t. } r \ll 1 \tag{A.21}$$

and again $\propto \left(\chi^{(2)} E_p L\right)^2$. It is worth noting that in the case where there is higher-order pair generation, that these states will not follow the spatial correlations outlined here. The probability of generating a single pair as compared to no pairs or multiple pairs is

$$|S(r,\phi)\rangle\langle 1,1| = \frac{\tanh^2 r}{\cosh^2 r} \approx r^2 \quad \text{s.t. } r \ll 1 \tag{A.22}$$

and thus is $\propto \left(\chi^{(2)} E_p L\right)^2$.

It is also useful to consider that, upon the detection of for instance the idler photon, the state of the signal photon then becomes

$$\mathrm{Tr}_i[|S(r,\phi)\rangle\langle S(r,\phi)|] = \frac{1}{\cosh^2 r} \sum_{n=0}^{\infty} \tanh r^{2n} \, |n\rangle\langle n| \tag{A.23}$$

which is a mixed thermal state. The same is true when considering the state of the idler photon predicated on the detection of the signal photon. In isolation however, looking at only the idler (or signal) output port results in a mixture of Fock states as

$$|i\rangle = |s\rangle = \frac{1}{\cosh r} \sum_{n=0}^{\infty} \left(-e^{-i\phi} \tanh r\right)^n |n\rangle \tag{A.24}$$

which again is similarly unlikely to be found with the states $|2\rangle$, $|3\rangle$, ...

A.2 Distortions from Turbulent Media and Noise as They Relate to Quantum Imaging

A.2.1 Distortions from Turbulent Media

Many different distortions can arise from light propagating through turbulent media. For the sake of this study, the physical mechanism of action of these effects is not relevant beyond identifying which effects only modify photons, rather than creating or destroying photons. That is, only effects which do not require the absorption or emission of photons are considered as distortions from turbulent media. This is because the absorption and then re-emission of a photon can allow for the momentum, energy, and even locality of the re-emitted photon to be modified compared to the absorbed photon. For example, Raman scattering is inelastic, and thus the energy of the re-emitted photon may be different from

that of the absorbed photon, and also the direction of propagation can be similarly modified by the photon interaction modifying the momentum of a material particle. Another example is that of absorption of a photon at a diode junction. The absorption converts the photon into an electrical differential, which then propagates to another diode junction in some other location, where the electrical differential then results in the emission of another photon. This process would lead to a non-locality of the photon from the perspective of the optical field. It is also worth noting that "distortions" and "scattering" from turbulent media are terms which can be used interchangeably.

With the details on the type of distortion out of the way, the effects of these distortions can also be described. In general, the effects of distortion can be described by light propagating after being exposed to a (possibly statistical) mixture of phase profiles. These phase profiles are only constrained by being described on a disk, being continuous and differentiable, and being within the range of $[0, 2\pi)$. An often used basis to describe profiles of this type are the Zernike polynomials (Figure A.1). The Zernike polynomials describe an orthogonal basis over the unit disk, and can be used to describe any phase profile on a disk via up- or down-scaling.

The definition of the Zernike polynomial is

$$Z_n^m(\rho, \varphi) = \begin{cases} R_n^m(\rho) \cos(m\varphi) & m \geq 0 \\ R_n^m(\rho) \sin(m\varphi) & m < 0 \end{cases} \tag{A.25}$$

where $R_n^m(\rho)$ is the radial Zernike polynomial. This polynomial can be calculated in multiple ways, though the one chosen here is to calculate it as

$$R_n^m(\rho) = (-1)^{(|n|-|m|)/2} \rho^{|m|} P_{(|n|-|m|)/2}^{(|m|,0)}(1 - 2\rho^2) \tag{A.26}$$

where $P_n^{(\alpha,\beta)}(x)$ is the Jacobi polynomial of degree n, the form of which will not be discussed for brevity. This form was chosen for convenient computation of the functions, however there are also closed-form representations of $R_n^m(\rho)$ which rely upon the sums of factorials. Generally, the form of these radial Zernike polynomials is that of the positive range of a sinusoidal function rotated around the origin of a polar system, examples of which can be seen in Z_0^0, Z_2^0, and Z_4^0 in Figure A.1. As an alternative, there exists other indexing methods for Zernike polynomial coefficients, like the OSA + 1 method, which indexes the coefficients as $Z_j(\rho, \varphi) = Z_n^m(\rho, \varphi)$ such that

$$j = \frac{n(n+1) + m}{2} + 1. \tag{A.27}$$

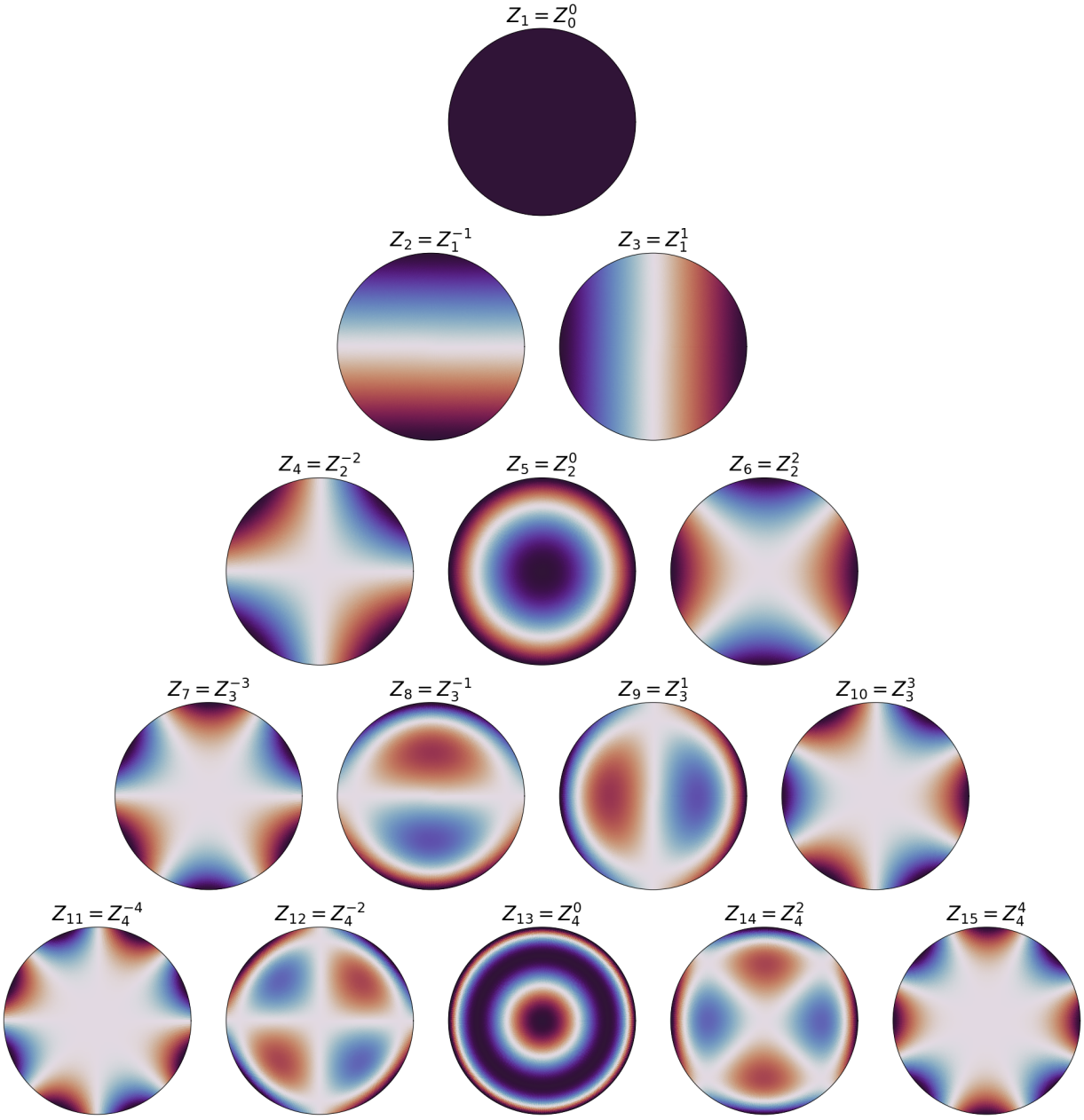

Figure A.1: **The First 15 Zernike Polynomials.** Depicted here are the first 15 Zernike polynomials. They can emulate the effects of multiple different aberrations on the phase profile of a light beam wavefront. These aberrations are outlined in Table 3.1.

A resultant phase profile is a linear combination of Zernike polynomials

$$\Phi(\rho, \varphi) = \sum_{j=0}^{j_{\text{cutoff}}} c_j Z_j(\rho, \varphi) \tag{A.28}$$

where $\{c_j\}$ are the coefficients of each Zernike polynomial, and j_{cutoff} is the cutoff coefficient of the highest utilized Zernike polynomial. In theory $j_{\text{cutoff}} \to \infty$, however in practice this value will be finite. For a single phase profile, it can be applied to an existent electric field as

$$E_{\text{out}}(\rho, \varphi, z) = e^{i\Phi(\rho,\varphi)} E_{\text{in}}(\rho, \varphi, z) \tag{A.29}$$

which can then propagate through space.

To be more general, multiple phase profiles can apply probabilistically to the electric field, and at different locations, and for different durations of time. Such a complex application of phase profiles can be mathematically represented, however for the sake of this study such an explicit representation is not necessary. Instead, this study only pertains to the modifications of the transverse spatial profile of the electric field after being distorted, as compared to the transverse spatial profile of the electric field without being distorted. Assuming that the electric field without distortions at the measurement plane would be $E(\rho, \varphi, z_m)$, then this application of phase profiles can be described by the mapping

$$\mathbf{S} : E(\rho, \varphi, z_m) \to E(\rho^*, \varphi^*, z_m) \tag{A.30}$$

where the mapping only changes the variables ρ and φ into ρ^* and φ^*, and does not affect the actual underlying data. Note that this mapping is not necessarily injective — that is, one value of ρ or φ can map to multiple values of ρ^* or φ^*. This is due to the probabilistic application of the phase profiles.

A.2.2 Noise

The concept of background noise can take many forms, as it can originate from a multitude of different sources. These sources include both real sources like incandescent lights, LED lights, the Sun, and laser sources, as well as electronic sources like electronic noise and sensor dark counts. Each of these sources follows different photon number statistics, though generally they will either be Poissonian or super-Poissonian in nature. A practical quantum imaging scheme would be exposed to a summation of multiple of these sources. As more sources are introduced, and for a high enough overall intensity, the photon number statistics

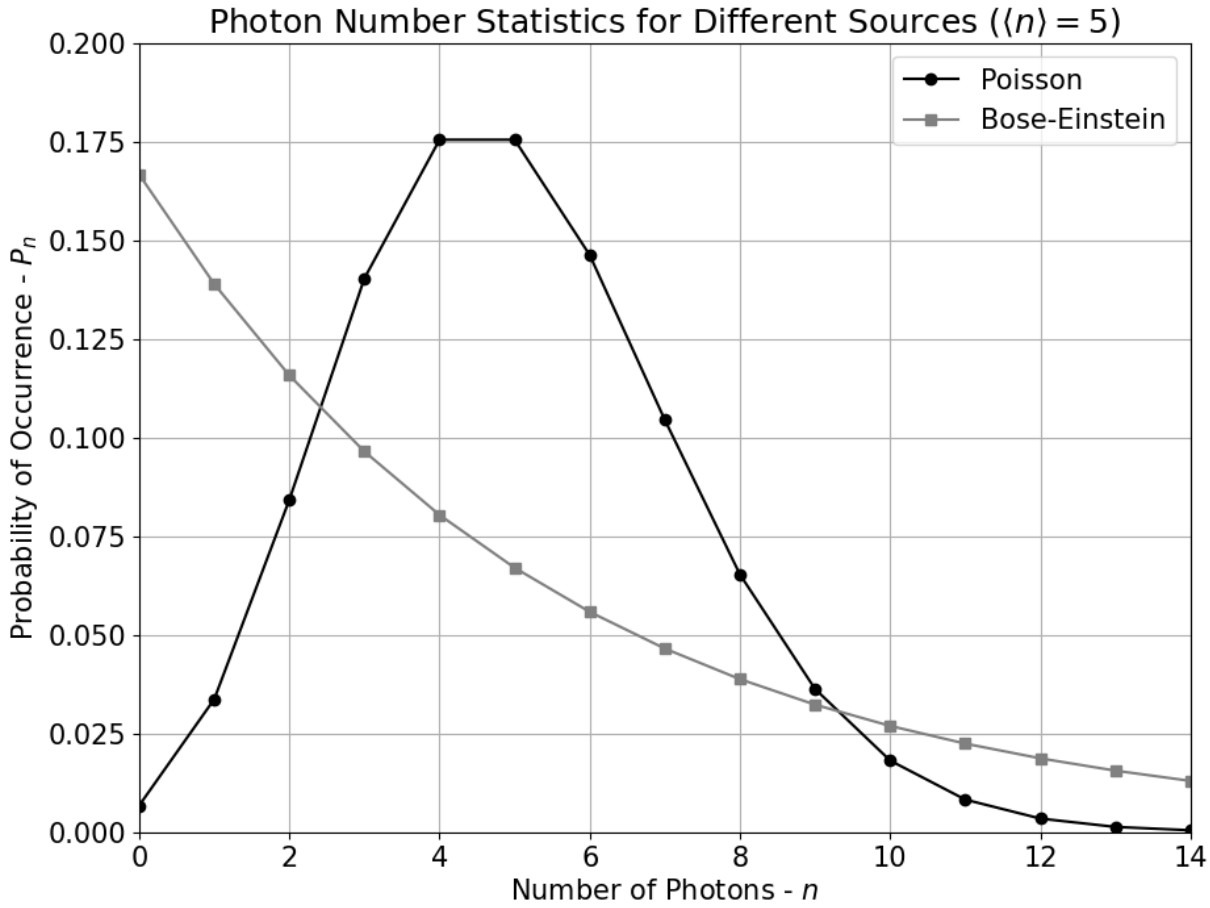

Figure A.2: **Photon Number Statistics for Different Sources.** Here example photon number statistics are shown for two sources with the same average photon number $\langle n \rangle = 5$. The Poissonian statistics are for a coherent state, and the Bose-Einstein statistics are for a thermal state.

will simply approach that of Poissonian statistics. This arises simply from the summing of different statistical sources, the justification for which is given in the following paragraph.

Consider there to be N sources, where each source is a single-mode thermal distribution of approximately the same average intensity $\bar{I}_j \sim \bar{n}_j$, where $\bar{n}_j = \langle n_j \rangle$ is the average expected photon number per unit time for the j^{th} source. The expected photon number per unit time of all these sources combined is

$$\bar{n} = \sum_j^N \bar{n}_j = N\bar{n}_j \sim \bar{I}. \tag{A.31}$$

It is known that each source will then have a variance in expected number of overall photons arriving of

$$\Delta^2 n_j = \bar{n}_j + \bar{n}_j^2 \approx \bar{n}_j^2, \tag{A.32}$$

as the photon statistics of a thermal source follow a Bose-Einstein distribution of the form

$$P_n = \frac{1}{\langle n \rangle + 1} \left(\frac{\langle n \rangle}{\langle n \rangle + 1} \right)^n \tag{A.33}$$

an example of which can be seen in Figure A.2 for $\langle n \rangle = 5$. The sources are assumed to each be independent. In this case, the variance of all the sources combined is then

$$\Delta^2 n = \sum_j^N \Delta^2 n_j = N(\bar{n}_j + \bar{n}_j^2) = \bar{n} + \frac{\bar{n}^2}{N}. \tag{A.34}$$

These sources are assumed to be classical, and of relatively high intensity, and thus since $\bar{n}$ is large $\Rightarrow \bar{n}^2 \gg \bar{n}$. This approximates the variance of the sum of all the sources as

$$\Delta^2 n \approx \bar{n} \sim \bar{I} \tag{A.35}$$

which is described by a Poissonian distribution. The photon number statistics for a Poissonian distribution are given by

$$P_n = \frac{e^{-\langle n \rangle} \langle n \rangle^n}{n!} \tag{A.36}$$

an example of which can be seen in Figure A.2 for $\langle n \rangle = 5$.

The spatial distribution of the arrival of photons from these sources will follow no pattern, and thus there will be no spatial correlations. For a combination of sources, the profile will likely be flat, while for a laser source the profile will follow that of the

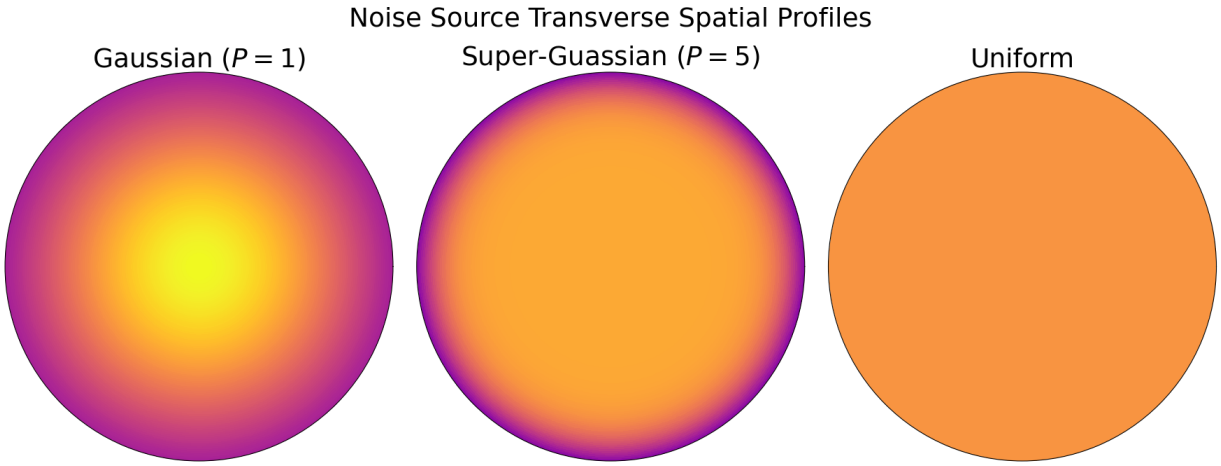

Figure A.3: **Noise Source Transverse Spatial Profiles.** Three different noise source transverse spatial profiles for Gaussian ($P = 1$), super-Gaussian ($P = 5$), and uniform sources. All three have the same scale, and are normalized such that the integral over the whole displayed area is 1. As $P \to \infty$, the super-Gaussian quickly approaches a uniform source.

laser, which is typically super-Gaussian. Examples of these spatial profiles are shown in Figure A.3. A super-Gaussian profile can be described by

$$G(r, P) = e^{-r^{2P}} \tag{A.37}$$

where r is the distance from the beam center, and P is the power of the super-Gaussian. $G(r, P)$ will quickly approach a uniform profile as $P \to \infty$.

A.3 Signal Metrics

To quantify the efficacy of any imaging setup, it is necessary to define observable metrics. There are many different metrics which are worth investigating, but for the sake of this investigation the signal-to-background ratio, the signal-to-noise ratio, and the fidelity are the main metrics of interset.

A.3.1 Signal-to-Background Ratio

The signal-to-background ratio (SBR) can be calculated theoretically for an image as

$$SBR = \frac{\mu_{\text{sig}}}{\mu_{\text{noise}}} \tag{A.38}$$

where μ is the average number of events per pixel in the area indicated by the subscripted region. Note that for this section, the use of the word "signal" refers to any photons from SDPC, rather than the signal photon from the pair. To distinguish this, the subscript "sig" is used in equations. While this is the optimal theoretical calculation, determining these values requires knowledge of the signal counts, added noise counts, dark and ambient counts, and signal area, which are all non-trivial values to calculate from the data.

The first value to be determined is the contribution to the event counts from both the dark counts and ambient photon events, collectively referred to here as "background" events. These background events are only part of the overall noise along with the added noise, however to calculate the amount of added noise alone, as well as to calculate the number of events attributed to only the signal, these quantities must all be determined separately. Defining the background can be done by taking a region of the image where no signal is present and calculating the average value of each pixel in that region. The area of the region is given as A_{bg}, and the total number of events in that region is N_{bg}. In order to minimize the effect of the radial variance in the background intensity, the background region can be chosen to occupy a region of the image equidistant from the center of the image region as compared to the to-be-selected signal region. The average background rate value can then be calculated as

$$\mu_{\text{bg}} = \frac{N_{\text{bg}}}{A_{\text{bg}}} \tag{A.39}$$

which will need to be re-calculated for each image.

Calculating μ_{sig} poses a challenge since the signal has an undetermined and potentially probabilistic spatial profile. Thus defining the signal region is difficult. The signal counts N_{sig} can be found by taking a calibration measurement which has no added noise, and defining a region with area A_{sig} which encompasses the signal. The number of events in that region are counted as N_{A}, and the number of background photons in the signal region can then be estimated by using the previously calculated μ_{bg} and signal area. This results in

$$N_{\text{sig}} = N_{\text{A}} - \mu_{\text{bg}} A_{\text{sig}}. \tag{A.40}$$

The value of μ_{sig} can then be calculated as

$$\mu_{\text{sig}} = \frac{N_{\text{sig}}}{A_{\text{sig}}} \tag{A.41}$$

however, it is important to note that A_{sig} should be very tight around the signal to best estimate the true value of μ_{sig}.

Finally, calculating μ_{noise} requires a similar, yet slightly modified approach as calculating μ_{sig}. The number of total noise events N_{noise} within A_{sig} can be found from all events within the region A_{sig}. This quantity is represented to as N_{A}, and differs from N_{sig} in that N_{A} is calculated based on the number of both signal and noise counts in A_{sig} for each measurement, whereas N_{sig} is based only on the signal counts in that region, and is assumed to be the same for all data sets as it was calculated one time from a calibration data set. Based on this, the number of noise counts can be calculated as

$$N_{\text{noise}} = N_{\text{A}} - N_{\text{sig}} \tag{A.42}$$

where it is important to note that this assumes that N_{bg} is thus implicitly included in N_{noise}. Further, it should be pointed out that this value a is good approximation, though it is not exact, even if the flux and profile of the signal is the same as it was during the calibration measurement. This is because there will always be a variance in number count of photons at any specific pixel due to the statistical nature of light. This variance is minimized by taking longer integration times, however since the measurements of the pixels are considered as an ensemble, the variance from each pixel is multiplicative over the whole set of pixels. Thus, this approximation can be made more accurate by a combination of longer integration times, as well as larger values of A_{sig}. The value of μ_{noise} can then be calculated as

$$\mu_{\text{noise}} = N_{\text{noise}}/A_{\text{sig}} \tag{A.43}$$

again with the caveat that A_{sig} is tight. This value can be used to determine the SBR using Equation (A.38).

A.3.2 Signal-to-Noise Ratio

The signal-to-noise ratio (SNR) can be calculated theoretically as:

$$SNR = \frac{\mu_{\text{sig}}}{\sigma_{\text{noise}}} \tag{A.44}$$

where μ_{sig} is calculated from above. The value of σ_{noise} can be determined by

$$\sigma_{\text{noise}} = \sum_{\forall p \in \{\text{sig}\}} \sqrt{\frac{N_{\text{noise},p} - \mu_{\text{noise}}}{A_{\text{sig}}}} \tag{A.45}$$

where {sig} is the set of all pixels in the region defined by A_{sig}, and $N_{\text{noise},p}$ is the number of noise counts in pixel p. This presents a practical problem though, as to accurately estimate how many counts in a particular pixel are from noise events requires a very long integration time. This is because, similar to the estimation in Equation (A.42), the error of the estimation is dependent on the error of each pixel in consideration. For the SBR, the measurements on each pixel are considered an ensemble, and thus the total error of the measurement is multiplicative over the pixels. For this estimation of SNR however, the pixels are not considered an ensemble, and instead are summed. This causes the error from each pixel's measurement to be additive rather than multiplicative. Thus, a very long integration time is needed to minimize the error in this measurement. Since most of the exposures in this work are generally short, this metric will have very high error, and is impractical.

To standardize the variables from the last two sections for a measurement with any integration time duration, take every mention of counts (N), average (μ), and standard deviation (σ) as per second.

A.3.3 Fidelity

Since σ_{noise} cannot be accurately calculated, an estimate for SNR which scales similarly to the SBR is desired. Further, since the structure of the target will be able to be changed by the distortions introduced from turbulent media, this estimator should further indicate how similar a final image is to an objective target. Such an estimator is the fidelity metric. This fidelity metric is based on performing a zero-normalized-cross-correlation measurement between the final TSFQCI image and a reference image. Because this fidelity metric normalizes by the standard deviation of the whole image measurement at once, the error of the metric scales well by both the size of the image and the integration time of the measurement.

A zero-normalized cross-correlation measurement consists of scanning a reference image over all possible locations of the target image, and calculating a value. This value, referred to as the cross-correlation value $\text{CXC}(x, y)$ is calculated as

$$\begin{aligned}\text{CXC}(x', y') = \frac{1}{(nx_r ny_r) + (nx_t ny_t)} \sum_{x,y} \frac{1}{\sigma_r \sigma_t} (r(x - x', y - y') - \mu_r)(t(x, y) - \mu_t) \\ \forall \{(x', y') : x' \in \mathbb{Z} < nx_r + nx_t, y' \in \mathbb{Z} < ny_r + ny_t, \}\end{aligned} \tag{A.46}$$

where nx and ny are the number of pixels in the x and y axes of an image, σ the standard deviation of the pixel values in an image, and μ the average of the pixel values in an image,

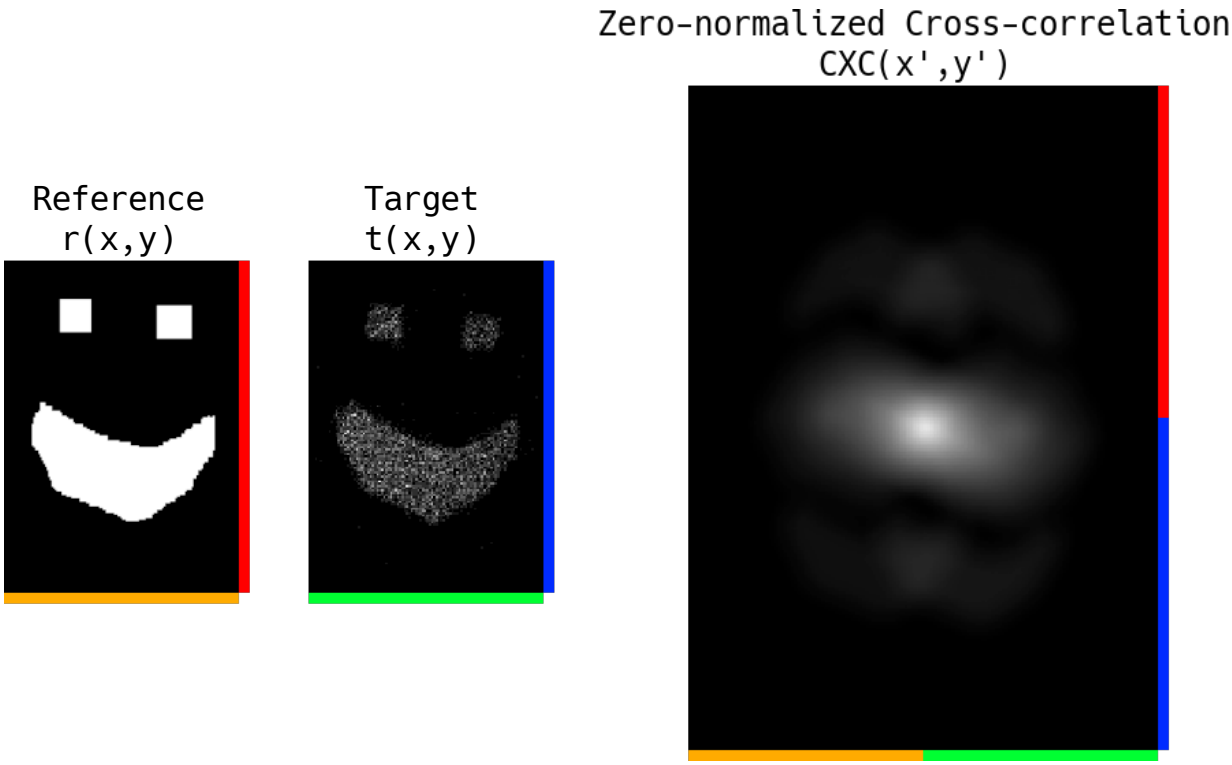

Figure A.4: **Zero-Normalized Cross-Correlation.** An example of a zero-normalized cross-correlation measurement between a reference and target image. In all three images, white is a value of 1, while black is a value of 0. The width of the CXC image is the sum of the widths of the reference and target images, while the height is the sum of the heights of the reference and target images. The maximum of CXC occurs at the center, indicating that the location of the target within the target bounds is the same as the location of the reference within the reference bounds. The value of CXC at this location is 0.7, indicating a 70% similarity of the target image to the reference image.

each calculated for both the reference and target images, respectively. An example of this measurement is shown in Figure A.4.

The fidelity is the value, as a percentage, of the maximum of $\mathrm{CXC}(x', y')$ such that

$$\mathrm{Fidelity}(t(x, y)) = \max\left[\mathrm{CXC}(x', y')\right] \tag{A.47}$$

is the fidelity for some image $t(x, y)$. Further, the location of the maximum, $(x'_{\max}, y'_{\max})$, is the location within the CXC image space where the reference image overlaps the target image maximally. As such, the location of the center of the target within the target image space can be calculated as

$$(x_t, y_t) = (x'_{\max} - nx_t, y'_{\max} - ny_t). \tag{A.48}$$

A.4 Calculating Spatial Filter Accidentals and Acceptance Probabilities

For this section, $g(\vec{x_i}' + \vec{x_s}')$ will be assumed to be some symmetric 2D Gaussian with variance in all directions of δx. In order to utilize a spatial filter, one of two approaches can be taken: (1) the photons are accepted/rejected based on the probability density function of the correlations at the point in that function space where the pair exists, or (2) a threshold value on the correlation probability density function is set and any pairs which exists at a point outside that radius in the function are rejected, and any inside are accepted. In implementation (1), the likelihood of accepting any specific photon pair $(\vec{x_i}', \vec{x_s}')$, regardless of the origin of the photons, is given by

$$P_1(\vec{x_i}', \vec{x_s}') = \frac{g(\vec{x_i}' + \vec{x_s}')}{g_{\max}} \tag{A.49}$$

where $g_{\max}$ is the $\max_C[g(\vec{x_i} + \vec{x_s})]\ \forall(\vec{x_i}, \vec{x_s}) \in C$. Implementation (2) has the likelihood of accepting any specific photon pair $(\vec{x_i}', \vec{x_s}')$ as

$$P_2(\vec{x_i}', \vec{x_s}') = \Pi\left(\frac{\|\vec{x_i}' + \vec{x_s}'\|}{x_{\mathrm{thresh}}}\right) \tag{A.50}$$

where $\Pi(t/x_{\mathrm{thresh}})$ is the rectangular function which is valued 1 where $t < x_{\mathrm{thresh}}$ and 0 otherwise.

With either filter, there is a chance that even a true signal-idler pair will not be coincidenced, and similarly that a false noise-idler pair will be accidentally coincidenced.

Considering each of these scenarios is important in selecting which filter to use. For filter (1), the chance of rejecting a true signal-idler pair can be considered by finding the probability of a photon pair being rejected multiplied by the likelihood of that photon pair being generated. Since $g(\vec{x_i}' + \vec{x_s}')$ is symmetric, this problem can be simplified by performing the variable remapping $\|\vec{x_i'} + \vec{x_s'}\| \to x'$, which remaps the space $C \to \|C\|$. Thus, the probability of a true signal-idler pair being rejected by the filter is

$$\begin{aligned} P_{1\checkmark\times} &= \int_{\|C\|} |(1 - P_1(x'))||g(x')|dx' \\ &= \int_0^{2|A_s|} |g(x')| - \frac{|g(x')|^2}{g_{\max}} dx' \\ &= 1 - \frac{1}{\sqrt{2}} \approx 0.293 \end{aligned} \tag{A.51}$$

since $g_{\max} = (2\delta x\sqrt{\pi})^{-1}$ as per the definition of a normalized Gaussian.

Similarly, the chance of accepting a noise-idler pair with (1) is the probability of accepting a noise-idler pair times the likelihood of that pair generating. Since the noise photon and idler photon are uncorrelated, and the noise photons' locations of arrival are evenly distributed throughout A_s, the chance of any specific pair generating is equal over $A_i \otimes A_s$. This unfortunately is no longer a symmetric problem, and so to perform the integration requires understanding the remapping of variables in more detail. During the remapping, the uniform distribution over the 4D space $A_i \otimes A_s$ becomes a normal distribution in the 1D space $\|C\|$ via two steps: first an addition of two uniform normal variables in $(\vec{x_i}, \vec{x_s}) \to \vec{x_i} + \vec{x_s}$, followed by the squaring, adding, and square rooting of the uniform variables from the previous space in $\vec{x_i} + \vec{x_s} \to \|\vec{x_i} + \vec{x_s}\|$.

To calculate the final distribution of $(\vec{x_i}, \vec{x_{\text{ext}}})$ in $\|C\|$, the distributions of the components of each vector are first considered. For $\vec{x_{\text{ext}}}$, both the x and y components follow a uniform random distribution with width $\sqrt{|A_s|}$, and thus equal variances

$$\delta x_{\text{ext}} = \frac{\sqrt{|A_s|}}{12}. \tag{A.52}$$

The distribution of $\vec{x_{\text{ext}}}$ is then uniform random with width $|A_s|$. The distribution of $\vec{x_i}$ can in practice be not so simple, but for the sake of this argument it can be approximated to be similarly uniform random with width $|A_i|$, resulting in the equal variances of each component being

$$\delta x_i = \frac{\sqrt{|A_i|}}{12}. \tag{A.53}$$

When performing $\vec{x_+} = \vec{x_i} + \vec{x_{\text{ext}}}$ the distributions in x_{+x} and x_{+y} will both become normal, with equal widths of

$$\delta x_+ = \delta x_i + \delta x_{\text{ext}} = \frac{\sqrt{|A_i|}}{12} + \frac{\sqrt{|A_s|}}{12} = \frac{\sqrt{|A_s|}}{6} \tag{A.54}$$

since $|A_i| = |A_s|$ by definition in Equation (2.2). Since $\vec{x_+}$ is a multivariate Gaussian distribution, it is known that the distribution of $\|\vec{x_+}\|$ is given by a χ distribution. More specifically, since $\vec{x_+}$ is two-dimensional, the distribution is that of a Rayleigh distribution [60] with variance of δx_+^2, which is of the form

$$\begin{aligned}\chi(x) &= \frac{x}{\delta x_+^4} e^{-x^2/(2\delta x_+^4)} \\ &= \frac{1296x}{|A_s|^2} e^{-648x^2/|A_s|^2}.\end{aligned} \tag{A.55}$$

Using the Rayleigh distribution above to represent the distribution of pairs in the $\|C\|$ space, the chance of an accidental is

$$\begin{aligned}P_{1\times} &= \int_{\|C\|} |P_1(x')|\chi(x')dx' \\ &= \int_{\|C\|} \frac{|g(x')|\chi(x')}{g_{\max}} dx' \\ &= \int_0^{2|A_s|} \frac{1296}{|A_s|} x e^{\frac{-648x^2}{|A_s|^2} - \frac{x^2}{2\delta x^2}} \\ &= \frac{1296\delta x^2 \left(1 - e^{-2592 - 2|A_s|^2/\delta x^2}\right)}{|A_s|^2 + 1296\delta x^2}\end{aligned} \tag{A.56}$$

which is again, a difficult function to interpret analytically. The graph of this function in Figure A.5 shows that the scaling of this probability with the ratio of $\delta x/|A_s|$ is approximately quadratic at tighter filters, before quickly leveling off to likely pair each idler photon which is missing a signal photon with a noise photon. In conclusion, for filter (1), the chance of an accidental grows quickly and quadraticallly with the width of the correlation, while the chance of a missed real pair is 29.3%.

For filter (2), the probability of a missed signal-idler pair occurring is the portion of $g(\vec{x'})$ which is not within the distance x_{thresh}. In other words, after performing the same variable remapping as above, $|x'| < x_{\text{thresh}}$. This portion is equivalent to

$$P_{2\checkmark\times} = \int_C (1 - P_2(x'))|g(x')|dx' = \int_0^{x_{\text{thresh}}} |g(x')|dx' = 1 - \text{erf}\left(\frac{x_{\text{thresh}}}{\sqrt{2\delta x^2}}\right) \tag{A.57}$$

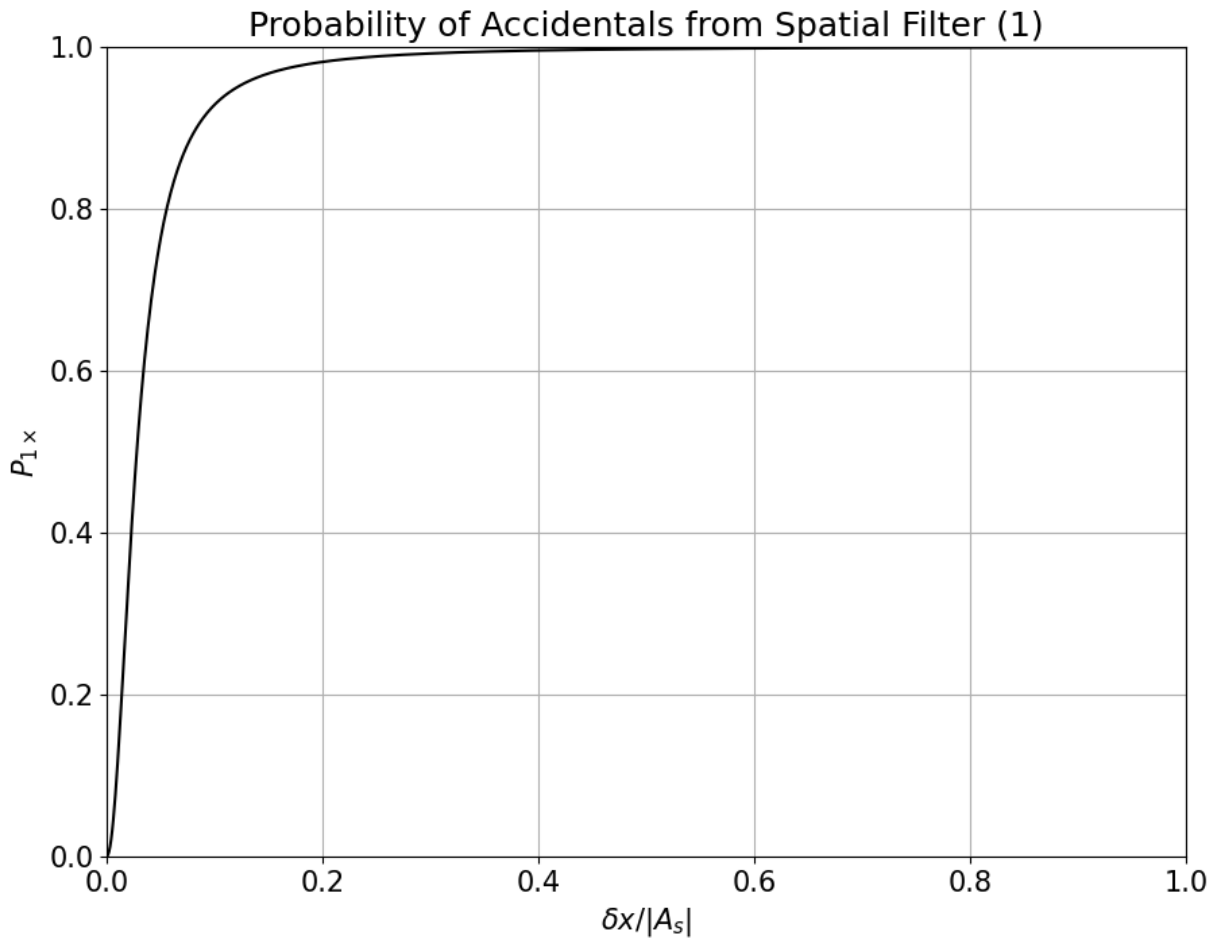

Figure A.5: **Probability of Accidentals from Spatial Filter (1).** Shown here is the probability of a noise-idler pair being accepted when using spatial filter (1). Of note, is that the probability of accidental acceptance increases quickly with the square of the ratio of the coincidences' width to the size of the $|A_s|$ region $(\delta x/|A_s|)^2$.

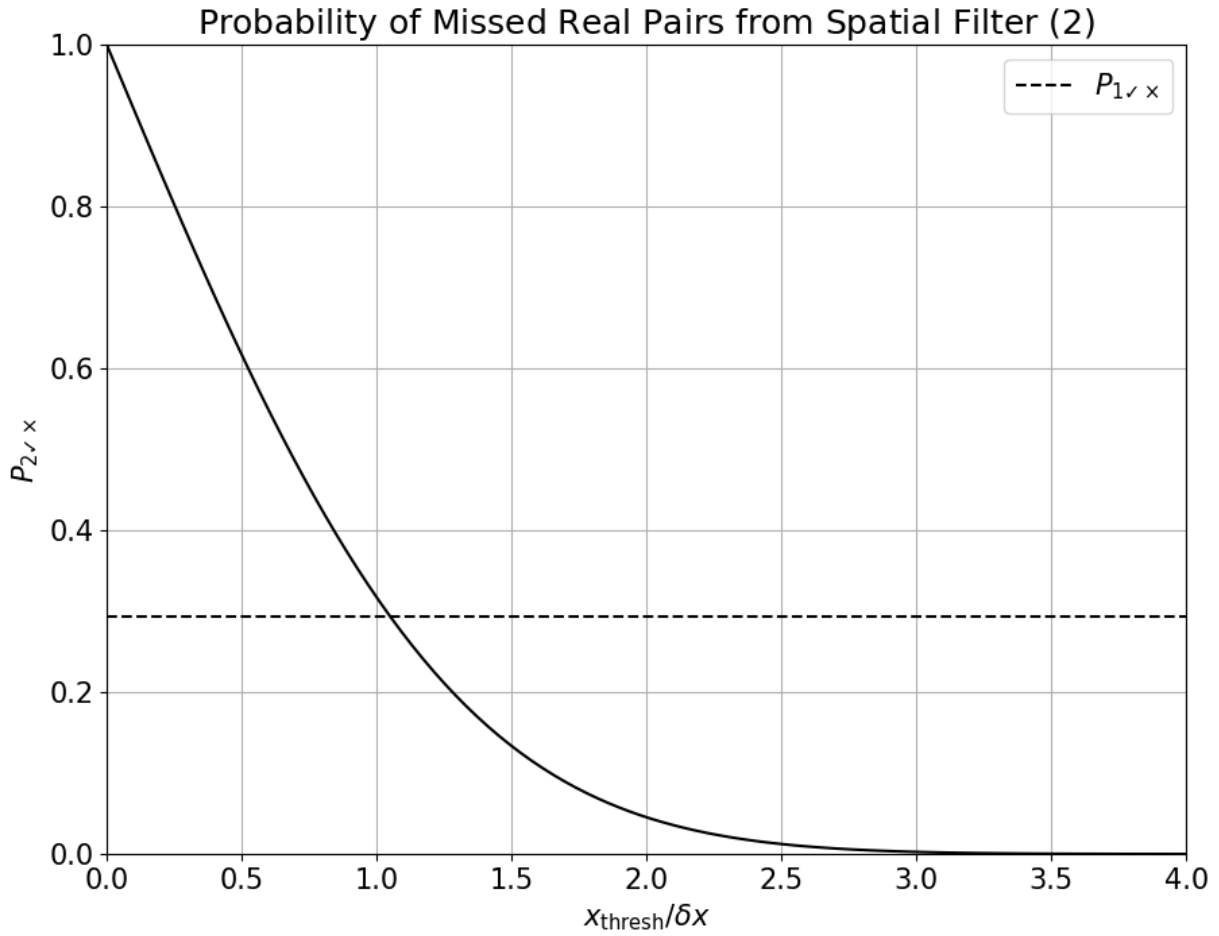

Figure A.6: **Probability of Missed Real Pairs from Spatial Filter (2).** Shown here is the probability of a signal-idler pair being rejected when using spatial filter (2). This probability quickly approaches 0% as the ratio of $x_{\text{thresh}}/\delta x$ increases. The value of $P_{1\checkmark\times}$ is also shown for comparison.

where erf(x) is the error function. The graph of this function in Figure A.6 shows that the probability of missing a true pair quickly approaches 0% as the ratio of $x_{\text{thresh}}/\delta x$ increases. For instance, a choice of $x_{\text{thresh}} = 2\delta x$, which is twice the variance of $g(\vec{x'})$, has a 4.5% probability of true pair rejection.

As for accidental noise-idler acceptances, the distribution $\chi(x)$ must again be considered. Using the same definition as given in Equation (A.55) for $\chi(x)$, the probability of a noise-idler accidental acceptance is

$$\begin{aligned} P_{2\times} &= \int_C P_2(x')\chi(x')dx' \\ &= \int_0^{x_{\text{thresh}}} \chi(x')dx' \\ &= 1 - e^{\frac{-648x_{\text{thresh}}^2}{|A_s|^2}}. \end{aligned} \tag{A.58}$$

To more easily compare this function, it is graphed for multiple x_{thresh} values, which are multiples of δx in Figure A.7 alongside $P_{1\times}$. It can be seen that, while the probability of accidentals acceptance is generally higher than it is for filter (1), it is still comparable, especially for strong correlations. In conclusion, for filter (2), the chance of an accidental acceptance grows similarly to how it does for filter (1), while the chance of a missed real pair can be made very low, especially compared to filter (1) where this metric cannot be controlled. As such, filter (2) will be considered for the rest of this thesis.

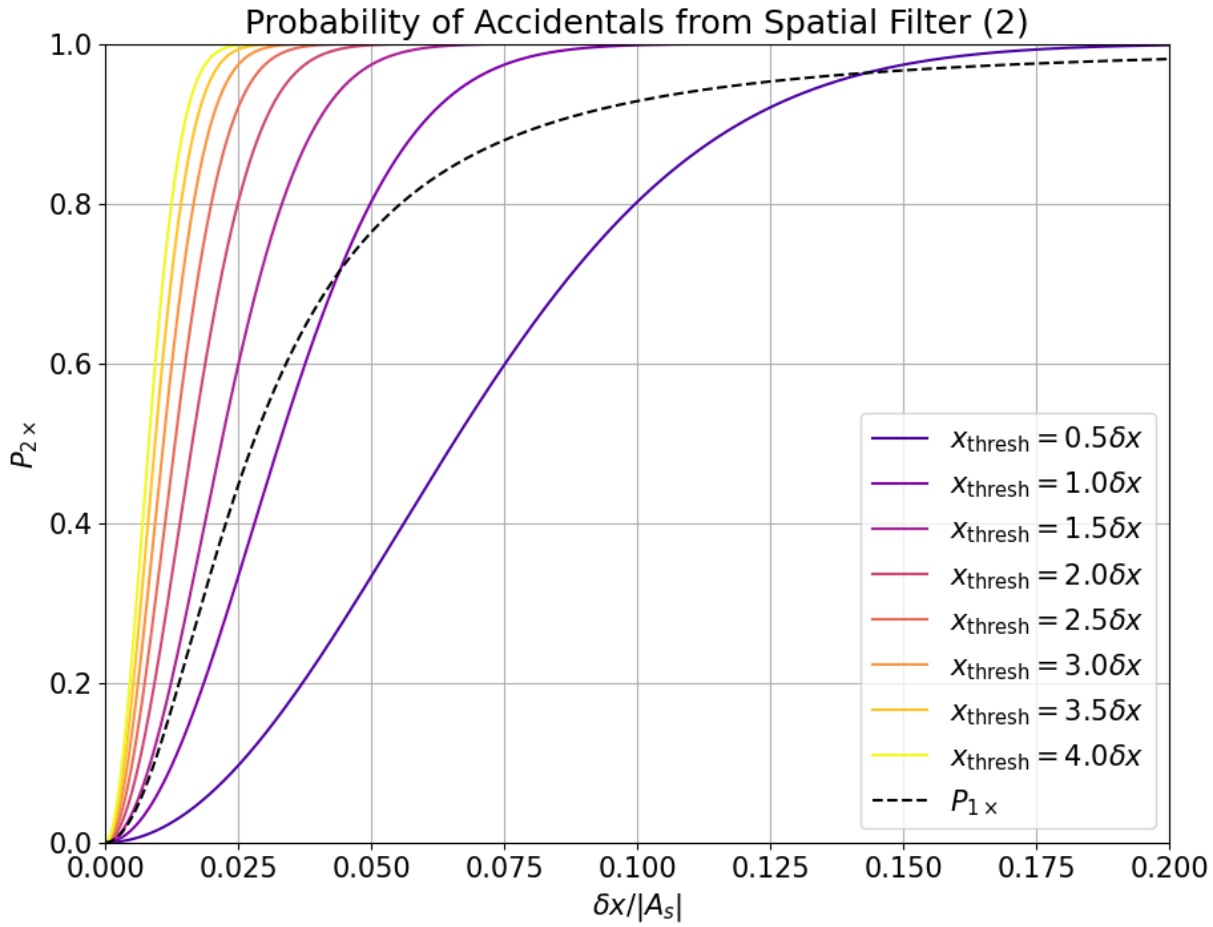

Figure A.7: **Probability of Accidentals from Spatial Filter (2).** Shown here is the probability of a noise-idler pair being accepted when using spatial filter (2). The probability for multiple threshold values x_{thresh} are shown, where the thresholds are multiples of δx. The probability of accidentals from spatial filter (1) $P_{1\times}$ is also shown for comparison. Generally, the filters have a higher, though comparable, accidental acceptance probability as compared to filter (1).

A.5 Processing Events from the TPX3CAM

The TPX3CAM device is able to stream information at up to 10Gbit/s, with an average of $5 - 20$ million events being communicated per second. As a result, the parsing, processing, and analyzing of the data from the camera requires very careful consideration and optimization in order to be performed in a feasible amount of time. Further, especially for exposures longer than a few seconds, the size of the data sets are typically on the scale of $>$ 100GB, and can require over 1000GB of computer memory to process in total. As such, big-data processing techniques must be employed in order to arrive at results without extensive use of computer clusters.

A.5.1 Parsing Events

The TPX3CAM device outputs events as a binary data stream, where each event corresponds to a 64-bit long word. These words can represent multiple different event types, but for the sake of this work only the "Pix" event type is of importance. The parsing of a pix event is shown in Table A.1. There are two methods by which the events can be retrieved from the TPX3CAM device. The first is by a direct data stream from the camera during acquisition time. The second is by retrieval from a raw data stream dump file after acquisition time. The former method requires communication with a Java server in order to request and receive packets, while the latter simply requires locating the file on disk. As a result, it is more convenient to read from the file than from the direct data stream.

In order to preserve the nearly-sorted order of the data as it is in the file, the parsing of the file is done serially. To efficiently iterate over the byte steam in the file, and also to perform the bitwise operations efficiently, the code to parse the files is written using the Rust programming language [2]. This program simply iterates over each 64-bit word in the file, and then performs the parsing outlined in Table A.1.(a).

A.5.2 Clustering Intensified Photon Events into Single Photon Events

As mentioned in the previous chapter, when a single photon event arrives at the intensifier, it creates $\mathcal{O}(10^5)$ photons, which then trigger some number of pixels on the detector. As a result, the arrival of a single photon results in many events on the camera which can be spread in time by up to 100 ns, and spread in space by up to 500 μm. In order to gain

Data	Type(0xB)	DCol	SPix	PixRaw	ToA	ToT	FToA	SPIDR
Bits	$60-63$	$53-59$	$47-52$	$44-46$	$30-43$	$20-29$	$16-19$	$0-15$

(a) Pix Word Parsing Table

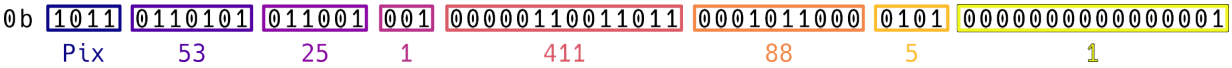

(b) An Example of a Parsed Pix Word

$$
\begin{aligned}
X &= 255 - (4(25) + 1) && = 154\,\text{pixels} \\
Y &= 255 - \left(2(53) + \left\lfloor \frac{1}{4} \right\rfloor\right) && = 149\,\text{pixels} \\
\text{ToA} &= 409600(1) + 1.5625(4(411) + (15 - 5)) && = 419890.625\,\text{ns} \\
\text{ToT} &= 25(88) && = 2200\,\text{ns}
\end{aligned}
$$

(c) Calculation of Example Parameters

Table A.1: **TPX3CAM Pix Event Parsing.** The key for the parsing of a single event from the TPX3CAM is shown here in (a). The binary string is broken up into 8 bit fields, with the first bit field indicating the type of the event, and the other 7 bit fields being used to convey the position and time information. The parsing of those fields from an example binary stream event output is shown in (b). These values are then used to calculate the X-Y positions, the ToA, and the ToT in (c).

information about the initial single photon event, this set of events must be clustered into one location and time of arrival (ToA). The algorithmic implementation of this clustering algorithm follows the outline given in [70], though it will also be explained here.

The output from the data stream parsing is stored in either a NumPy or CuPy array. The dynamic use of these two Python packages allows for utilization of CUDA processing on systems which support it, while still allowing normal CPU parallelization on non-CUDA supporting systems. Going forward, any algorithms described as being vectorized can be assumed to dynamically work with both NumPy and CuPy, unless otherwise noted. The arrays are then sorted by time utilizing a timsort algorithm, as this algorithm is shown to be efficient for nearly-sorted data [8]. To identify the centroid, the ToT of all events are considered and compared to their neighboring events within some set time and position distance. The event with the longest ToT within that time and space distance is considered the centroid of each cluster, and all other events in the cluster are removed. This reduces the data set by approximately 10×.

A.5.3 Coincidencing Single Photon Events

After the data is clustered and reduced to represent single photon events, the events can then be coincidenced based on ToA. In order to do so the photon events must be first labeled as being events which occur in either the signal or idler region. The regions are identified after previewing the data, and any events which occur outside these two regions are removed from the data set. The sets of signal and idler events are simultaneously sorted in time, and then the time differences (dToA) between the signal and idler events are considered. Each idler event is compared to all signal events within a given time window, and the signal-idler event with the lowest dToA is considered as a potential pair. This is repeated until the all possible pairs with dToA less than a given cutoff value are identified. Any unpaired photons are removed from the data set. This results in a list of possible coincidence events based on ToA only. Further, the dToA of the pairs can be as large as the cutoff value. Once these pairs are found, they are used as the baseline for all further data analysis. Typically, by this point, enough events have been removed from the data set that traditional processing techniques can be utilized without needing to worry about significant computational memory costs.

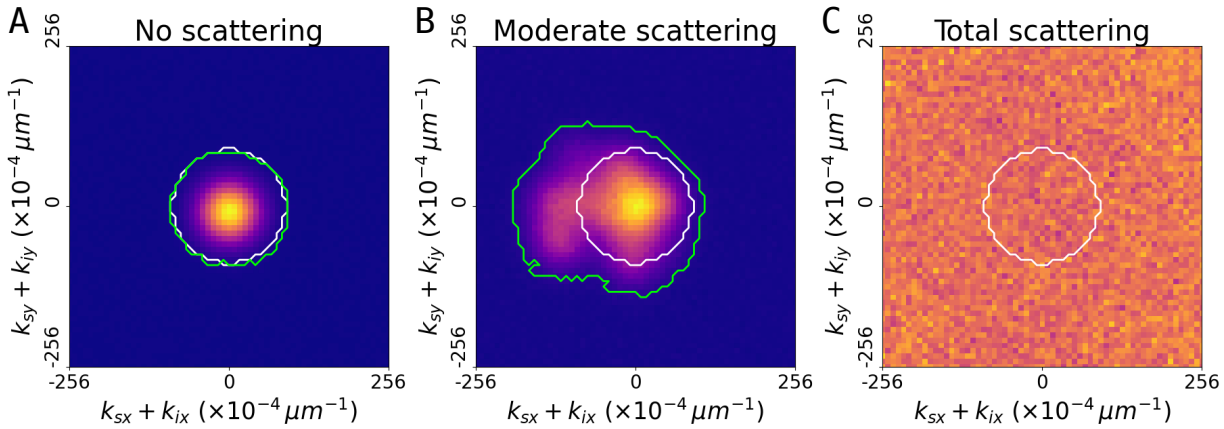

Figure A.8: **Comparison of Standard and Dynamic Spatial Filters at Different Distortion Strengths.** The simple filter (white outline) and spatial $g^{(2)}$ filter (green outline) for three scenarios: no scattering (A), moderate scattering (B), and total scattering (C). In the total scattering scenario, all momenta combinations are considered in the spatial $g^{(2)}$ filter, and thus the green outline is not visible. No background signal is present in this simulated data set. Since the maximum number of pairs in each bin is dependent on the strength of scattering, the plots are all normalized to their respective maxima.

A.6 Behavior of TSFQCI Through Different Scattering Strengths

Since the maximum possible value of the spatial $g^{(2)}$ metric is dependent on the strength of the distortion from the turbulent media for a finite exposure time, it is valuable to discuss the behavior of the filter for different scattering strengths, and compare it to the behavior of the simple spatial filter. This will allow for determining the upper and lower bounds on the effectiveness of the filter. For the sake of having the scattering strength as the only variable it is assumed that $\delta(k_s + k_i)$ is fixed before the scattering is applied, and also that there is no added background signal. The results here are from simulated data.

No Scattering

In the case of no scattering, the spatial $g^{(2)}$ filter will only allow pairs which fall very close to the momenta bins within the range $\delta(k_s + k_i)$ (Figure A.8.A, green outline). Thus, the modified filter will perform nearly identically to the simple filter when no scattering

is present (Figure A.8.A, white outline). With background signal present, the spatial $g^{(2)}$ filter may allow slightly more accidentals through as compared to the simple filter.

Extreme Scattering

In the extreme case of a total scattering which maps the input spatial modes in such a way that all entries in all momenta bins are uniform-randomly redistributed among all other momenta bins, then the spatial $g^{(2)}$ filter will capture all momenta bins (Figure A.8.C, green outline (off-plot)). With no added background signal, this perfectly captures all light from the SPDC source. This is opposed to the simple filter (Figure A.8.C, white outline) which will only capture a proportion of the SPDC light equal to the ratio between the area of the simple filter and the whole momenta-combination space area. With background noise present, the spatial $g^{(2)}$ filter would include more accidentals than the simple filter. Due to the uniform-random redistribution, however, the momentum bins within the simple filter will consist of a combination of actual and accidental correlated pairs, with proportions identical to those in the image without the filter. As such, the simple filter will drastically lower the overall photon count of the resultant image, without raising the contrast, whereas the modified filter will not affect the contrast, but also will not lower the photon count. Thus, the modified filter will out-perform the simple filter.

Moderate Scattering

In the case of a moderate scattering, the spatial $g^{(2)}$ filter will capture most or all of the bins containing the actual correlated pairs (Figure A.8.B, green outline). The simple filter may capture some subset of the actual correlated pairs, but will miss many of the pairs which were scattered out of the momenta bins within $\delta(k_s + k_i)$, which will on average scale with the strength scattering (Figure A.8.B, white outline). Thus, the stronger the scattering, the better the spatial $g^{(2)}$ filter performs compared to the simple filter. When background signal is present, the spatial $g^{(2)}$ filter will likely capture some accidentals, however the simple filter may as well.

Conclusion

This investigation helps identify the lower and upper limits on the performance of the spatial $g^{(2)}$ filter. The spatial $g^{(2)}$ filter's upper performance limit is to perform as well as the simple filter would perform if the distortions from turbulent media were undone on the

same data set. This is equivalent to performing the filter described by Equation (A.16) after performing the inverse mapping $\vec{k_s} = \mathbf{S}^{-1}\vec{k_s}'$. This would only occur if either no scattering is present to begin with and thus $\mathbf{S} = \mathbf{S}^{-1} = \mathbf{I}$, or if no background signal is present and thus all events are preserved, though it is the upper bound on the performance limit nonetheless. The lower bound for the performance limit occurs when there is total scattering and background signal, in which case the lower bound for the performance is to perform as well as traditional ghost imaging. This limit is unsurprising, as all transverse spatial information will be lost in the signal beam. In this work, and in most possible applications, this filter would be employed in the moderate scattering regime, likely not far from the no-scattering limit, and thus will typically perform closer to the upper bound limit than to the lower bound limit.

A.6.1 Simulating Beam Modification

Aside from the generation of photon events, the other aspect of the experimental system which can be simulated are the beam modifications. This includes masking the beam with a transmissive target, as well as distorting the beam to emulate the distortion effects from turbulent media. While the former is relatively simple to implement, the latter has posed significant challenges, and at the time of writing this thesis is still a work in progress. Regardless, both will be described here.

Beam Masking

In order to emulate the target being present within a beam path, beam masking is utilized. This concept takes an array representing the beam mask which has some 2D size, and has values of either 0 or 1. Each event inside the data set then has its position crosschecked with the values in the beam mask. If the value of the mask at the location of the event is 0, then the event is removed from the data set. If the value is 1, then the event is left unchanged. In order to prevent copious mask sizes, this can be performed on a subset of the data set, rather than the entire data set at once. As an extension to this, it is possible to instead allow the mask to have any value in the range $[0, 1]$, in which case the mask value would represent a probability that events at that position will be removed from the data set or not. This extension has not yet been shown to be useful, and as such does not come up again in this work.

Beam Distorting

The effect of turbulent media on the beam is complex. Generally, turbulent media applies a phase mask, or sequence of phase masks, to the propagating light within one of the beam paths. As such, this would be a reasonable starting point for simulating such a distortion. Unfortunately, as mentioned above, this simulator only considers position and time characteristics of the photon events. In other words, only intensity information is known, and any propagation and phase information about the photons is never created. Thus, while a phase profile could be applied to the data set, it would not have any use as there is no way to propagate events of this form in space or time.

As an alternative, the definition of the distortions as described in Chapter A.2 can be used as a means of simulating this behavior. To reiterate, a lossless distortion is considered as the remapping of one event in an input position space $\mathbf{X}_{\text{in}}$ to any number of events in an output position space $\mathbf{X}_{\text{out}}$. These position spaces are related as $\mathbf{X}_{\text{in}} \cong \mathbf{X}_{\text{out}}$, or in other words, are considered to be isomorphic to one another (i.e. the same size and shape). As such, there exists some mapping $\mathbf{S} : \mathbf{X}_{\text{in}} \rightarrow \mathbf{X}_{\text{out}}$. By defining this mapping for all possible input-output space pairings, the distortions could be conveniently simulated.

Two approaches have been attempted to define this mapping $\mathbf{S}$: the first is by convolving a randomly generated sparse kernel with all events in the input space, and the second is by defining a probabilistic offset to each location in the input space. The first approach is computationally straightforward and can create a somewhat accurate effect to what is observed in the real distortions from turbulent media. Unfortunately, the effect seems to be too weak, and often is notably less complex than real effects. The second approach creates an offset mask by randomly weighting the coefficients of the first 15 Zernike polynomials (Figure A.1). These masks then probabilistically weight an offset function which pushes events up to the corresponding offset mask value at maximum, and does not move the events at minimum. This approach should allow for creating distortions at a similar level of complexity as is seen in real distortions, however it is not yet properly implemented.